Projectile Nose Heating in the Ram Accelerator

by

Gilbert Chew

A dissertation submitted in partial fulfillment
of the requirements for the degree of

Doctor of Philosophy

University of Washington

1995

Approved by _____
Chairperson of Supervisory Committee

Program Authorized
to Offer Degree Aeronautics and Astronautics

Date _____

Projectile Nose Heating in the Ram Accelerator

by

Gilbert Chew

A dissertation submitted in partial fulfillment
of the requirements for the degree of

Doctor of Philosophy

University of Washington

1995

Approved by _____
Chairperson of Supervisory Committee

Program Authorized
to Offer Degree Aeronautics and Astronautics

Date _____

In presenting this dissertation in partial fulfillment of the requirements for the Doctoral degree at the University of Washington, I agree that the Library shall make its copies freely available for inspection. I further agree that extensive copying of this dissertation is allowable only for scholarly purposes, consistent with "fair use" as prescribed in the U.S. Copyright Law. Requests for copying or reproduction of this dissertation may be referred to University Microfilms, 1490 Eisenhower Place, P.O. Box 975, Ann Arbor, MI 48106, to whom the author has granted "the right to reproduce and sell (a) copies of the manuscript in microform and/or (b) printed copies of the manuscript made from microform."

Signature _____

Date _____

University of Washington

Abstract

Projectile Nose Heating in the Ram Accelerator

by Gilbert Chew

Chairperson of the Supervisory Committee: Professor Adam P. Bruckner
Dept. of Aeronautics and Astronautics

A study of in-tube aerodynamic heating of ram accelerator projectiles is presented. The ram accelerator is a ramjet-in-tube device which propels projectiles supersonically through a combustible gas mixture. Many aspects of ram accelerator operation have been studied extensively in the past few years; however, to date most research has not focused on the effects of projectile heat transfer. The current study involves computer simulations of ram accelerator operation, emphasizing the study of aerodynamic heating. The computer simulation couples a TVD finite-difference CFD solution of a viscous turbulent flow field with a semi-implicit solution for the temperature of the solid projectile material. Typical material properties and velocity histories from laboratory experiments were used in the simulations. The results of these computer simulations show that significant increases in temperature are predicted on the nose tip and near the base of the nose cones, where shock impingement occurs. A stress analysis shows that aluminum nose cones are predicted to blunt significantly. Additional simulations show that other aluminum nose configurations, including hemispherical tips and larger nose cone angles are predicted to experience significant tip erosion. In contrast, nose cones made of more refractory alloys, including titanium, titanium-coated aluminum, and steel are predicted to retain structural integrity, and thus attain higher maximum speeds.

Table of Contents

List of Figures

List of Tables

Page

Nomenclature

A	flux Jacobian matrix ($A = \frac{\partial F}{\partial Q}$), parameter in White-Christophe turbulent boundary layer model
A_1, A_2, A_3	intermediate factors in calculation of dissipation vector
A_i	enthalpy model gas constants
A_{ij}	Wilkes Mixing Rule factor for conductivity
a	speed of sound, parameter in White-Christophe boundary layer model
$\underline{a}^i$	contravariant base vectors
B	flux Jacobian matrix ($B = \frac{\partial G}{\partial Q}$), parameter in White-Christophe boundary layer model
B_{ij}	Wilkes' Mixing Rule factor for viscosity
b	parameter in White-Christophe boundary layer model
C	specific heat, flux Jacobian matrix ($C = \frac{\partial H}{\partial Q}$)
C_f	coefficient of skin friction
C_{he}	Stanton number
C_v	constant-volume specific heat
C_s	specific heat of solid alloy
CFD	Computational Fluid Dynamics
CJ	Chapman-Jouguet
c_1, c_2, c_3	collected factors for heat equation

c_i	mass fraction of chemical species i in gas mixture
E	total energy per unit volume, energy
E^*, E^{**}, E^{***}	dummy matrices in CFD algorithm
e	internal energy per unit mass
$\hat{e}_i$	base vectors in physical space
F	ξ-direction flux matrix for Navier-Stokes equations in computational space
$\tilde{F}$	x-direction flux matrix for Navier-Stokes equations in physical space
G	η-direction flux matrix for Navier-Stokes equations in computational space
$\tilde{G}$	y-direction flux matrix for Navier-Stokes equations in physical space
g, g^{ij}	geometric terms for coordinate transformation
g^l_j	flux limiter function
H	matrix for axisymmetric terms in Navier-Stokes equations in computational space
H_0	total enthalpy per unit mass
$\tilde{H}$	matrix for axisymmetric terms in Navier-Stokes equations in physical space
h	enthalpy
h^ξ, h^η	$\frac{\Delta t}{\Delta \xi}, \frac{\Delta t}{\Delta \eta}$
I	identity matrix
i	dummy index for chemical species

J	Jacobian matrix
j	space index ($x=j\Delta x$)
K_1, K_2, K_3	intermediate values in calculation of numerical dissipation vector
k	thermal conductivity, space index ($y=k\Delta y$)
k_0, k_1, k_2	grid metric terms ((ξ_t, ξ_x, ξ_y) or (η_t, η_x, η_y))
k_ξ	factor in calculation of dissipation vector ($k_\xi = \sqrt{\xi_x^2 + \xi_y^2}$)
L	linear matrix operator
M	Mach number, dummy or intermediate matrix
M_i	molecular weight of species i
m	viscosity model exponent, mass flux in x-direction (ρu)
N	number of chemical species
n	time index ($t=n\Delta t$), conductivity model exponent, mass flux in y-direction (ρv)
Pr	Prandtl number
p	pressure
Q	matrix of conserved quantities in computational space
$\tilde{Q}$	matrix of conserved quantities in physical space
q	heat flux
R	gas constant, matrix of eigenvectors of flux Jacobians, radius of curvature of nose tip
R_U	universal gas constant
Re	Reynolds number
r	radial coordinate

S	matrix of source terms in Navier-Stokes equations in computational space, parameter in White-Christophe boundary layer model, sign function
$\tilde{S}$	matrix of source terms in Navier-Stokes equations in physical space
s	distance along wall
T	temperature
t	time
U	contravariant velocity
U_k, U_t	intermediate terms in calculation of dissipation vector
u	component of velocity in x-direction
V	contravariant velocity
v	component of velocity in y-direction
x	physical space coordinate
y	physical space coordinate
Z	Axisymmetry flag (1=axisymmetric, 0=2-dimensional)
z	Axial coordinate

Greek

α	thermal diffusivity, intermediate vector in calculation of numerical dissipation vector, intermediate term in calculation of flux Jacobian matrices
β	combined viscous dissipation and heat flux, shock angle
γ	ratio of specific heats
δ	boundary layer thickness
ε	arbitrary small number
ζ	computational space coordinate

η computational space coordinate

θ azimuthal coordinate direction, implicitness parameter in finite-difference algorithms, flow turning angle, momentum thickness:

$$\left(\int_0^{\delta} \frac{\rho u}{\rho_e u_e} \left(1 - \frac{u}{u_e}\right) dy \right)$$

λ eigenvalue of flux Jacobian matrix

μ viscosity

$\nu^l_{j,k}$ intermediate term in calculation of numerical dissipation vector

ξ computational space coordinate

ρ density

σ principal stress

τ time in computational space

τ_{ij} stress tensor

Φ dissipation vector

ϕ component of dissipation vector Φ

ψ eigenvalue smoothing function

Ω matrix operator in CFD algorithm

ω order of accuracy parameter in CFD algorithm

Subscripts

0 quantity at reference conditions

1, 2 upstream, downstream of shock

∞ freestream conditions

aw	conditions at an adiabatic wall
e	conditions at edge of boundary layer
i	chemical species index
j,k	dummy row and column indices
L	laminar
N	total number of chemical species in gas mixture
n	normal direction
S	solid
T	turbulent
t	tangential direction
t	partial differential with respect to physical time
V	viscous term
w	conditions at the wall
x, y	partial differentials with respect to physical space
ξ, η	partial differentials with respect to computational space
τ	partial differential with respect to computational time

Acknowledgements

The author would like to thank Professor Adam P. Bruckner for his assistance in the preparation of this dissertation. Thanks must also be given to the other professors who have served on the Supervisory Committee: Abraham Hertzberg, David Pratt, Ian Fyfe, James Riley, and Scott Eberhardt. In addition, the support of Prof. Bruckner, Prof. Hertzberg, and Dr. Carl Knowlen over the many years of working on the ram accelerator is greatly appreciated. Thanks also to the many graduate students who have worked on the ram accelerator over the years, particularly Edward Burnham and Alan Kull, who helped prepare the author for the PhD Qualifying Exam, and to the current students on the project: Andrew Higgins, Thomas Imrich, and Josh Elvander. Special thanks to Barbrina Dunmire for reading and editing a very rough draft of this manuscript. Thanks also to Professor Keith Holsapple for the use of Fred, to Mike Nusca of ARL for access to a Cray, and to Melanie Gill of Frame Technology Corporation for a copy of Framemaker. Finally, special thanks to my family for their support over my lifetime.

Dedication

To my parents, Sen Poy and Wai Fong Chew

1. Introduction

For nearly a decade, research has been conducted at the University of Washington on the ram accelerator,[1-3] a device that propels projectiles to high velocities. In a ram accelerator, a projectile travels supersonically through a combustible mixture of gases within a sealed tube. The accompanying shock system compresses the gas flow, which combusts in a zone that travels with the projectile. The resulting pressure distribution generates thrust that accelerates the projectile. In spite of the extensive research performed on the ram accelerator, its maximum demonstrated velocity has been limited by a lack of detailed understanding of the involved processes. In particular, the effects of supersonic aerodynamic heating on ram accelerator projectiles are potentially significant, but have not yet been studied with any detail. However, recent experimental and numerical research sheds new light on this topic. To aid in this endeavor, a new numerical code has been developed, which couples the flow of gases around the projectile to the conduction of heat within the nose alloy. This dissertation presents experimental data, numerical code development, and computer simulations of the effects of aerodynamic heating on ram accelerator projectiles.

1.1 Summary of Ram Accelerator Operation

In principle, a ram accelerator operates much like a conventional airbreathing ramjet (see Fig. 1). The projectile, tube wall, and bluff base function analogously to the centerbody, outer cowling, and flame holders of a supersonic ramjet. In a ram accelerator, a stationary tube is filled with a combustible mixture of gaseous oxidizer and fuel. The projectile, moving supersonically through this gas mixture, generates a complex system of shock waves, which reflect back and forth between the projectile surface and the tube wall. The gas combusts either in a recirculation region at the base

of the projectile or behind a sufficiently strong shock in the flow. The complex interaction of the supersonic flow with the tube wall, projectile, and combustion forms a pressure distribution which produces net positive thrust on the projectile.

Extended study of laboratory experiments has allowed the identification of three regimes of operation, which are defined by the ratio of the projectile velocity to the Chapman-Jouguet (CJ) detonation velocity. Briefly, a CJ detonation wave is a

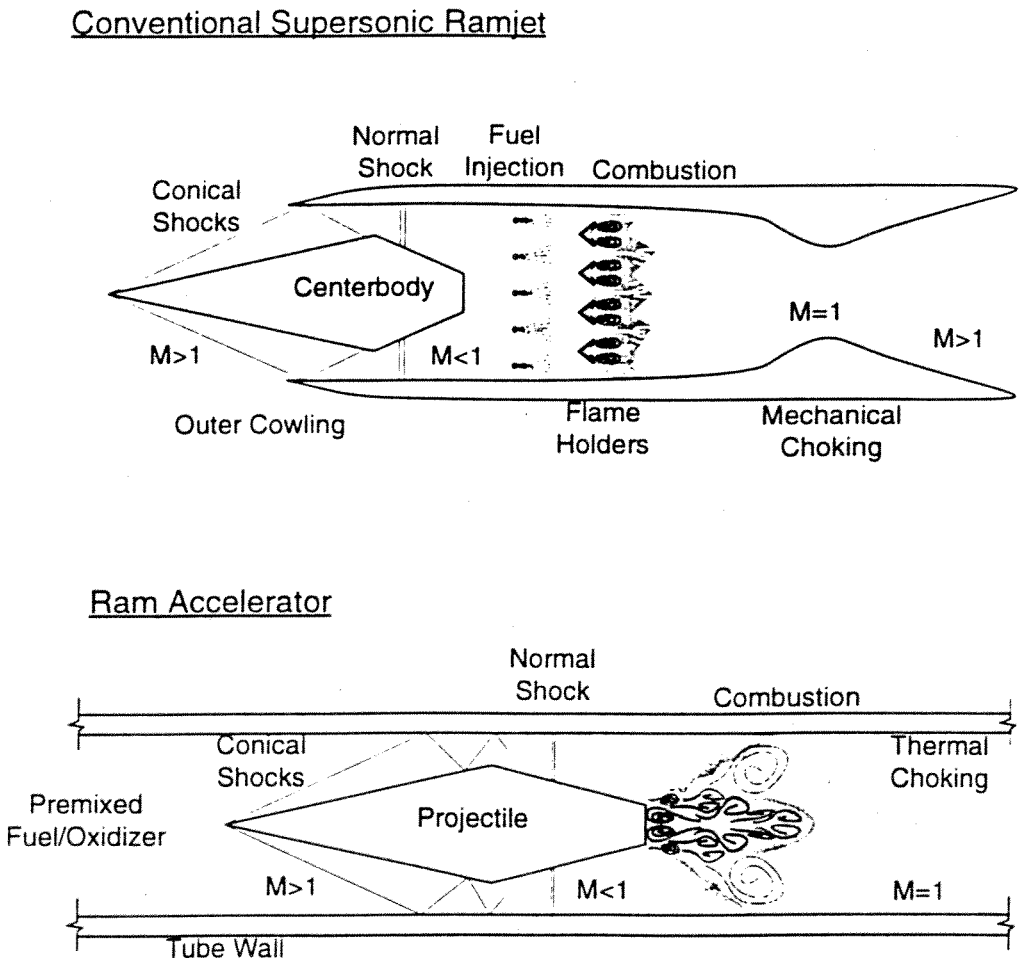

Figure 1. Comparison of conventional ramjet and ram accelerator.

supersonically traveling shock wave followed by a zone of combustion which thermally chokes the shocked gas, driving it to a Mach number of unity relative to the wave front.[4] Any given mixture of combustible gases has characteristic thermodynamic properties, including sound speed and heat of combustion; these properties govern the unique speed at which a self-sustaining detonation will travel, known as the CJ detonation velocity. In the ram accelerator, the subdetonative and superdetonative velocity regimes are identified by projectile velocities below and above the CJ speed of the resident gas mixture, respectively. The transdetonative regime corresponds approximately to a velocity range between 90% and 110% of the CJ speed. The impetus for the division of ram accelerator operation into these three regimes is the widely differing operating and performance characteristics in each regime.[5]

Most of the research to date has been performed at subdetonative velocities. Current theory holds that in this velocity range the ram accelerator operates in a thermally choked mode. Combustion in a recirculation region at the base of the projectile is thought to thermally choke the flow, which in turn supports a normal shock system on the projectile body. The shock system induces a high-pressure zone at the rear of the projectile body, producing thrust. A simplified quasi-one-dimensional theory holds that as the projectile accelerates and its Mach number increases, the normal shock recedes back along the body, reducing thrust. For a fully tapered tail, this normal shock would continue to recede back as the projectile accelerates, only falling off (at full tube area) when the projectile velocity had attained the CJ speed of the gas mixture. At this point, the thrust on the projectile is zero. Thus, the maximum theoretically attainable velocity of a thermally choked ram accelerator equals the CJ speed of the propellant gas.

At velocities much higher than the CJ speed, the conical shock system on the projectile becomes much stronger; one of these shocks may become strong enough to induce combustion in front of the recirculation zone. Thus, shock-induced combustion, or perhaps even an oblique detonation, may result. In this mode, the flow is not thermally choked behind the projectile, and no normal shock forms on the body. However, the resulting pressure distribution still produces a net positive thrust, accelerating the projectile. Presently, there has been only limited experimentation in the superdetonative regime,[6] so these conjectures have not been conclusively verified.

Between the superdetonative and subdetonative regimes lies the transdetonative velocity range.[7] In many experiments, projectiles have been observed to experience markedly increased acceleration as they reach the upper range of subdetonative operation. Often, projectiles attain speeds well beyond the CJ detonation velocity, in defiance of quasi-one-dimensional thermally choked theory. Since this phenomenon is highly repeatable, the definition of a separately defined regime is justified. However, as yet a theoretical basis for operation in this mode is not well understood.

1.2 Applications

The unique characteristics of ram accelerator technology can be incorporated into many interesting applications. High velocities may be achieved through relatively uniform continuous acceleration, allowing projectiles to avoid the extremely harsh accelerations found in conventional guns. Unlike rockets, thrust is obtained without the need for onboard propellant. Ram accelerators are powered by common gaseous fuels, whose pressure can be readily varied to tailor the projectile velocity. In short, ram accelerators avoid some of the persistent and troublesome limitations of other high-

speed mass-launch devices. Proposed applications of ram accelerators include Earth-to-orbit mass launchers for acceleration-insensitive payloads,[8,9] and as launchers in ground-based aeroballistic test facilities.[10,11,12]

The ram accelerator is also one of the few devices that combine supersonic operation with combustion. In this respect, the ram accelerator incorporates processes similar to the next generation of aerospace engines. Study of ram accelerator operation may thus lead directly to better understanding of the phenomena involved in these advanced engines. Also, the complex combusting flowfield within the ram accelerator can provide test data against which computational simulation programs may be checked; these computer programs, so important to the design of new engines, often lack "real world" validation. Thus, the ram accelerator can be viewed as a test bed or experimental platform, on which basic science, directly applicable to advanced aerospace engines, can be performed.

These potential applications have sparked worldwide interest in ram accelerator technology. Experimental facilities can be found at the U.S. Army Research Laboratory in Maryland[13], Institute de Saint-Louis in France,[14] and at Hiroshima University[15] and Tohoku University[16] in Japan.

1.3 Thrust of Research

Although ram accelerator research has sparked much interest, many of the processes involved are not well understood, such as the effects of localized aerodynamic heating of the projectile and associated blunting of the nose. This problem may limit the velocity capability of ram accelerators, as the aerodynamic heating at high Mach numbers weakens, and even melts, the surface of the projectile.

An approximate relation between heat flux and nose tip radius can be found by examining the heat flux of spheres. The stagnation point heat flux of spheres can be estimated from the following correlation:[17]

$$q_w = 0.763\ \mathrm{Pr}^{-0.6} \sqrt{\rho_e \mu_e} \sqrt{\frac{du_e}{dx}} (h_{aw} - h_w) \tag{1.1}$$

where ρ is the density, μ is the viscosity, u is the velocity, h is the enthalpy of the gas, and x is the streamwise distance; the subscript e refers to conditions at the edge of the boundary layer, and the subscripts w and aw refer to conditions at the wall and at a hypothetical adiabatic wall, respectively. The velocity gradient can be found[17] from

$$\frac{du_e}{dx} = \frac{1}{R} \sqrt{\frac{2\,(p_e - p_\infty)}{\rho_e}} \tag{1.2}$$

where p is the pressure and R is the radius of curvature of the sphere; the subscript ∞ refers to freestream conditions. Combining the two expressions yields

$$q_w = 0.763\ \mathrm{Pr}^{-0.6} \sqrt{\frac{\rho_e \mu_e}{R}} \left(\frac{2\,(p_e - p_\infty)}{\rho_e} \right)^{\frac{1}{4}} (h_{aw} - h_w) \tag{1.3}$$

Examination of the above equation shows that the stagnation point heat flux is inversely proportional to the square root of the radius of curvature. Thus, a sharp nose with an attached conical shock can melt quickly into a blunt nose with a detached bow shock. This blunting may have deleterious effects on the flow, stemming from the presence of the entropy layer,[18] the streamtubes of gas next to the projectile that must pass through the strong (normal to near-normal) shock around the centerline. The hot entropy layer may induce combustion in the flow earlier than in flow over sharp cones. Early ignition is a subject of current study; the effects may include movement of the combustion zone

through the subsonic boundary layer from behind the projectile up onto the projectile itself, and possibly to the nose. While combustion on the body has been speculated as producing thrust at velocities greater than the CJ detonation speed of the gas mixture,[19] combustion on the nose may lead to choking of the flow at the throat and an undesired unstart. (In ram accelerator experiments testing the limits of operation, the experiment often ends with the cessation of projectile acceleration within the tube, and the formation of a normal shock ahead of the projectile. The situation is analogous to ramjet engine unstarts, and hence the term is also used in conjunction with ram accelerators. Unstarts are suspected to be associated with projectile structural failures or unsteady aerothermodynamic phenomena; their causes are not yet completely understood.) Consequently, aerodynamic heating can have a twofold effect: it can weaken the nose cone and it can change the aerodynamics of the flow, possibly adversely affecting overall ram accelerator performance. In order to design for these detrimental effects and minimize them, aerodynamic heating of ram accelerator projectiles needs to be better quantified.

To date, relatively little investigation of in-tube aerodynamic heating has been done. Preliminary unpublished calculations, modeling the projectile surface as a flat slab, indicated that the recovery temperature often exceeds the melting temperature of the projectile material. More extensive computations modeled the flow using modified integral boundary layer theory and a one-dimensional heat transfer model, and, simulating laboratory experiments, concluded that the projectile surface begins to melt at the time of projectile unstart.[20] Finally, a preliminary investigation of this problem by the author, using a Computational Fluid Dynamics (CFD) axisymmetric laminar flow solver, simulated a laboratory experiment, again concluding that the surface temperature at the nose tip typically reaches the alloy melting point.[21] Another conclusion was that

choice of projectile material greatly influenced the extent and magnitude of the rise in temperature.

This dissertation presents a more extensive analysis of ram accelerator projectile heating. A series of laboratory experiments compare projectiles with identical external projectile configurations, but made of different alloys. Any differences in velocity history would be expected to result mainly from the differences in the thermal and mechanical properties of the alloys. To complement this experimental effort, a more general computer program has been written that simulates laboratory experiments. In this program, a CFD algorithm solves the Navier-Stokes equations, using the Baldwin-Lomax turbulence model. Heat conduction within the projectile is solved using a standard Alternating Direction Implicit (ADI) method on the unsteady heat equation. Either two-dimensional or axisymmetric solutions can be computed. The program thus couples solutions of the gas flow around the projectile to solutions of the heat flow within the projectile. Using this program, the extent of heat transfer to ram accelerator projectiles in simulated experiments is investigated. Combined, the laboratory experiments and computer simulations indicate the alloy properties necessary to optimize the maximum projectile velocity.

A description of the research facilities, both experimental and computational, are presented first, followed by the experimental data. Next to be shown are the governing equations of the fluid flow and heat transfer, followed by a summary of the numerical methods used to solve these equations. Finally, the data generated by the resulting numerical code are presented.

2. Research Facilities

2.1 Experimental Apparatus

The ram accelerator facility at the University of Washington consists of three main sections: the initial launcher, the main ram accelerator test section, and the final decelerator section (see Fig. 2). The initial launcher consists of a single-stage light gas gun and vent section, and serves to accelerate an initially stationary projectile to the desired entrance velocity of the ram accelerator section. The gas gun typically uses helium as the driver gas, which eventually vents into a dump tank through small holes in the wall of a vent tube. At the end of the initial accelerator, projectiles attain velocities of up to 1500 m/s.

Experimentation takes place in the test section, which is itself composed of eight steel tubes, each 2 m long. The tubes are joined by steel collars, which thread onto the ends. The purpose of this design is to allow the test section to be subdivided into stages, with each stage containing different gas mixtures and/or pressures. The stages are separated by thin Mylar diaphragms, placed at the joints between tube sections. Each stage can thus have a chosen gas mixture, each tailored for ram accelerator operation in different velocity ranges. As the projectile accelerates down the tube, it travels through gas mixtures with successively higher sound speeds and varying chemical energy densities. This design allows the projectile Mach number and operating heat release to be kept within the optimal ranges over the entire length of tube.

All instrumentation in the ram accelerator consists of probes placed in the wall of the test section. Forty instrument stations are spaced at 40 cm intervals along the length of the tube, and each station has multiple instrument ports, placed azimuthally around the circumference of the tube; four-port stations alternate with three-port stations. With

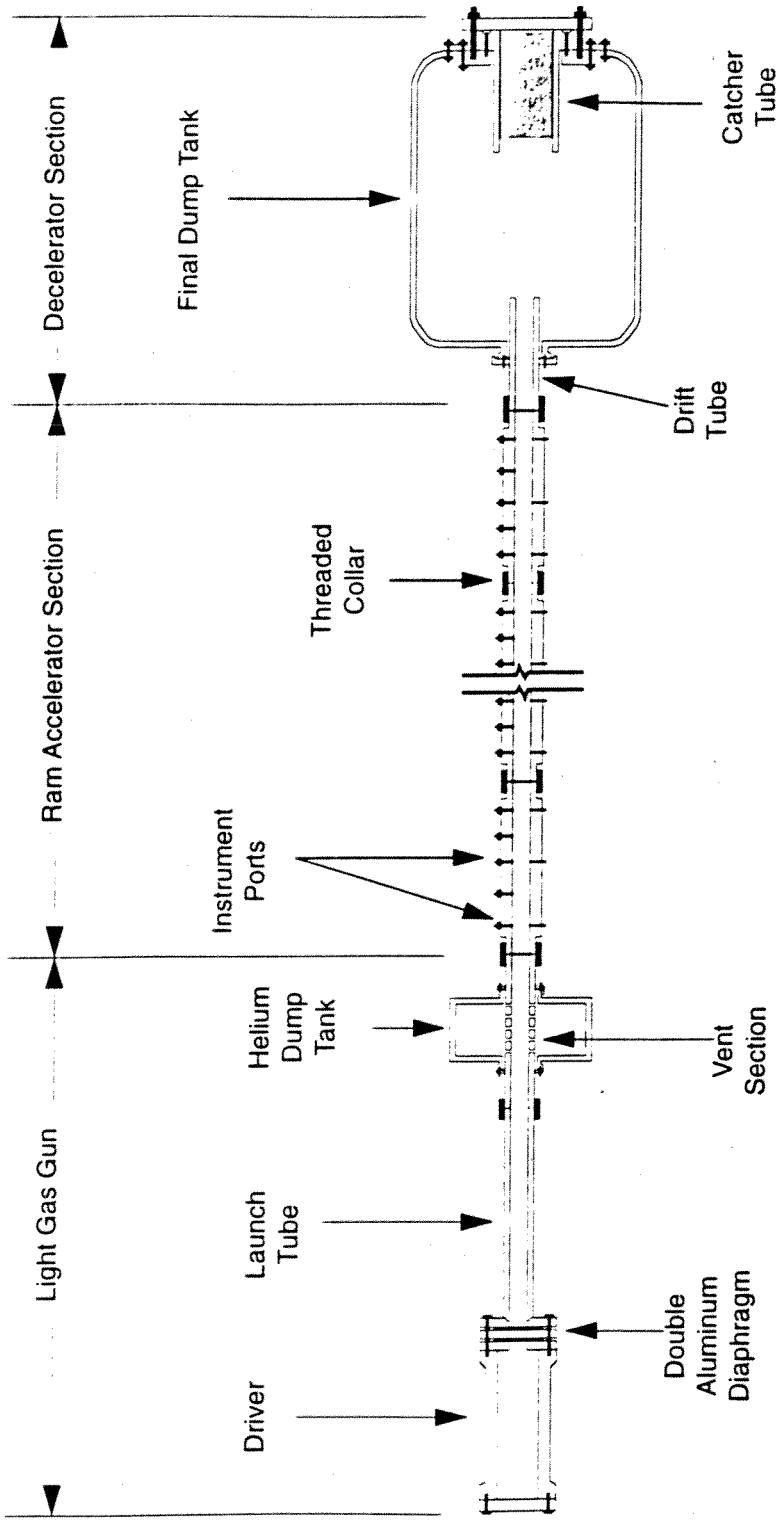

Figure 2. Schematic of ram accelerator experimental facility.

such multiple ports, various combinations of instruments can be used to obtain data at any station. The current array of instruments includes electromagnetic sensors, piezoelectric pressure transducers, fiber-optic light guides, and (occasionally) thermocouples. Data from a multiply-instrumented station provide a good snapshot of the processes occurring in the tube at a given location as the projectile speeds by the station. However, the data are limited by the placement of the instrument ports: currently, experimental data are measured solely at the surface of the bore. Although much can be inferred from these data, conditions at the actual surface of the projectile are not directly measured, and are largely unknown. The small size of the projectiles has so far prohibited use of on-board instrumentation.

Upon exit from the test section, the projectile passes through a short drift tube, and enters the decelerator section. Here, the projectile travels across an evacuated dump tank; a window in the side of the dump tank allows the projectile to be photographed. A short catcher tube, filled with tightly wound carpet remnants, finally stops the projectile.

A more detailed description of the facility can be found in Ref. 23.

2.2 Experimental Projectiles

The nominal external projectile configuration is shown in Fig. 3. Ram accelerator projectiles consist of two major components: the nose and the body. Externally, the nose is a smooth, sharp-pointed cone. The body is a truncated cone, with fins distributed around its circumference: the fins span the bore of the tube, and serve to center the projectile as it slides down the tube. The number of fins is variable: most projectiles used to date have either four or five fins. The flat rear face of the body is

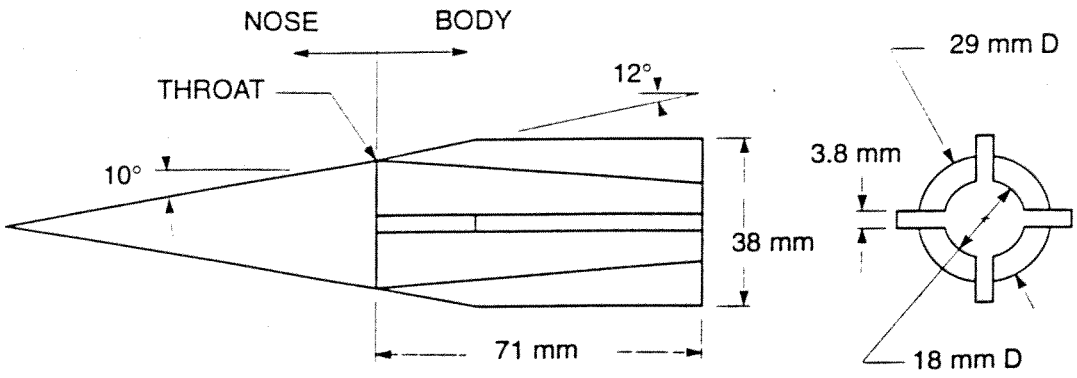

Figure 3. Projectile configuration.

thought to act as a bluff-body flameholder, aiding in the stabilization of combustion at the rear of the projectile.[2]

Generally, the nose and the body are manufactured as two separate pieces which thread together at the throat, where the cross-sectional area of the projectile is greatest (and hence where the flow area is smallest). This technique allows the pieces to be hollowed out, reducing the overall mass. Minimizing the mass maximizes the acceleration for a given thrust; however, less material is then available to bear mechanical and thermal loads. Also, although the projectile is often made of a single material (either aluminum or magnesium alloys), the two-piece design allows different materials to be used in the construction of the nose and the body. For example, some projectiles have been fabricated with an aluminum nose and magnesium body, and vice versa. Other possible structural variations involve constructing the fins and/or the tip of the nose cone as separate pieces. Thus, as many as four different materials could be used in projectile manufacture, each optimized for the different structural components.

2.3 Computational Facility

Most of the computer simulations were performed either on a DEC 3000 Model 300 AXP workstation running XWindows and UNIX, located at the University of Washington, or on a Cray C90 supercomputer, located at the United States Army Engineer Waterways Experiment Station in Vicksburg, Mississippi. Miscellaneous code development also took place on an IBM-compatible personal computer with an 80386 CPU running at 40 MHz. All codes were written in FORTRAN-77. Other software, including the finite-element program (to be described later) used for this dissertation, was run on a University of Washington Uniform Access VAX computer.

2.3 Computational Facility

Most of the computer simulations were performed either on a DEC 3000 Model 300 AXP workstation running XWindows and UNIX, located at the University of Washington, or on a Cray C90 supercomputer, located at the United States Army Engineer Waterways Experiment Station in Vicksburg, Mississippi. Miscellaneous code development also took place on an IBM-compatible personal computer with an 80386 CPU running at 40 MHz. All codes were written in FORTRAN-77. Other software, including the finite-element program (to be described later) used for this dissertation, was run on a University of Washington Uniform Access VAX computer.

3. Laboratory Research and Discussion

3.1 Introduction

Improvements in the current understanding of the ram accelerator require both numerical and experimental studies. Currently, numerical simulations are not sufficiently complex to fully model all aspects of ram accelerator operation, and do not predict all significant phenomena. Conversely, experimental data are limited in variety and spatial density, and are difficult to obtain, due to the harsh conditions and short experiment times. Often, interpretation of data is difficult and inconclusive. Obviously, a combination of computational simulations and laboratory experiments is necessary for a complete picture. The lab experiments provide the basic data of real phenomena, and the simulations provide detail and insight.

To date, most of the experiments have focused on studying the effects of varying the relative amounts of component gases in the tube, the gas fill pressure, or the staging of various gas mixtures — in short, the effects of aerodynamic nose heating have, for the most part, not been studied. Currently, the ram accelerator facility at the University of Washington is not equipped to measure the temperature anywhere in the projectiles during an experiment. No on-board instrumentation is carried by the projectiles because of their small size, and the transducers in the ram accelerator tube measure only the pressure and luminosity of the gas at the inner tube surface, away from the projectile itself. The only other data that are available are the velocity histories of the projectiles. Assuming that excessive heating of the projectile alloy interferes with nominal ram accelerator operation, then the maximum velocity attained by a projectile reflects the heat flux history in a given experimental configuration.

3.2 Projectile material variations

In designing projectiles to withstand the high-temperature ram accelerator environment, there are three basic types of materials to consider: refractory substances, such as titanium; good conductors, such as copper; and ablators, such as carbon composites. Refractory substances generally have high melting temperatures, and retain high strength even close to the melting point. Good conductors carry heat quickly away from a hot surface; thus a large influx of heat is spread out over a large amount of material, reducing the maximum rise in temperature. Ablators convert sensible heat into the heat of vaporization; the solid that is left is thus protected from the full effect of the heat flux. Most materials used in the construction of ram accelerator projectiles combine, to some extent, characteristics of all of these three types. However, the characteristics of candidate materials still vary widely, and some materials are expected to better endure the harsh conditions of ram accelerator operation than others.

In expectation of the effects of variations in projectile material on overall maximum velocity, projectiles made of different materials have been used in ram accelerator experiments in an effort to ascertain the optimum configuration. Some of the material properties of three of the alloys used in the experiments to date are listed in Table 1.[22] Obviously, the thermophysical properties of the titanium alloy differ greatly from those of the magnesium and aluminum alloys, which are relatively similar to each other. Thus, the limits of operation of a projectile constructed from titanium are expected to differ significantly from those of either magnesium or aluminum projectiles.

Indeed, this conclusion is supported by a series of one-stage experiments using projectiles made of different alloys. The only major variations were in the alloy and internal configuration; assuming that the chemistry and gross flow characteristics are

Table 1. Properties of projectile alloys

Property	Aluminum 7075-T6	Magnesium ZK60A	Titanium 6Al-4V
Melting Temperature (K)	750-910	795-910	1810-1920
Density (kg/m^3)	2800	1830	4470
Thermal Conductivity (W/m-K)	121-182 (280-590K)	121-132 (310-560K)	7-18 (310-1140K)
Specific Heat (J/kg-K)	835-1045 (300-590K)	1045-1340 (370-750K)	565-837 (310-1030K)
Yield Tensile Strength (10^8 Pa)	4.8 (310 K) 0.5 (590 K)	3.6 (293K) 1.0 (500K)	10.2 (310 K) 1.8 (1140K)

largely independent of these variables, only structural strength and thermal properties are affected, thus directly testing the effects of aerodynamic heating. A schematic of the standard external configuration of projectile noses, including the major dimensions, is shown in Fig. 4. The internal configurations of aluminum and titanium noses are shown in Figs. 5 and 6, respectively. Note that the dimensions shown cause the walls of the

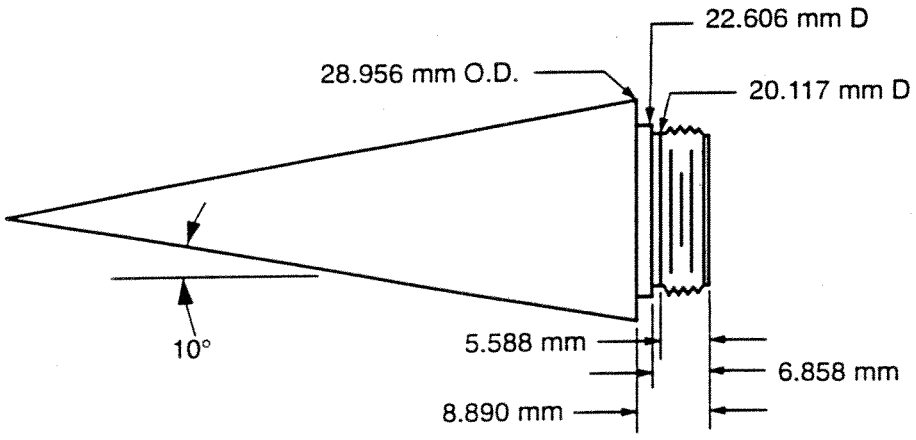

Figure 4. External configuration of standard projectile nose.

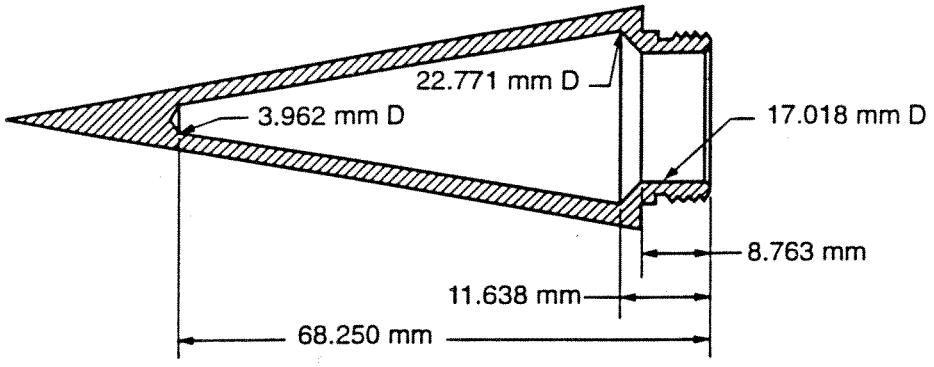

Figure 5. Internal dimensions of aluminum noses.

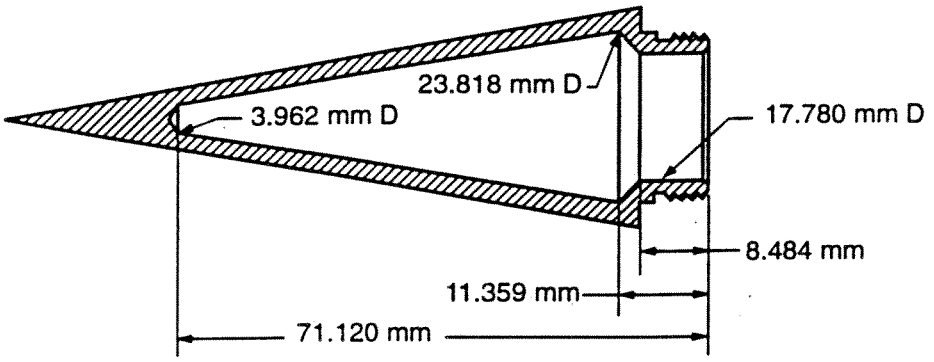

Figure 6. Internal dimensions of titanium noses.

titanium nose to be thinner than those of the aluminum nose; this feature was designed to take advantage of the much higher yield strength of the titanium alloy. Since titanium is much denser than aluminum, using the same dimensions for each alloy would result in large differences in total mass between the two types of projectiles and hence much lower accelerations for titanium projectiles. To compensate for the difference in densities, projectiles made of titanium are constructed with thinner walls. This adjustment minimizes the variation in overall projectile mass, and thus reduces the effect

of velocity history on maximum velocity. Table 2 summarizes the configurations for the

Table 2. The alloy variation series.

EXPERIMENT NO.	HS 1062	HS 1063	HS 1064	HS 1065	HS 1066
Body alloy	Al	Al	Ti	Mg	Ti
Nose alloy	Al	Ti	Al	Mg	Ti
Total Mass (g)	76.85	86.63	100.95	107.16	108.70
Tube Fill Pressure (Pa)	$5.0(10^6)$	$5.1(10^6)$	$5.1(10^6)$	$5.2(10^6)$	$5.1(10^6)$
Max. Velocity (m/s)	2070	2100	1850	1510	2046
Unstart?	Yes	Yes	Yes	Yes	No

alloy variation series of experiments. The gas mixture used in each of this series of experiments consisted of 2.8 CH_4 + 2 O_2 + 5.7 CH_4. Figure 7 shows the velocity-time histories of this series. The velocities were calculated by centrally-differencing the projectile position and time data. Minor differences in accelerations arise from the somewhat different combinations of projectile mass and initial gas pressure in each experiment; the chemical composition and projectile shape were held constant. Obviously, the all-aluminum projectile used in HS 1062 performed very well, achieving high accelerations up to a high maximum velocity of 2070 m/s. The projectile unstarted immediately upon reaching this speed. In HS 1063, the projectile with an aluminum body and a titanium nose attained a marginally higher maximum velocity; however, in this experiment, the projectile coasted (i.e., neither accelerated nor decelerated) approximately 1 m at the maximum velocity before unstarting, unlike the prior experiment. In the third experiment, HS 1064, the projectile with a titanium body and an aluminum nose unstarted at a significantly lower velocity of 1850 m/s. The fourth experiment, HS 1065, was an attempt to obtain magnesium projectile data for

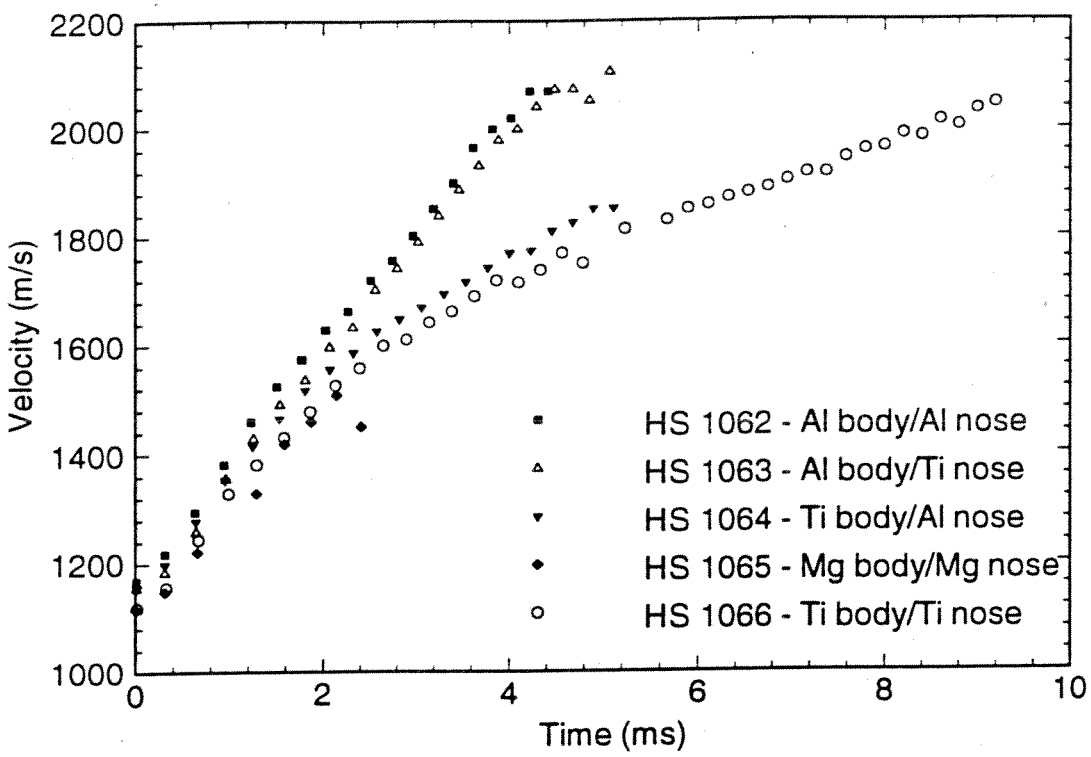

Figure 7. Velocity histories of projectile alloy variation experiment series in single-stage ram accelerator.

comparison over a wider range of alloys; an insert made of lead was placed inside a magnesium projectile, so that the projectile mass, initial gas fill pressure and resulting velocity history would be virtually identical to that of an all-titanium projectile. Unfortunately, this projectile suffered an anomalously early unstart. Finally, in HS 1066, an all-titanium projectile was used. Due to its high mass, and the safety limits on the initial gas fill pressure, the acceleration of the projectile in HS 1066 is lower than that of the aluminum-body projectiles in HS 1062 or HS 1063, although it is similar to that of HS 1064. Obviously, the maximum velocity of the all-titanium projectile is much higher than that of HS 1064, and is roughly equal to the velocities attained in HS 1062

and HS 1063. More importantly, the projectile was observed to be still accelerating at the end of the ram accelerator section; unlike the prior experiments, the projectile did not unstart in the tube.

The projectiles in which a titanium nose was used all attained a similarly high maximum velocity; the projectiles which did not have titanium noses generally did not last as long, and unstarted at lower velocities. This result is consistent with the expectation that titanium would endure the harsh conditions (high temperatures and pressures) in the ram accelerator better than magnesium or aluminum, since titanium has the highest yield strength and melting temperature of the three alloys, as shown in Table 1.

Although the all-aluminum projectile reached a maximum velocity comparable to that of the titanium-nose projectiles, this result is not inconsistent with the theory that transient projectile heating affects the maximum velocity of the projectile. The high acceleration of the low-mass projectile results in a reduced time for heat to be absorbed by the projectile before reaching high speeds. Thus, the aluminum projectile may simply have accelerated to a high speed before its alloy could weaken or melt.

These results also show that the alloy used in constructing the projectiles is possibly more critical for the nose than for the body. The velocity profile of HS 1064 is very similar to that of HS 1066 for the first five ms of each experiment, yet the projectile in HS 1064 unstarted soon after this point, while the projectile in HS 1066 continued to accelerate to much higher speeds. Both projectiles used a titanium body; the most significant difference between the two experiments is the nose alloy, indicating that some failure of the aluminum nose may have contributed to the earlier unstart in HS 1064. In contrast, the alloy used to fabricate the projectile body seems to have less

effect on the projectile velocity. Consider the experiments HS 1062 and HS 1064: the projectiles of both experiments had aluminum noses, differing only in the body alloy. In spite of the expected greater durability of the titanium body of HS 1064, an unstart occurred at a much lower projectile velocity than in HS 1062, indicating that the superior durability of a titanium body is largely irrelevant to the maximum attainable velocity.

The apparent superiority of titanium noses for attaining high velocities and enduring long experiment times is supported by another pair of experiments, this time in a two-stage ram accelerator. The experimental configuration is summarized in Table 3.

Table 3. Two-stage alloy comparison.

EXPERIMENT	HS 1076	HS 1093
Nose alloy	Al	Ti
Body alloy	Al	Al
Total Mass (g)	76.53	83.62
First stage fill pressure (Pa)	$5.1(10^6)$	$5.0(10^6)$
Second stage fill pressure (Pa)	$5.1(10^6)$	$5.1(10^6)$
Max. Velocity (m/s)	2200	2310
Unstart?	Yes	Yes

In both experiments, the first stage consisted of 2 m of the mixture $2.8\ CH_4 + 2\ O_2 + 5.7\ CH_4$, and the second stage consisted of 14 m of the mixture $6\ CH_4 + 2\ O_2 + 2\ H_2$. As explained in Chapter 2, staging allows the projectile to remain in an optimum range of Mach numbers, maximizing thrust as it accelerates down the ram accelerator tube. A comparison of the projectile velocity histories from the two experiments is shown in Fig. 8. As in the one-stage experiments, the projectile with an

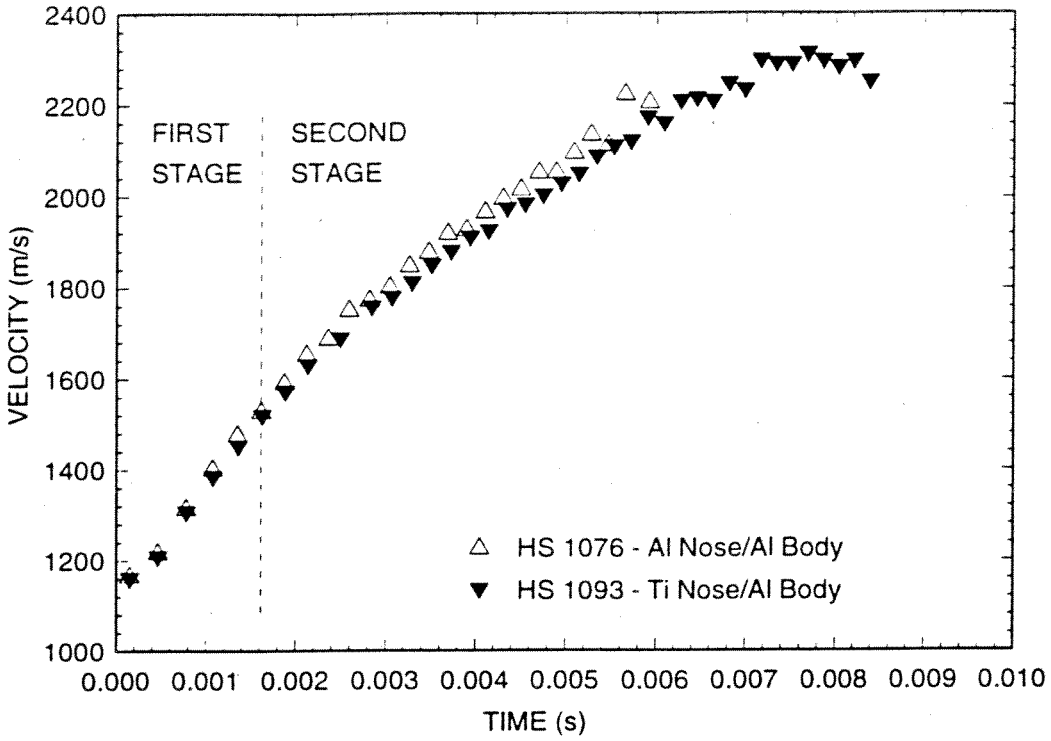

Figure 8. Velocity histories of projectiles in two-stage ram accelerator experiments comparing an aluminum and a titanium nose.

aluminum nose experienced an unstart earlier in the experiment than the projectile with a titanium nose. Although the velocity profiles are very similar in the early part of the experiment, the titanium-nose projectile reached a higher velocity than the aluminum-nose projectile. Again, the alloy used in constructing the nose is the major difference between the two experimental configurations; thus, again, projectiles with titanium noses seem to be superior.

Unfortunately, as yet the ram accelerator facility at the University of Washington is not equipped to directly measure the state of the projectile nose before or during an unstart. Currently, the instrumentation at this facility measures pressure only at the tube wall, relatively far from the surface of the nose. Consequently, the only tool available

for more extensive analysis is numerical simulation. Thus, the next step in analyzing the heating of the nose is to develop a computer program to simulate the experiments.

4. Governing Equations

4.1 Navier-Stokes Equations

A theoretical analysis of the ram accelerator begins with the equations of conservation of mass, momentum, and energy. To reduce the complexity of the calculations, the axisymmetric form of the conservation equations is used. The axisymmetric form is nearly as simple as the two-dimensional form, but since the projectile nose itself is axisymmetric, this form of the equations describes the flow over the nose as accurately as the more complex three-dimensional form.

The axisymmetric Navier-Stokes equations[24] can be written in matrix form as

$$\frac{\partial \tilde{Q}}{\partial t} + \frac{\partial}{\partial x}(\tilde{F} - \tilde{F}_V) + \frac{\partial}{\partial y}(\tilde{G} - \tilde{G}_V) + Z(\tilde{H} - \tilde{H}_V) = \tilde{S} \tag{4.1}$$

where $\tilde{Q}$ is the matrix of conserved quantities:

$$\tilde{Q} = \begin{bmatrix} \rho_1 \\ \rho_2 \\ \cdots \\ \rho_N \\ \rho u \\ \rho v \\ E \end{bmatrix}. \tag{4.2}$$

The flux matrices $\tilde{F}$ and $\tilde{G}$ represent the non-viscous terms in the conservation equations:

$$\tilde{F} = \begin{bmatrix} \rho_1 u \\ \rho_2 u \\ \cdots \\ \rho_N u \\ \rho u^2 + p \\ \rho uv \\ u(E+p) \end{bmatrix} \qquad \tilde{G} = \begin{bmatrix} \rho_1 v \\ \rho_2 v \\ \cdots \\ \rho_N v \\ \rho uv \\ \rho v^2 + p \\ v(E+p) \end{bmatrix} \tag{4.3}$$

and the matrix $\tilde{H}$ represents terms in the conservation equations unique to axisymmetric flow:

$$\tilde{H} = \frac{1}{y} \begin{bmatrix} \rho_1 v \\ \rho_2 v \\ \cdots \\ \rho_N v \\ \rho uv \\ \rho v^2 \\ v(E+p) \end{bmatrix} \tag{4.4}$$

Similarly, the viscous terms of the conservation equations of fluid flow are collected in the flux matrices $\tilde{F}_V$, $\tilde{G}_V$, and the axisymmetric flow matrix $\tilde{H}_V$:

$$\tilde{F}_V = \begin{bmatrix} 0 \\ 0 \\ \cdots \\ 0 \\ \tau_{xx} \\ \tau_{xy} \\ u\tau_{xx} + v\tau_{xy} - q_x \end{bmatrix} \qquad \tilde{G}_V = \begin{bmatrix} 0 \\ 0 \\ \cdots \\ 0 \\ \tau_{xy} \\ \tau_{yy} \\ u\tau_{xy} + v\tau_{yy} - q_y \end{bmatrix} \tag{4.5}$$

$$\tilde{H}_V = \frac{1}{y}\begin{bmatrix} 0 \\ 0 \\ \cdots \\ 0 \\ \tau_{xy} \\ \tau_{yy} \\ u\tau_{xy} + v\tau_{yy} - q_y \end{bmatrix}. \tag{4.6}$$

The matrix $\tilde{S}$ represents source terms otherwise unaccounted for in the conservation equations. For example, a chemical reaction would change the amounts of the involved chemical species.

The first N rows of the matrix equation constitute the equation of mass conservation for each molecular species considered. Similarly, the succeeding rows correspond to the equations of momentum (in the longitudinal and radial directions) and energy conservation, respectively. For axisymmetric flow, $Z = 1$ in Eq. 4.1; otherwise, for two-dimensional ("wedge") flow, $Z = 0$. In the above equations, ρ_i is the density of molecular species i, ρ is the overall density of the gas mixture, N is the total number of different species, u and v are the velocities in the x and y directions, respectively, p is the pressure, and E is the total energy per volume of gas. The terms labelled τ_{ij} are the components of the fluid stress tensor, and are nonzero only for viscous flow. The definitions for the components of the stress tensor τ are shown below:

$$\tau_{xx} = -\frac{2}{3}\mu\left[-2\frac{\partial u}{\partial x} + \frac{\partial v}{\partial y} + \frac{v}{y}\right] \tag{4.7}$$

$$\tau_{yy} = -\frac{2}{3}\mu\left[\frac{\partial u}{\partial x} - 2\frac{\partial v}{\partial y} + \frac{v}{y}\right] \tag{4.8}$$

$$\tau_{\theta\theta} = -\frac{2}{3}\mu\left[\frac{\partial u}{\partial x} + \frac{\partial v}{\partial y} - 2\frac{v}{y}\right] \tag{4.9}$$

$$\tau_{xy} = \mu\left[\frac{\partial u}{\partial y} + \frac{\partial v}{\partial x}\right] \tag{4.10}$$

The q terms result from heat flow in the fluid. According to Anderson,[25] the threshold temperature for substantive radiative heat transfer is roughly 10,000 K. The maximum temperature in the flow can be estimated from the expression for the stagnation temperature of an ideal gas:[26]

$$T_0 = T\left(1 + \frac{\gamma - 1}{2}M^2\right) \tag{4.11}$$

where γ is the ratio of specific heats, M is the Mach number, and T and T_0 are the freestream and stagnation temperatures, respectively. For the ram accelerator, a typical experiment has $\gamma = 1.36$, $T = 293$ K, and a maximum Mach number of about 6, resulting in a stagnation temperature of approximately 2200 K; thus, radiative heat transfer can be ignored. Therefore, only thermal conduction contributes to the heat flux terms, and

$$q_x = -k\frac{\partial T}{\partial x} \qquad q_y = -k\frac{\partial T}{\partial y} \tag{4.12}$$

where T is the temperature and k is the thermal conductivity.

Collectively, these equations are known as the Navier-Stokes equations of fluid flow.

4.2 Coordinate Transformation

When coupled with an equation of state and appropriate boundary conditions, these equations can completely characterize the aerodynamics of the ram accelerator. However, they are not in the most convenient form for solution by finite difference

methods. For finite difference solutions, the physical region of interest is subdivided by a grid of points, with flow variables to be solved at each point. The differentials of the conservation equations are approximated by algebraic combinations of the data at each grid point; thus, solving a finite-difference problem ideally constitutes an exact solution to a close approximation to a real problem. Orthogonal grids are not used here; instead, meshes are generated to conform to the physical boundaries of the problem of interest. Without an orthogonal mesh, however, finite-difference representations of the conservation equations become quite complex and difficult to solve.

The solution to this problem is to transform the mesh into an orthogonal coordinate system, as shown in Fig. 9. This transformation is fairly common, and is derived elsewhere.[27] Simply, the physical (x,y) coordinates are transformed into computational (ξ,η) coordinates, in which the transformed computational mesh is orthogonal.

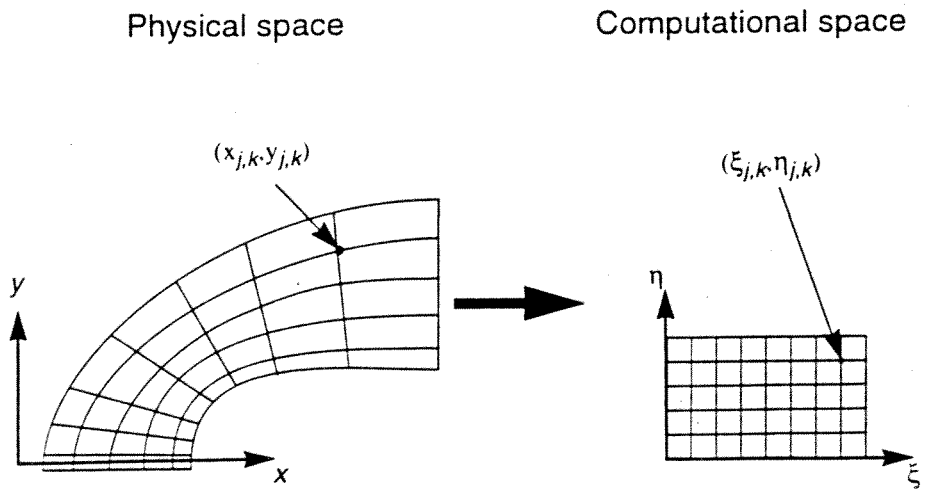

Figure 9. Grid transformation.

4.3 Grid Metrics

Using a coordinate transformation requires the calculation of quantities known as grid metrics, which relate the differences in geometry between computational and physical space. The grid metrics ξ_x, η_x, ξ_y, and η_y are defined as follows:

$$\xi_x \equiv \frac{\partial \xi}{\partial x} \qquad \xi_y \equiv \frac{\partial \xi}{\partial y} \qquad \eta_x \equiv \frac{\partial \eta}{\partial x} \qquad \eta_y \equiv \frac{\partial \eta}{\partial y} \tag{4.13}$$

A convenient quantity to define is the Jacobian of the transformation J. The Jacobian will be used to calculate the grid metrics, and is itself first computed using the known coordinates of the grid points. The inverse of the grid Jacobian is given by

$$J^{-1} = x_\xi y_\eta - x_\eta y_\xi \tag{4.14}$$

where

$$x_\xi \equiv \frac{\partial x}{\partial \xi} \qquad y_\xi \equiv \frac{\partial y}{\partial \xi} \qquad x_\eta \equiv \frac{\partial x}{\partial \eta} \qquad y_\eta \equiv \frac{\partial y}{\partial \eta} \tag{4.15}$$

These partial differentials can themselves be estimated, for the majority of the grid points, by second-order central-differencing. For example,

$$(x_\xi)_{j,k} \equiv \frac{1}{2\Delta\xi}(x_{j+1,k} - x_{j-1,k}) \tag{4.16}$$

For grid points at the boundaries of the mesh, one-sided three-point schemes can be used:

$$(y_\eta)_{1,k} \equiv \frac{-3y_{1,k} + 4y_{2,k} - y_{3,k}}{2\Delta\eta} \tag{4.17}$$

$$(y_\eta)_{jmax,k} \equiv \frac{3y_{jmax,k} - 4y_{jmax-1,k} + y_{jmax-2,k}}{2\Delta\eta} \tag{4.18}$$

Once the Jacobian is known, then the grid metrics are found:

$$\xi_x = Jy_\eta \qquad \xi_y = -Jx_\eta \qquad \eta_x = -Jy_\xi \qquad \eta_y = Jx_\xi \tag{4.19}$$

For convenience, a grid spacing of unity ($\Delta\xi=\Delta\eta=1$) is used for the transformed coordinate system.

4.4 Navier-Stokes Equations in Generalized Coordinate Form

After the grid metrics are found, the Navier-Stokes equations are transformed by substituting for the differentials in physical space with equivalent differentials in computational space, using the chain rule of differentiation. For example, if Q is some physical quantity, then the differential $\frac{\partial Q}{\partial x}$ is replaced, using the relation

$$\frac{\partial Q}{\partial x} = \xi_x \frac{\partial Q}{\partial \xi} + \eta_x \frac{\partial Q}{\partial \eta}. \tag{4.20}$$

After all the differentials are transformed, with some algebraic manipulation the conservation equations can be written as

$$\frac{\partial Q}{\partial \tau} + \frac{\partial}{\partial \xi}(F - F_V) + \frac{\partial}{\partial \eta}(G - G_V) + Z(H - H_V) = S \tag{4.21}$$

where the various terms are collected into the new matrices Q, F, G, and H as follows:

$$Q = J^{-1}\tilde{Q} \tag{4.22}$$

$$F = J^{-1}(\xi_t \tilde{Q} + \xi_x \tilde{F} + \xi_y \tilde{G}) \qquad F_V = J^{-1}(\xi_x \tilde{F}_V + \xi_y \tilde{G}_V) \tag{4.23}$$

$$G = J^{-1}(\eta_t \tilde{Q} + \eta_x \tilde{F} + \eta_y \tilde{G}) \qquad G = J^{-1}(\eta_x \tilde{F}_V + \eta_y \tilde{G}_V) \tag{4.24}$$

$$H = J^{-1}H \qquad H = J^{-1}H_V \tag{4.25}$$

Thus, the new matrix of conserved quantities is

$$Q = J^{-1}\begin{bmatrix} \rho_1 \\ \rho_2 \\ \cdots \\ \rho_N \\ \rho u \\ \rho v \\ E \end{bmatrix}, \tag{4.26}$$

the inviscid flux matrices F and G are given by

$$F = J^{-1}\begin{bmatrix} \rho_1 U \\ \rho_2 U \\ \cdots \\ \rho_N U \\ \rho u U + \xi_x p \\ \rho v U + \xi_y p \\ U(E+p) - \xi_t p \end{bmatrix} \qquad G = J^{-1}\begin{bmatrix} \rho_1 V \\ \rho_2 V \\ \cdots \\ \rho_N V \\ \rho u V + \eta_x p \\ \rho v V + \eta_y p \\ V(E+p) - \eta_t p \end{bmatrix} \tag{4.27}$$

and the inviscid axisymmetric terms of the conservations equations are collected into the matrix H:

$$H = \frac{J^{-1}}{y}\begin{bmatrix} \rho_1 v \\ \rho_2 v \\ \cdots \\ \rho_N v \\ \rho u v \\ \rho v^2 \\ v(E+p) \end{bmatrix} \tag{4.28}$$

Similarly, the viscous and conductive terms of the conservation equations are written:

$$F_V = J^{-1}\begin{bmatrix} 0 \\ 0 \\ \cdots \\ 0 \\ \xi_x\tau_{xx} + \xi_y\tau_{xy} \\ \xi_x\tau_{xy} + \xi_y\tau_{yy} \\ \xi_x\beta_x + \xi_y\beta_y \end{bmatrix} \qquad G_V = J^{-1}\begin{bmatrix} 0 \\ 0 \\ \cdots \\ 0 \\ \eta_x\tau_{xx} + \eta_y\tau_{xy} \\ \eta_x\tau_{xy} + \eta_y\tau_{yy} \\ \eta_x\beta_x + \eta_y\beta_y \end{bmatrix} \tag{4.29}$$

and the axisymmetric viscous source term is

$$H_V = \frac{J^{-1}}{y}\begin{bmatrix} 0 \\ 0 \\ \cdots \\ 0 \\ \tau_{xy} \\ \tau_{yy} - \tau_{\theta\theta} \\ \beta_y \end{bmatrix} \tag{4.30}$$

where

$$\begin{aligned} \beta_x &= u\tau_{xx} + v\tau_{xy} - q_x \\ \beta_y &= u\tau_{xy} + v\tau_{yy} - q_y \end{aligned} \tag{4.31}$$

The stress tensor can be calculated in terms of the generalized coordinates:

$$\tau_{xx} = -\frac{2}{3}\mu\left[-2\left(\xi_x u_\xi + \eta_x u_\eta\right) + \left(\xi_y v_\xi + \eta_y v_\eta\right) + \frac{v}{y}\right] \tag{4.32}$$

$$\tau_{yy} = -\frac{2}{3}\mu\left[\left(\xi_x u_\xi + \eta_x u_\eta\right) - 2\left(\xi_y v_\xi + \eta_y v_\eta\right) + \frac{v}{y}\right] \tag{4.33}$$

$$\tau_{\theta\theta} = -\frac{2}{3}\mu\left[\left(\xi_x u_\xi + \eta_x u_\eta\right) + \left(\xi_y v_\xi + \eta_y v_\eta\right) - 2\frac{v}{y}\right] \tag{4.34}$$

$$\tau_{xy} = \mu [(\xi_y u_\xi + \eta_y u_\eta) + (\xi_x v_\xi + \eta_x v_\eta)] \tag{4.35}$$

Note that the transformed equations, like the conservation equations, are expressed in a mathematically conservative form. Finite difference schemes require conservative forms of equations for accurate solution of fluid dynamics problems, especially when discontinuities (such as supersonic shocks) are involved. Numerical errors result from the approximation of any exact equation; these errors have the same effect as adding false source terms in the conservation equations. For the equations in non-conservative form, this error only increases with decreasing mesh spacing; that is, increasing the resolution of the computational grid degrades the obtained solution. For the equations in conservative form, however, the error does not increase with increasing resolution. Since the solution thus does not degrade with the addition of more grid points, this characteristic is known as the *telescoping property*.[27]

The set of equations is not yet complete, however. To fully specify the state of the gases, an equation of state is needed. Here, the gases are assumed to be thermally perfect, meaning that

$$p = \rho RT \tag{4.36}$$

where R is the gas constant. However, the gases are not assumed to be calorically perfect; models for the temperature variation of assorted gas properties will be discussed in the next chapter.

4.5 Unsteady Heat Conduction in Solids

The Navier-Stokes equations describe the purely fluid dynamic aspects of the flow. To also involve the interaction between the projectile surface and the surrounding

flow, the effects of material heating must be included. The high temperatures encountered in the complex shock system and combustion zones around the projectile heat the projectile, possibly even to its melting point. In turn, the changes in temperature and shape of the projectile surface affect the aerothermodynamics of the flow. To date, most theoretical analyses of the ram accelerator have treated the projectile as an adiabatic, unchanging surface. However, a more thorough analysis requires that the effects of heating not be ignored.

Obviously, the solid projectile material is stationary, so the solid heat flux is due only to conduction, which is governed by Fourier's Law:[29]

$$\vec{q} = -k\vec{\nabla}T \tag{4.37}$$

where k is the thermal conductivity, T is the temperature, and $\vec{q}$ is the heat flux vector. This equation defines only the heat flux vector. Unsteady changes in temperature are described by applying the conduction equation to an energy conservation equation:

$$\rho C\frac{\partial T}{\partial t} = -\vec{\nabla}\cdot\vec{q} = \vec{\nabla}\cdot(k\vec{\nabla}T) \tag{4.38}$$

where C is the heat capacity. A particularly convenient form of this equation results when the thermal conductivity is assumed to be constant. Then

$$\frac{\partial T}{\partial t} = \alpha\nabla^2 T \tag{4.39}$$

where the thermal diffusivity α is defined as

$$\alpha = \frac{k}{\rho C} \tag{4.40}$$

Analyses of unsteady heat conduction often use Eq. 4.39. However, since the conductivities of alloys depend on the temperature, and the temperature in ram accelerator projectiles varies greatly, the conductivity is not constant. Thus, the more accurate Eq. 4.38 must be used.

4.6 The Unsteady Heat Equation in Generalized Coordinate Form

In order to simplify the boundary conditions, Eq. 4.38 is transformed to a body-fitted coordinate system. This transformation is similar to the generalized-coordinate transformation used in solving the Navier-Stokes equations, except that the final form is more complex, due to the presence of second-order differentials. Care also must be taken to express Eq. 4.38 in a conservative manner.

According to Thompson[27], a numerically conservative form of the operator on the right hand side of Eq. 4.38 can be written as

$$\vec{\nabla} \cdot (k\vec{\nabla}T) = \frac{1}{\sqrt{g}} \sum_{i=1}^{3} \sum_{j=1}^{3} \frac{\partial}{\partial \xi^i} (k g^{ij} \sqrt{g} \frac{\partial T}{\partial \xi^j}) \tag{4.41}$$

where the geometric terms g and g^{ij} are defined by the equations

$$\frac{1}{\sqrt{g}} = \underline{a}^1 \cdot (\underline{a}^2 \times \underline{a}^3) \, . \tag{4.42}$$

$$g^{ij} = \underline{a}^i \cdot \underline{a}^j \tag{4.43}$$

Here $\underline{a}^i$ are known as contravariant base vectors, defined by

$$\underline{a}^i \equiv \vec{\nabla} \xi^i \, . \tag{4.44}$$

The gradient operator can be expressed in either cartesian or cylindrical coordinates. In cartesian coordinates,

$$\vec{\nabla}\Phi = \frac{\partial \Phi}{\partial x}\hat{e}_x + \frac{\partial \Phi}{\partial y}\hat{e}_y + \frac{\partial \Phi}{\partial z}\hat{e}_z \tag{4.45}$$

while in cylindrical coordinates,

$$\vec{\nabla}\Phi = \frac{\partial \Phi}{\partial r}\hat{e}_r + \frac{1}{r}\frac{\partial \Phi}{\partial \theta}\hat{e}_\theta + \frac{\partial \Phi}{\partial z}\hat{e}_z \tag{4.46}$$

A more general form can be written to include both forms:

$$\vec{\nabla}\Phi = \frac{\partial \Phi}{\partial x}\hat{e}_x + \frac{\partial \Phi}{\partial y}\hat{e}_y + \left(\frac{1}{y^Z}\right)\frac{\partial \Phi}{\partial \theta}\hat{e}_\theta \tag{4.47}$$

For cartesian coordinates, Z=0, and the x, y, and θ of Eq. 4.47 equal the x, y, and z, respectively, of Eq. 4.45. For cylindrical coordinates, Z=1, and the x, y, and θ of Eq. 4.47 equal the z, r, and θ, respectively, of Eq. 4.46.

Thus, one finds

$$\underline{a}^1 = \xi_x e_x + \xi_y e_y + \left(\frac{1}{y^Z}\right)\xi_\theta e_\theta \tag{4.48}$$

$$\underline{a}^2 = \eta_x e_x + \eta_y e_y + \left(\frac{1}{y^Z}\right)\eta_\theta e_\theta \tag{4.49}$$

$$\underline{a}^3 = \zeta_x e_x + \zeta_y e_y + \left(\frac{1}{y^Z}\right)\zeta_\theta e_\theta. \tag{4.50}$$

Assuming planar (for cartesian coordinates) or axisymmetric (for cylindrical coordinates) geometry, then

$$\xi_\theta = \eta_\theta = \zeta_x = \zeta_y = 0 \tag{4.51}$$

and

$$\zeta_\theta = 1 \tag{4.52}$$

and so

$$\underline{a}^1 = \xi_x \hat{e}_x + \xi_y \hat{e}_y \tag{4.53}$$

$$\underline{a}^2 = \eta_x \hat{e}_x + \eta_y \hat{e}_y \tag{4.54}$$

$$\underline{a}^3 = \left(\frac{1}{y\bar{z}}\right) \hat{e}_\theta . \tag{4.55}$$

Then

$$\underline{a}^2 \times \underline{a}^3 = \begin{vmatrix} \hat{e}_x & \hat{e}_y & \hat{e}_\theta \\ \eta_x & \eta_y & 0 \\ 0 & 0 & \left(\frac{1}{y\bar{z}}\right) \end{vmatrix} = \hat{e}_x \eta_y \left(\frac{1}{y\bar{z}}\right) - \hat{e}_y \eta_x \left(\frac{1}{y\bar{z}}\right) \tag{4.56}$$

so

$$\frac{1}{\sqrt{g}} = (\xi_x \hat{e}_x + \xi_y \hat{e}_y) \cdot \left[\hat{e}_x \eta_y \left(\frac{1}{y\bar{z}}\right) - \hat{e}_y \eta_x \left(\frac{1}{y\bar{z}}\right) \right] \tag{4.57}$$

or

$$\frac{1}{\sqrt{g}} = (\xi_x \eta_y - \xi_y \eta_x) \left(\frac{1}{y\bar{z}}\right) . \tag{4.58}$$

Similarly,

$$g^{11} = \underline{a}^1 \cdot \underline{a}^1 = (\xi_x \hat{e}_x + \xi_y \hat{e}_y) \cdot (\xi_x \hat{e}_x + \xi_y \hat{e}_y) = \xi_x^2 + \xi_y^2 \tag{4.59}$$

$$g^{22} = \underline{a}^2 \cdot \underline{a}^2 = (\eta_x \hat{e}_x + \eta_y \hat{e}_y) \cdot (\eta_x \hat{e}_x + \eta_y \hat{e}_y) = \eta_x^2 + \eta_y^2 \tag{4.60}$$

$$g^{33} = \underline{a}^3 \cdot \underline{a}^3 = (\frac{1}{yZ}) \hat{e}_\theta) \cdot (\frac{1}{yZ}) \hat{e}_\theta) = \frac{1}{y^2 Z} \tag{4.61}$$

$$g^{12} = \underline{a}^1 \cdot \underline{a}^2 = (\xi_x \hat{e}_x + \xi_y \hat{e}_y) \cdot (\eta_x \hat{e}_x + \eta_y \hat{e}_y) = \xi_x \eta_x + \xi_x \eta_y = g^{21} \tag{4.62}$$

$$g^{13} = g^{31} = g^{23} = g^{32} = 0 \tag{4.63}$$

With the assumption of two-dimensionality or axisymmetry, differentials with respect to the third coordinate θ equal zero, simplifying Eq. 4.41:

$$\begin{aligned}
\vec{\nabla} \cdot (k\vec{\nabla}T) &= \frac{1}{\sqrt{g}} \sum_{i=1}^{2} \sum_{j=1}^{2} \frac{\partial}{\partial \xi^i} (k g^{ij} \sqrt{g} \frac{\partial T}{\partial \xi^j}) \\
&= \frac{1}{\sqrt{g}} \Big[\frac{\partial}{\partial \xi} (k g^{11} \sqrt{g} \frac{\partial T}{\partial \xi}) + \frac{\partial}{\partial \xi} (k g^{12} \sqrt{g} \frac{\partial T}{\partial \eta}) \\
&\quad + \frac{\partial}{\partial \eta} (k g^{21} \sqrt{g} \frac{\partial T}{\partial \xi}) + \frac{\partial}{\partial \eta} (k g^{22} \sqrt{g} \frac{\partial T}{\partial \eta}) \Big] \\
&= \frac{1}{\sqrt{g}} \Big[\frac{\partial}{\partial \xi} (k (\xi_x^2 + \xi_y^2) \sqrt{g} \frac{\partial T}{\partial \xi}) + \frac{\partial}{\partial \xi} (k (\xi_x \eta_x + \xi_x \eta_y) \sqrt{g} \frac{\partial T}{\partial \eta}) \\
&\quad + \frac{\partial}{\partial \eta} (k (\xi_x \eta_x + \xi_x \eta_y) \sqrt{g} \frac{\partial T}{\partial \xi}) + \frac{\partial}{\partial \eta} (k (\eta_x^2 + \eta_y^2) \sqrt{g} \frac{\partial T}{\partial \eta}) \Big]
\end{aligned} \tag{4.64}$$

Defining

$$c_1 \equiv k\sqrt{g} (\xi_x^2 + \xi_y^2) \tag{4.65}$$

$$c_2 \equiv k\sqrt{g} (\eta_x^2 + \eta_y^2) \tag{4.66}$$

$$c_3 \equiv k\sqrt{g}\,(\xi_x \eta_x + \xi_x \eta_y) \tag{4.67}$$

and substituting Eqs. 4.64-4.67 into Eq. 4.38 gives the unsteady heat equation for generalized coordinates.

$$\rho C \frac{\partial T}{\partial t} = \frac{1}{\sqrt{g}}\left[\frac{\partial}{\partial \xi}\left(c_1 \frac{\partial T}{\partial \xi}\right) + \frac{\partial}{\partial \eta}\left(c_2 \frac{\partial T}{\partial \eta}\right) + \frac{\partial}{\partial \eta}\left(c_3 \frac{\partial T}{\partial \xi}\right) + \frac{\partial}{\partial \xi}\left(c_3 \frac{\partial T}{\partial \eta}\right)\right] \tag{4.68}$$

5. Numerical Methods

5.1 Introduction

The systems of differential equations that describe gas dynamics and heat conduction are impractical to solve analytically. Here, finite-difference approximations of the equations will be solved instead. In general, these solutions can be obtained either by explicit or implicit methods.

5.2 Navier-Stokes Equations: Explicit vs. Implicit methods

The choice of the computational method directly affects the amount of computation time necessary to complete a calculation. Although explicit methods are by far the simplest to understand and implement, the limit in the maximum allowed time step per iteration is far too small for any but the simplest studies of heat transfer in boundary layers. This limitation stems from the basic stability criterion for explicit CFD schemes: that the Courant number not exceed unity.[28] If this restriction is exceeded, the computation loses stability, resulting in non-physical "solutions." In generalized coordinates, this limit can be expressed as

$$\Delta t \leq \frac{1}{|U| + a\sqrt{\xi_x^2 + \xi_y^2} + |V| + a\sqrt{\eta_x^2 + \eta_y^2}} \tag{5.1}$$

where a is the local speed of sound at each grid point. Unfortunately, the desire to resolve the high gradients in boundary layers demands the use of highly clustered grids, for which the grid metric terms ξ_x, ξ_y, η_x, and η_y become extremely large, resulting in an extremely small time step at each iteration. Thus, an explicit algorithm often needs an unreasonably large number of iterations to advance in time.

In contrast, implicit schemes are generally not as restrictive in their stability limits, and hence can use much larger time steps. Thus, although much more difficult to implement than an explicit scheme, an implicit scheme is required in this analysis for any practical analysis.

5.3 Solving the Navier-Stokes Equations

The particular finite-difference method chosen for computer simulation of ram accelerator flow is a scheme proposed and used by Yee, Klopfer, and Montagne.[30] This scheme is Total Variation Diminishing (TVD), and is a fully implicit method. This particular method was chosen because of its accuracy and robustness, particularly in solving hypersonic blunt-body flows.[30,31]

The algorithm of Yee *et al.* is derived by manipulating the Navier-Stokes matrix equation into a two-parameter finite-difference form:

$$\begin{aligned}
&\Delta Q^{n}_{j,k} + \frac{h^{\xi}\theta}{1+\omega}\left(F^{n+1}_{j+\frac{1}{2},k} - F^{n+1}_{j-\frac{1}{2},k}\right) \\
&\quad + \left(\frac{h^{\eta}\theta}{1+\omega}\left(G^{n+1}_{j,k+\frac{1}{2}} - G^{n+1}_{j,k-\frac{1}{2}}\right) + \frac{h^{\xi}\theta}{1+\omega} ZH^{n+1}_{j,k}\right) \\
&\qquad = \frac{\omega}{1+\omega}\left(\Delta Q^{n-1}_{j,k}\right) - \frac{h^{\xi}(1-\theta)}{1+\omega}\left(F^{n}_{j+\frac{1}{2},k} - F^{n}_{j-\frac{1}{2},k}\right) \\
&\qquad\quad + -\frac{h^{\eta}(1-\theta)}{1+\omega}\left(G^{n}_{j,k+\frac{1}{2}} - G^{n}_{j,k-\frac{1}{2}}\right) - \frac{\Delta t(1-\theta)}{1+\omega} ZH^{n}_{j,k} \qquad (5.2)
\end{aligned}$$

In the above equation, θ and ω are parameters that affect the order of accuracy of the equation, j, k, and n are indices for the axial, radial, and time coordinates (that is, $x=j\Delta x$, $y=k\Delta y$, and time $t=n\Delta t$), and

$$h^{\xi} = \frac{\Delta t}{\Delta \xi} \tag{5.3}$$

$$h^{\eta} = \frac{\Delta t}{\Delta \eta}. \tag{5.4}$$

For generalized coordinates, $\Delta\xi$ and $\Delta\eta$ are generally equal to unity.

Note that unless otherwise specified, a variable with a noninteger index represents the algebraic mean of the values of the variable at the surrounding integer index values. Also, for convenience, integer indices are sometimes left out of an expression, but should be understood from context. Thus, for example,

$$\rho_{j+\frac{1}{2}} \equiv \frac{1}{2}(\rho_{j,k} + \rho_{j+1,k}) \tag{5.5}$$

In Eq. 5.2, the numerical fluxes F and G include flux limiter (a type of numerical dissipation) terms for stability; thus, instead of the form of Eqs. 4.23-4.24, these numerical fluxes can be expressed by

$$F_{j+\frac{1}{2},k} = \frac{1}{2}\left[\left[\left(\frac{\xi_x}{J}\right)_{j+\frac{1}{2}}(\tilde{F}_{j,k} + \tilde{F}_{j+1,k}) + \left(\frac{\xi_y}{J}\right)_{j+\frac{1}{2}}(\tilde{G}_{j,k} + \tilde{G}_{j+1,k})\right]\right.$$
$$\left. + \left(\frac{\xi_t}{J}\right)_{j+\frac{1}{2}}(\tilde{Q}_{j,k} + \tilde{Q}_{j+1,k}) + \frac{(R\Phi)_{j+\frac{1}{2},k}}{J_{j+\frac{1}{2},k}}\right] \tag{5.6}$$

and

$$G_{j,k+\frac{1}{2}} = \frac{1}{2}\left[\left(\frac{\eta_x}{J}\right)_{k+\frac{1}{2}} (\tilde{F}_{j,k} + \tilde{F}_{j,k+1}) + \left(\frac{\eta_y}{J}\right)_{k+\frac{1}{2}} (\tilde{G}_{j,k} + \tilde{G}_{j,k+1}) \right] + \left(\frac{\eta_t}{J}\right)_{j+\frac{1}{2}} (\tilde{Q}_{j,k} + \tilde{Q}_{j,k+1}) + \frac{(R\Phi)_{j,k+\frac{1}{2}}}{J_{j,k+\frac{1}{2}}} \tag{5.7}$$

where

$$\left(\frac{\xi_x}{J}\right)_{j+\frac{1}{2}} = \frac{1}{2}\left(\frac{\xi_{x_{j,k}}}{J_{j,k}} + \frac{\xi_{x_{j+1,k}}}{J_{j+1,k}}\right) \tag{5.8}$$

$$\left(\frac{\xi_y}{J}\right)_{j+\frac{1}{2}} = \frac{1}{2}\left(\frac{\xi_{y_{j,k}}}{J_{j,k}} + \frac{\xi_{y_{j+1,k}}}{J_{j+1,k}}\right) \tag{5.9}$$

$$\left(\frac{\eta_x}{J}\right)_{k+\frac{1}{2}} = \frac{1}{2}\left(\frac{\eta_{x_{j,k}}}{J_{j,k}} + \frac{\eta_{x_{j,k+1}}}{J_{j,k+1}}\right) \tag{5.10}$$

$$\left(\frac{\eta_y}{J}\right)_{k+\frac{1}{2}} = \frac{1}{2}\left(\frac{\eta_{y_{j,k}}}{J_{j,k}} + \frac{\eta_{y_{j,k+1}}}{J_{j,k+1}}\right) \tag{5.11}$$

Note that $F=F(Q)$, $G=G(Q)$, etc. That is, the flux matrices are functions of the Q-matrix.

Here, the numerical dissipation is provided by the vector $R\Phi$. The vector Φ uses the same form as that given by Yee and Harten;[32] once defined, the $R\Phi$ is formed in a procedure similar to that used by Yee and Shinn.[33] The formation of $R\Phi$ is discussed in more detail in Appendix A.

Using a Taylor series expansion and retaining only terms of first order in ΔQ, the flux terms at time level $n+1$ can be expressed as

$$F^{n+1} = F^n + A^n \Delta Q^n \tag{5.12}$$

$$G^{n+1} = G^n + B^n \Delta Q^n \tag{5.13}$$

$$H^{n+1} = H^n + C^n \Delta Q^n \tag{5.14}$$

where $A \equiv \frac{\partial F}{\partial Q}$, $B \equiv \frac{\partial G}{\partial Q}$, and $C \equiv \frac{\partial H}{\partial Q}$, and are known as flux Jacobians. Except for the terms unique to axisymmetric flow, the forms of the flux Jacobians are similar to those used by Steger,[34] and are discussed in detail in Appendix B.

Substituting Eqs. 5.12-5.14 into Eq. 5.2 and collecting terms give

$$\begin{aligned}
\Delta Q^n_{j,k} &+ \frac{h^\varsigma \theta}{1+\omega}\left[(A\Delta Q)^n_{j+\frac{1}{2},k} - (A\Delta Q)^n_{j-\frac{1}{2},k} \right] \\
&+ \frac{h^\eta \theta}{1+\omega}\left[(B\Delta Q)^n_{j,k+\frac{1}{2}} - (B\Delta Q)^n_{j,k-\frac{1}{2}} \right] + \frac{\Delta t \theta}{1+\omega} Z (C\Delta Q)^n_{j,k} \\
&= \frac{\omega}{1+\omega}\Delta Q^{n-1}_{j,k} - \frac{h^\xi (1-\theta)}{1+\omega}\left(F^n_{j+\frac{1}{2},k} - F^n_{j-\frac{1}{2},k} \right) \\
&\quad - \frac{h^\eta (1-\theta)}{1+\omega}\left(G^n_{j,k+\frac{1}{2}} - G^n_{j,k-\frac{1}{2}} \right) - \frac{\Delta t (1-\theta)}{1+\omega} Z H^{n+1}_{j,k}
\end{aligned} \tag{5.15}$$

or, with

$$(A\Delta Q)^n_{j+\frac{1}{2},k} - (A\Delta Q)^n_{j-\frac{1}{2},k} \equiv \frac{1}{2}\left[(A\Delta Q)^n_{j+1,k} - (A\Delta Q)^n_{j-1,k} \right] \tag{5.16}$$

$$(B\Delta Q)^{n}_{j,k+\frac{1}{2}} - (B\Delta Q)^{n}_{j,k-\frac{1}{2}} \equiv \frac{1}{2}\left[(B\Delta Q)^{n}_{j,k+1} - (B\Delta Q)^{n}_{j,k-1}\right] \tag{5.17}$$

then

$$\begin{aligned}\left[I + \frac{h^{\xi}\theta}{1+\omega}\left(L^{\xi}_{j+\frac{1}{2},k} - L^{\xi}_{j-1/2,k}\right)\right.&\\ \left. + \frac{h^{\eta}\theta}{1+\omega}\left(L^{\eta}_{j,k+\frac{1}{2}} - L^{\eta}_{j,k-\frac{1}{2}}\right) + \frac{\Delta t\theta}{1+\omega}ZC^{n}_{j,k}\right]\Delta Q^{n}_{j,k}&\\ = \frac{\omega}{1+\omega}\Delta Q^{n-1}_{j,k} - \frac{h^{\xi}}{1+\omega}\left(F^{n}_{j+\frac{1}{2},k} - F^{n}_{j-\frac{1}{2},k}\right)&\\ - \frac{h^{\eta}}{1+\omega}\left(G^{n}_{j,k+\frac{1}{2}} - G^{n}_{j,k-\frac{1}{2}}\right) - \frac{\Delta t}{1+\omega}ZH^{n}_{jk}&\end{aligned} \tag{5.18}$$

where the operator L uses the nonstandard notation of Yee *et al.*:

$$L^{\xi}_{j+\frac{1}{2},k}E^{**} = \frac{1}{2}\left(A_{j+1,k}E^{**}_{j+1,k} - \Omega^{\xi}_{j+\frac{1}{2},k}E^{**}\right) \tag{5.19}$$

$$L^{\xi}_{j-\frac{1}{2},k}E^{**} = \frac{1}{2}\left(A_{j-1,k}E^{**}_{j-1,k} - \Omega^{\xi}_{j-\frac{1}{2},k}E^{**}\right) \tag{5.20}$$

$$L^{\eta}_{j,k+\frac{1}{2}}E^{***} = \frac{1}{2}\left(B_{j,k+1}E^{***}_{j,k+1} - \Omega^{\eta}_{j,k+\frac{1}{2}}E^{***}\right) \tag{5.21}$$

$$L^{\eta}_{j,k-\frac{1}{2}}E^{***} = \frac{1}{2}\left(B_{j,k-1}E^{***}_{j,k-1} - \Omega^{\eta}_{j,k-\frac{1}{2}}E^{***}\right) \tag{5.22}$$

and where

$$\Omega^{\xi}_{j+\frac{1}{2},k} E^{**} = R_{j+\frac{1}{2},k} \operatorname{diag}\left[\psi\left(\lambda^{l}_{j+\frac{1}{2}}\right)\right] R^{-1}_{j+\frac{1}{2},k} \left(E^{**}_{j+1,k} - E^{**}_{j,k}\right) \tag{5.23}$$

$$\Omega^{\eta}_{j,k+\frac{1}{2}} E^{***} = R_{j,k+\frac{1}{2}} \operatorname{diag}\left[\psi\left(\lambda^{l}_{k+\frac{1}{2}}\right)\right] R^{-1}_{j+\frac{1}{2},k} \left(E^{***}_{j,k+1} - E^{***}_{j,k}\right) \tag{5.24}$$

The term $\operatorname{diag}(\alpha^l)$ designates a diagonal matrix with elements α^l. Here λ^l are the eigenvalues of the flux jacobian matrices, and ψ is the function defined by

$$\psi(\lambda^l) = \begin{cases} |\lambda^l| & , \text{ if } |\lambda^l| \geq \varepsilon \\ \dfrac{(\lambda^l)^2 + \varepsilon^2}{2\varepsilon} & , \text{ if } |\lambda^l| < \varepsilon \end{cases} \tag{5.25}$$

where ε is a small number. The purpose of this function is to smooth the discontinuity in the slope of $|\lambda^l|$ near zero. Although the algorithm performs adequately using a constant ε, Yee *et al.* recommend a variable value for ε. Following their guidelines, the relation

$$\varepsilon^l = \varepsilon^l_o \left(|U| + |V| + \frac{a}{2}\left[\sqrt{\xi_x^2 + \xi_y^2} + \sqrt{\eta_x^2 + \eta_y^2}\right]\right) \tag{5.26}$$

was used, where ε^l_o is a small constant and U and V are the contravariant velocities.[30] Although the overall dissipation of this scheme is nonlinear, in general the larger the magnitude of the constant ε, the greater the amount of numerical dissipation added to the solution. Yee *et al.* use a constant value of ε^l_o; however, using different ε^l_o for each row l of the matrix form of the Navier-Stokes equations allows differing amounts of numerical dissipation to be added to each conservation equation. Thus, since molecular diffusion is not modeled in this analysis, a greater amount of numerical dissipation can

be added to the species density equations to maintain stability, and a lesser amount of numerical dissipation can be added the momentum and energy conservation equations, which already include turbulent diffusion terms.

Equation 5.18 is a block pentadiagonal matrix equation; generally, such equations are difficult to solve, requiring extremely large amounts of computer time and memory. Fortunately, a simplification can be made to this matrix equation by approximate factorization.[35] First, note that in general, for any matrices M_1 and M_2,

$$I + M_1 + M_2 + M_1 M_2 = (I + M_1)\,(I + M_2)\,. \tag{5.27}$$

If the terms of the matrix product $M_1 M_2$ are small, then

$$I + M_1 + M_2 \approx (I + M_1)\,(I + M_2) \tag{5.28}$$

In a similar manner, Eq. 5.18 can be approximately factored into the following form:

$$\begin{aligned}
&\left[I + \frac{h^{\eta}\theta}{1+\omega}\left(L^{\eta}_{j,k+\frac{1}{2}} - L^{\eta}_{j,k-\frac{1}{2}} \right) \right] \\
&\times \left[I + \frac{h^{\xi}\theta}{1+\omega}\left(L^{\xi}_{j+\frac{1}{2},k} - L^{\xi}_{j-\frac{1}{2},k} \right) + \frac{\Delta t\theta}{1+\omega} Z C^{n}_{j,k} \right] \Delta Q^{n}_{j,k} \\
&\qquad = \frac{\omega}{1+\omega}\Delta Q^{n-1}_{j,k} - \frac{h^{\xi}}{1+\omega}\left(\tilde{F}^{n}_{j+\frac{1}{2},k} - \tilde{F}^{n}_{j-\frac{1}{2},k} \right) \\
&\qquad\quad - \frac{h^{\eta}}{1+\omega}\left(\tilde{G}^{n}_{j,k+\frac{1}{2}} - \tilde{G}^{n}_{j,k-\frac{1}{2}} \right) - \frac{\Delta t}{1+\omega} Z \tilde{H}^{n}_{j,k}
\end{aligned} \tag{5.29}$$

For modest time steps, the error introduced by approximate factorization is sufficiently small.

Equation 5.29 is in a form suitable for implicit solution in alternating directions. That is, a matrix equation is solved implicitly over rows of points in the computational mesh, then over columns. Instead of a block pentadiagonal matrix equation, only two block tridiagonal matrix equations must be solved, which can be accomplished much more quickly. First, form

$$E^{*}_{j,k} = -\frac{h^{\xi}}{1+\omega}\left[\tilde{F}^{n}_{j+\frac{1}{2},k} - \tilde{F}^{n}_{j-\frac{1}{2},k}\right] - \frac{h^{\eta}}{1+\omega}\left[\tilde{G}^{n}_{j,k+\frac{1}{2}} - \tilde{G}^{n}_{j,k-\frac{1}{2}}\right] - \frac{\Delta t}{1+\omega} ZH^{n}_{j,k} + \frac{\omega}{1+\omega}\Delta Q^{n-1}_{j,k} \tag{5.30}$$

for every j,k of the Q matrix. Then, solve the block tridiagonal matrix equation

$$\left[I + \frac{h^{\eta}\theta}{1+\omega}L^{\eta}_{j,k+\frac{1}{2}} - \frac{h^{\eta}\theta}{1+\omega}L^{\eta}_{j,k-\frac{1}{2}}\right]E^{**} = E^{*} \tag{5.31}$$

for each row of the E^{**} matrix. That is, each solution of Eq. 5.31 results in a series of $E^{**}_{j,k}$'s, over all j but only for a single row k; Eq. 5.31 thus must be solved once for each value of k, i.e. each row.

After all the $E^{**}_{j,k}$'s are found, then solve a second block tridiagonal matrix equation,

$$\left[I + \frac{h^{\xi}\theta}{1+\omega}L^{\xi}_{j+\frac{1}{2},k} - \frac{h^{\xi}\theta}{1+\omega}L^{\xi}_{j-\frac{1}{2},k} + \frac{\Delta t\theta}{1+\omega}ZC^{n}_{j,k}\right]E^{***} = E^{**}, \tag{5.32}$$

for E^{***} by columns. That is, each solution of Eq. 5.32 results in a set of $E^{***}_{j,k}$'s, for all k over a single given j, and Eq. 5.32 must be solved once for each value of j, i.e. each

column. And, finally, noting that $E^{***} \equiv \Delta Q$, then the matrix of conserved quantities, Q, is updated to the next time level, $n+1$:

$$Q_{j,k}^{n+1} = Q_{j,k}^{n} + E_{j,k}^{***} . \tag{5.33}$$

5.4 Enthalpy Modeling

In the computer simulation, the gases are not modeled as calorically perfect; polynomial approximations for the relation of enthalpy with temperature are used:

$$e_i = R_i \left[(A_{1,i} - 1)\, T + A_{2,i} \frac{T^2}{2} + A_{3,i} \frac{T^3}{3} + A_{4,i} \frac{T^4}{4} + A_{5,i} \frac{T^5}{5} + A_{6,i} \right] \tag{5.34}$$

where e_i is the internal energy per unit mass at temperature T and R_i is the gas constant of the i^{th} species. The constants A_i for the gases used most often in the ram accelerator are shown in Table 4.[36]

Equation. 5.34 only gives the internal energy for a given species; for the whole mixture, the internal energy is a weighted function of the species energies:

$$e = \frac{1}{\rho} \sum_{i=1}^{N} \rho_i e_i \tag{5.35}$$

where ρ_i and ρ are the species and overall gas densities, respectively.

5.5 Modeling the Conductivity and Viscosity of Gas Mixtures

The accurate solution of the Navier-Stokes Equations requires valid models of the viscosity and thermal conductivity of the gas. For gases, both the thermal conductivity and the viscosity are highly temperature dependent, so their variability

Table 4. Enthalpy constants.

Temperature Range	Parameter	O_2	N_2	CH_4
300 K-1000 K	A_1	3.784	3.704	3.826
	A_2	$-3.023(10^{-3})$	$-2.422(10^{-3})$	$-3.979(10^{-3})$
	A_3	$9.949(10^{-6})$	$2.867(10^{-6})$	$2.456(10^{-5})$
	A_4	$-9.819(10^{-9})$	$-1.203(10^{-9})$	$-2.273(10^{-8})$
	A_5	$3.303(10^{-12})$	$-1.395(10^{-14})$	$-6.963(10^{-12})$
	A_6	$-1.064(10^{3})$	$-1.064(10^{3})$	$-1.014(10^{4})$
1000 K-5000 K	A_1	3.612	2.853	1.503
	A_2	$7.485(10^{-4})$	$1.602(10^{-3})$	$1.042(10^{-2})$
	A_3	$-1.982(10^{-7})$	$-6.294(10^{-7})$	$-3.918(10^{-6})$
	A_4	$3.375(10^{-11})$	$1.144(10^{-10})$	$6.778(10^{-10})$
	A_5	$-2.391(10^{-15})$	$-7.806(10^{-15})$	$-4.428(10^{-14})$
	A_6	$-1.198(10^{3})$	$-8.901(10^{2})$	$-9.979(10^{3})$

cannot be ignored in any ram accelerator simulation. Many equations exist to model thermal conductivity; the exponential model[37] is one of the most commonly used:

$$k = k_o \cdot \left(\frac{T}{T_o}\right)^n \tag{5.36}$$

where k is the thermal conductivity, T is the temperature, and n is an arbitrary constant. The subscript o refers to reference conditions; thus $k=k_o$ when $T=T_o$. The exponential model was used for the results shown in this paper because of its obvious simplicity, and availability of data of its arbitrary constants.

A similar model exists for the viscosity μ of a pure gas:[37]

$$\mu = \mu_o \cdot \left(\frac{T}{T_o}\right)^m \tag{5.37}$$

Again, the exponential model was chosen for its simplicity. The constants μ_o, k_o, and n for the gases used in the simulations presented in this paper are shown in Table 5.[37,38]

Table 5. Viscosity and conductivity constants

Gas	O_2	N_2	CH_4
μ_o (kg/m-s)	$1.919(10^{-5})$	$1.633(10^{-5})$	$1.199(10^{-5})$
m	0.69	0.67	0.87
k_o (W/m-K)	0.0244	0.0242	0.0242
n	0.84	0.74	1.30

Equations 5.36-5.37 refer to the conductivity of a pure gas. The ram accelerator, however, usually uses mixtures of gases. The conductivity of gas mixtures can be estimated using Wilkes' Mixing Rule:[39]

$$k_{mixture} = \sum_{i=1}^{N} \left(\frac{\rho_i}{\rho}\right) \frac{k_i}{\sum_{j=1}^{N} \left(A_{ij} \frac{\rho_j}{\rho}\right)} \tag{5.38}$$

where

$$A_{ij} = \frac{\left[1 + \sqrt{\frac{k_i}{k_j}}\sqrt{\frac{M_j}{M_i}}\right]^2}{\sqrt{8 + 8\frac{M_j}{M_i}}} \tag{5.39}$$

and M_i is the molecular weight of species i.

Similarly, for viscosity,

$$\mu_{mixture} = \sum_{i=1}^{N} \left(\frac{\rho_i}{\rho} \right) \frac{\mu_i}{\sum_{j=1}^{N} \left(B_{ij} \frac{\rho_j}{\rho} \right)} \tag{5.40}$$

where

$$B_{ij} = \frac{\left[1 + \sqrt{\frac{\mu_i}{\mu_j}} \sqrt{\frac{M_j}{M_i}} \right]^2}{\sqrt{8 + 8\frac{M_j}{M_i}}} \tag{5.41}$$

5.6 Turbulence modeling

The modeling of turbulence is a topic of current research. For simplicity, the Baldwin-Lomax model[40] was chosen for use in the computer program. As an algebraic "eddy viscosity" method, the Baldwin-Lomax model collects the effects of turbulence into single terms which are simply added to the laminar viscosity and conductivity of the gas. That is, the viscosity and conductivity given by

$$\mu = \mu_L + \mu_T \tag{5.42}$$

$$k = k_L + k_T \tag{5.43}$$

are used in the viscous flux terms, where μ_L and k_L are the laminar viscosity and conductivity, respectively, given in the previous section, and μ_T and k_T are the equivalent increases in viscosity and conductivity, respectively, which occur in the presence of turbulence. The details of the Baldwin-Lomax model, as well as the

modeling of the transition point between laminar and turbulent flow, are discussed in Appendix C.

5.7 Solving the Heat Equation

Fortunately, a simpler method can be used to solve the heat equation in the projectile solid than is used to solve the Navier-Stokes equations, due to the lack of fluid flow in the solid. As seen in Eq. 4.68, the unsteady conduction of heat in a solid is governed by

$$\rho C\frac{\partial T}{\partial t} = \frac{1}{\sqrt{g}}\left[\frac{\partial}{\partial \xi}(c_1\frac{\partial T}{\partial \xi}) + \frac{\partial}{\partial \eta}(c_2\frac{\partial T}{\partial \eta}) + \frac{\partial}{\partial \eta}(c_3\frac{\partial T}{\partial \xi}) + \frac{\partial}{\partial \xi}(c_3\frac{\partial T}{\partial \eta})\right]. \tag{5.44}$$

For numerical analysis, finite-difference differentials can be substituted for the exact differentials in the above equation. For example, the exact time differential can be replaced by a first-order finite-difference scheme:

$$\frac{\partial T}{\partial t} = \frac{(T_{j,k}^{n+1} - T_{j,k}^{n})}{\Delta t} \tag{5.45}$$

Similar substitutions for the other differentials result in the following finite-difference form of the unsteady heat equation:

$$\rho C\sqrt{g}\frac{T^{n+1}-T^{n}}{\Delta t} =$$

$$\left([c_1]_{j+\frac{1}{2},k}(T_{j+1,k}-T_{j,k}) - [c_1]_{j-\frac{1}{2},k}(T_{j,k}-T_{j-1,k}) \right)$$

$$+ \left([c_2]_{j,k+\frac{1}{2}}(T_{j,k+1}-T_{j,k}) - [c_2]_{j,k-\frac{1}{2}}(T_{j,k}-T_{j,k-1}) \right)$$

$$+ \frac{1}{2}\left([c_3]_{j,k+1}\frac{T_{j+1,k+1}-T_{j-1,k+1}}{2} - [c_3]_{j,k-1}\frac{T_{j+1,k-1}-T_{j-1,k-1}}{2} \right)$$

$$+ \frac{1}{2}\left([c_3]_{j+1,k}\frac{T_{j+1,k+1}-T_{j+1,k-1}}{2} - [c_3]_{j-1,k}\frac{T_{j-1,k+1}-T_{j-1,k-1}}{2} \right) \quad (5.46)$$

Rearranging terms gives the explicit solution for the temperature at time $(n+1)\Delta t$, based on the temperature at time $t=n\Delta t$.

$$\begin{aligned} T_{j,k}^{n+1} = T_{j,k}^{n} &+ \frac{\Delta t}{\rho C\sqrt{g}}\Big[[c_1]_{j+\frac{1}{2},k}(T_{j+1,k}^{n}-T_{j,k}^{n}) - [c_1]_{j-\frac{1}{2},k}(T_{j,k}^{n}-T_{j-1,k}^{n}) \\ &+ [c_2]_{j,k+\frac{1}{2}}(T_{j,k+1}^{n}-T_{j,k}^{n}) - [c_2]_{j,k-\frac{1}{2}}(T_{j,k}^{n}-T_{j,k-1}^{n}) \\ &+ \frac{1}{4}\Big(([c_3]_{j,k+1}+[c_3]_{j+1,k})T_{j+1,k+1}^{n} \\ &- ([c_3]_{j-1,k}+[c_3]_{j,k+1})T_{j-1,k+1}^{n} \\ &- ([c_3]_{j,k-1}+[c_3]_{j+1,k})T_{j+1,k-1}^{n} \\ &+ ([c_3]_{j-1,k}+[c_3]_{j,k+1})T_{j-1,k-1}^{n} \Big) \Big] \end{aligned} \quad (5.47)$$

This algorithm is very simple to implement, since the temperature T^{n+1} at a given mesh point can be found using only the known temperatures at time level n, and does not require knowledge of the solution at $n+1$ at any other mesh point.

Unfortunately, just as in the solution of the Navier-Stokes equations, the requirements of numerical stability limit the maximum time step between computational levels.

Again, an alternative to the explicit method is the fully implicit method, which is unconditionally stable, and has no stability constraint on the maximum time step used in numerical computations. To obtain the implicit form of the finite-difference equation, the unknown temperatures T^{n+1} are used instead of the known temperatures T^n on the right-hand-side of Eq. 5.46; then,

$$\begin{aligned}
&\left(\frac{\rho C\sqrt{g}}{\Delta t} + [c_1]_{j+\frac{1}{2},k} + [c_1]_{j-\frac{1}{2},k} + [c_2]_{j,k+\frac{1}{2}} + [c_2]_{j,k-\frac{1}{2}}\right) T^{n+1}_{j,k} \\
&\quad - [c_1]_{j+\frac{1}{2},k} T^{n+1}_{j+1,k} - [c_1]_{j-\frac{1}{2},k} T^{n+1}_{j-1,k} \\
&\quad - [c_2]_{j,k+\frac{1}{2}} T^{n+1}_{j,k+1} - [c_2]_{j,k-\frac{1}{2}} T^{n+1}_{j,k-1} \\
&- \frac{1}{4}\left(\left([c_3]_{j,k+1} + [c_3]_{j+1,k}\right) T^{n+1}_{j+1,k+1}\right. \\
&\quad - \left([c_3]_{j-1,k} + [c_3]_{j,k+1}\right) T^{n+1}_{j-1,k+1} \\
&\quad - \left([c_3]_{j,k-1} + [c_3]_{j+1,k}\right) T^{n+1}_{j+1,k-1} \\
&\quad \left. + \left([c_3]_{j-1,k} + [c_3]_{j,k+1}\right) T^{n+1}_{j-1,k-1}\right) \\
&\qquad = \left(\frac{\rho C\sqrt{g}}{\Delta t}\right) T^{n}_{j,k} \qquad (5.48)
\end{aligned}$$

In this method, the temperature at time step $n+1$ must be solved at all mesh points at once; that is, for M data points, a set of M equations must be solved simultaneously. For two-dimensional heat conduction, this problem means solving a novadiagonal matrix equation--a difficult task requiring very large amounts of computer memory and numerous mathematical operations. Thus, although stability does not

constrain the size of the time step, considerable work is needed to obtain the solution at successive iterations.

A compromise between the explicit and fully implicit methods is known as the Alternating Direction Implicit (ADI) method. Whereas the explicit method solves for the temperature one mesh point at a time, and the fully implicit method solves for all the temperatures at once, the ADI method solves for the temperature a row or a column at a time. To solve for a row of temperatures, in Eq. 5.46, all the terms involving differentials solely in the ξ-direction are associated with iteration $n+1/2$; they are the unknowns to be solved. All the other terms are associated with iteration n; they are assumed to be known, having been solved in the previous iteration. Thus, rearrange Eq. 5.46 as

$$
\begin{aligned}
- [c_1]_{j-\frac{1}{2},k}\, T^{n+1/2}_{j-1,k} + \left(\frac{\rho C \sqrt{g}}{\Delta t} + [c_1]_{j+\frac{1}{2},k} + [c_1]_{j-\frac{1}{2},k} \right) T^{n+1/2}_{j,k} \\
- [c_1]_{j+\frac{1}{2},k}\, T^{n+1/2}_{j+1,k} \\
= \; [c_2]_{j,k-\frac{1}{2}}\, T^{n}_{j,k-1} + \left(\frac{\rho C \sqrt{g}}{\Delta t} - [c_2]_{j,k+\frac{1}{2}} - [c_2]_{j,k-\frac{1}{2}} \right) T^{n}_{j,k} \\
+ [c_2]_{j,k+\frac{1}{2}}\, T^{n}_{j,k+1} \\
+ \frac{1}{4} \Big[\left([c_3]_{j,k+1} + [c_3]_{j+1,k} \right) T^{n}_{j+1,k+1} \\
- \left([c_3]_{j-1,k} + [c_3]_{j,k+1} \right) T^{n}_{j-1,k+1} \\
- \left([c_3]_{j,k-1} + [c_3]_{j+1,k} \right) T^{n}_{j+1,k-1} \\
+ \left([c_3]_{j-1,k} + [c_3]_{j,k+1} \right) T^{n}_{j-1,k-1} \Big]
\end{aligned}
\tag{5.49}
$$

Eq. 5.49 is a tridiagonal matrix equation, with all the unknowns on the left side: the solution gives the temperature at all points in row k. This method is systematically applied to every row k in the mesh, so that the temperature $T^{n+1/2}$ is found for every point in the mesh. Next, again rearrange Eq. 5.46, but this time as

$$
\begin{aligned}
-[c_2]_{j,k-\frac{1}{2}} T^{n+1}_{j,k-1} + \left(\frac{\rho C \sqrt{g}}{\Delta t} + [c_2]_{j,k+\frac{1}{2}} + [c_2]_{j,k-\frac{1}{2}} \right) T^{n+1}_{j,k} \\
- [c_2]_{j,k+\frac{1}{2}} T^{n+1}_{j,k+1} \\
= \quad [c_1]_{j-\frac{1}{2},k} T^{n+1/2}_{j-1,k} + \left(\frac{\rho C \sqrt{g}}{\Delta t} + [c_1]_{j+\frac{1}{2},k} + [c_1]_{j-\frac{1}{2},k} \right) T^{n+1/2}_{j,k} \\
+ [c_1]_{j+\frac{1}{2},k} T^{n+1/2}_{j+1,k} \\
+ \frac{1}{4} \Big[\left([c_3]_{j,k+1} + [c_3]_{j+1,k} \right) T^{n+1/2}_{j+1,k+1} \\
- \left([c_3]_{j-1,k} + [c_3]_{j,k+1} \right) T^{n+1/2}_{j-1,k+1} \\
- \left([c_3]_{j,k-1} + [c_3]_{j+1,k} \right) T^{n+1/2}_{j+1,k-1} \\
+ \left([c_3]_{j-1,k} + [c_3]_{j,k+1} \right) T^{n+1/2}_{j-1,k-1} \Big]
\end{aligned}
\tag{5.50}
$$

Like Eq. 5.49, Eq. 5.50 is a tridiagonal matrix equation, with all the unknown temperatures T^{n+1} on the left-hand-side of the equation. The solution of Eq. 5.50 gives the temperatures over all the points in column j; repeating over each column gives the temperatures at time $t = (n+1)\Delta t$ at every point in the computational mesh.

The solution method alternates between solving the temperatures by rows and solving them by columns, in order to eliminate bias in the solution resulting from having

one direction solved implicitly and the other direction solved explicitly; hence, the name of the algorithm.

For two-dimensional problems, the ADI method is known to be unconditionally stable for any size of time step.[41] Thus, the ADI method has some of the stability of the fully implicit method, but requires only the solution of tridiagonal matrix equations (a much simpler task than is necessary for the fully implicit method). Comparison of Eqs. 5.49 and 5.50 to Eq. 5.47 and to Eq. 5.48 shows that the ADI method is, indeed, an intermediate scheme between the explicit and implicit methods, and fortunately combines some of the strengths of both methods.

5.8 Boundary Conditions

There are several boundary conditions that must be considered. For the gas, conditions at the inflow, the outflow, and the tube wall need to be specified; for the solid, the conditions at the inner surface, the tip, and the rear of the nose also need to be specified. Finally, the most complex boundary condition, that at the gas-solid interface, must be properly set.

The gas inflow and outflow boundary conditions are relatively simple. Since ram accelerator projectiles travel supersonically, the inflow conditions are unaffected by the presence of the projectile, and are nearly identical to the initial conditions of the gases in the tube. The only adjustment arises from the acceleration of the reference frame, which travels with the projectile; this acceleration causes an increase in the inflow velocity, in the projectile frame of reference. The outflow boundary condition is even simpler, since subsonic flow occurs only in a thin zone at the bottom of the boundary layer. Because the computer simulations are performed over a region in which

the flow is mostly supersonic, the outflow conditions have little effect on upstream conditions; thus, a simple extrapolation of the flow properties from just inside the boundary suffices, and is not expected to significantly degrade the computational solution.

At the tube wall, the condition is essentially that of a solid adiabatic frictionless wall; from symmetry considerations, a similar boundary condition can be applied along the centerline of the tube. In the finite-volume formulation of Yee *et al.*, this task is accomplished by using a "reflection" scheme: at "ghost points" outside the computational mesh, fluxes are set in opposition to the fluxes of points within the mesh, ensuring that no mass, momentum, or energy crosses over the boundary. Using these reflected fluxes, the conditions on the boundary are found from the same finite-difference scheme as used in the interior.

On the projectile surface, the no-slip condition is enforced; that is, $u = v = 0$ along this boundary of the gas zone. The density boundary condition is set in a manner similar to that used on the tube wall.

The energy boundary condition at the interface between gas and solid is a more complex problem. Basically, the flux of energy, including heat transfer in both the gas and the solid, as well as viscous dissipation in the gas, must be properly modeled in applying conservation of energy. First assume a "composite" cell on the boundary, composed partly of gas, partly of solid, as shown in Fig. 10; although the cell is composed of both solid and gas, the entire cell is at a single temperature T. Then express the energy equation in conservative form, namely

$$\frac{\partial Q}{\partial t} = \frac{\partial F}{\partial \xi} + \frac{\partial G}{\partial \eta} + H \tag{5.51}$$

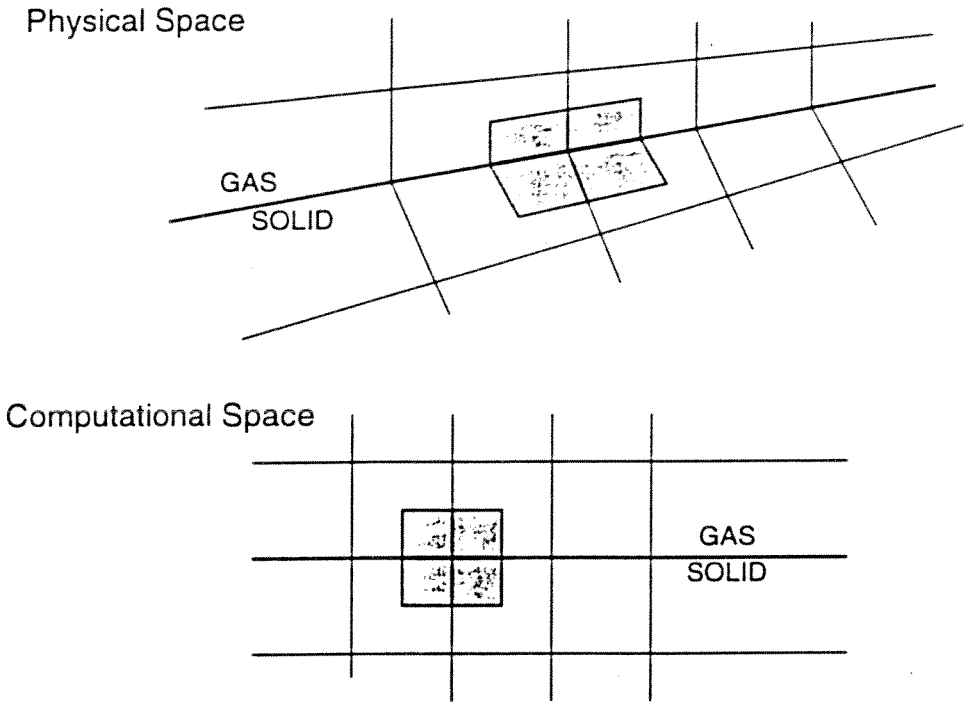

Figure 10. Composite gas-solid interface cell.

In this case, the energy stored in both the gas and the solid must be considered; thus,

$$dQ = \frac{1}{2}\left(dQ_{\text{gas}} + dQ_{\text{solid}}\right) \tag{5.52}$$

where

$$dQ_{\text{gas}} = d\left(J^{-1}_{\text{gas}} E_{\text{gas}}\right) \tag{5.53}$$

$$dQ_{\text{solid}} = d\left(J^{-1}_{\text{solid}} E_{\text{solid}}\right) \tag{5.54}$$

For a gas mixture, the energy is the sum of the energies of the components:

$$dE_{gas} = \sum_{i=1}^{N} dE_i \tag{5.55}$$

where the change in energy per unit volume is due both to changes in energy per unit mass and gas density:

$$dE_i = d(\rho_i e_i) = \rho_i de_i + e_i d\rho_i \tag{5.56}$$

Since e_i, the energy per unit mass of species i, is a function of temperature only, then

$$de_i = \frac{de_i}{dT} dT = C_{V,i} dT. \tag{5.57}$$

Also,

$$d\rho = \sum_{i=1}^{N} d\rho_i \tag{5.58}$$

so that Eq. 5.55 becomes

$$dE_{\text{gas}} = \sum_{i=1}^{N} (\rho_i C_{V,i} dT + e_i d\rho_i) \tag{5.59}$$

or, since

$$\sum_{i=1}^{N} \rho_i C_{V,i} \equiv \rho C_V \tag{5.60}$$

then

$$dE_{\text{gas}} = \rho C_V dT + \sum e_i d\rho_i \tag{5.61}$$

or, rearranging terms,

$$dT = \frac{1}{\rho C_V}\left(dE_{\text{gas}} - \sum e_i d\rho_i\right). \tag{5.62}$$

Now, for the solid,

$$dE_{\text{solid}} = \rho_s C_s dT \tag{5.63}$$

or, substituting for dT from Eq. 5.62,

$$dE_{\text{solid}} = \frac{\rho_s C_s}{\rho C_V}\left(dE_{\text{gas}} - \sum e_i d\rho_i\right) \tag{5.64}$$

Combining Eqs. 5.53, 5.54, and 5.64, and substituting into Eq. 5.52 give

$$dQ = \frac{1}{2}\left[\mathcal{J}^{-1}_{\text{gas}} dE_{\text{gas}} + \mathcal{J}^{-1}_{\text{solid}} \frac{\rho_s C_s}{\rho C_V}\left(dE_{\text{gas}} - \sum e_i d\rho_i\right)\right] \tag{5.65}$$

$$dQ = \frac{1}{2}\left[\mathcal{J}^{-1}_{\text{gas}}\left(1 + \frac{\mathcal{J}^{-1}_{\text{solid}}}{\mathcal{J}^{-1}_{\text{gas}}}\frac{\rho_s C_s}{\rho C_V}\right)dE_{\text{gas}} - \mathcal{J}^{-1}_{\text{gas}}\frac{\mathcal{J}^{-1}_{\text{solid}}}{\mathcal{J}^{-1}_{\text{gas}}}\frac{\rho_s C_s}{\rho C_V}\sum e_i d\rho_i\right] \tag{5.66}$$

$$dQ = \frac{1}{2}\left[\left(1 + \frac{\mathcal{J}^{-1}_{\text{solid}}}{\mathcal{J}^{-1}_{\text{gas}}}\frac{\rho_s C_s}{\rho C_V}\right)dQ_{gas} - \frac{\mathcal{J}^{-1}_{\text{solid}}}{\mathcal{J}^{-1}_{\text{gas}}}\frac{\rho_s C_s}{\rho C_V}\sum e_i dQ_i\right] \tag{5.67}$$

Or finally, returning back to Eq. 5.51,

$$\frac{\partial}{\partial t}\left(\frac{1}{2}\left[\left(1 + \frac{\mathcal{J}^{-1}_{\text{solid}}}{\mathcal{J}^{-1}_{\text{gas}}}\frac{\rho_s C_s}{\rho C_V}\right)dQ_{gas} - \frac{\mathcal{J}^{-1}_{\text{solid}}}{\mathcal{J}^{-1}_{\text{gas}}}\frac{\rho_s C_s}{\rho C_V}\sum e_i dQ_i\right]\right) = \frac{\partial F}{\partial \xi} + \frac{\partial G}{\partial \eta} + ZH \tag{5.68}$$

Thus, on the gas-solid interface, Eq. 5.68 is substituted for the standard energy conservation equation. However, the heat fluxes in both the gas and the solid must be

included in the solution; this task is accomplished by simply noting that since the generalized-coordinate cell is half-gas, half-solid,

$$F_{\text{interface}} = \frac{1}{2}\left(F_{\text{gas}} + F_{\text{solid}}\right) \tag{5.69}$$

where, as shown in Ch. 4,

$$F_{\text{gas}} = J_{\text{gas}}^{-1}\left[U(E+p) - \xi_t p - (\xi_x \beta_x + \xi_y \beta_y)\right] \tag{5.70}$$

and, converting the heat equation in the solid to a similar form,

$$F_{\text{solid}} = J_{\text{solid}}^{-1}\left[\xi_x q_x + \xi_y q_y\right]. \tag{5.71}$$

Similarly, the G-fluxes on each side of the interface can be defined:

$$G_{\text{gas side}} = J_{\text{gas}}^{-1}\left[V(E+p) - \eta_t p - (\eta_x \beta_x + \eta_y \beta_y)\right] \tag{5.72}$$

$$G_{\text{solid side}} = J_{\text{solid}}^{-1}\left[\eta_x q_x + \eta_y q_y\right] \tag{5.73}$$

With the fluxes now defined on the interface between gas and solid, the boundary conditions can be included in the matrix equations 5.30-5.32. Thus, the boundary conditions are solved simultaneously with the conditions in the rest of the flow in an implicit solution.

5.9 Initial Conditions

In each of the simulations, the initial conditions in the gas are of steady flow established around the projectile. The inflow velocity equals the experiment velocity of the projectile upon entrance to the ram accelerator section of the facility. The actual condition at entrance is not precisely known because the complex interaction between

the gases in the initial accelerator and ram accelerator sections, the Mylar diaphragm separating the two sections, and the projectile itself is not well understood. However, the supersonic projectile quickly leaves the entrance region of the ram accelerator, and so the error in the initial flow conditions is not expected to significantly affect the simulations.

The initial temperature in the simulated projectile is set to room temperature, 293 K. Although the actual initial temperature is unknown, the projectile is expected to start at close to room temperature. The temperature at the interface between the gas and the projectile solid is likewise set to room temperature. Considering the large rise in surface temperature expected over the duration of ram accelerator experiments, small errors in the initial temperature should not significantly affect the simulations.

6. Code Validation

6.1 Introduction

The algorithms, numerical models, and equations described in Chapters 4-5 were used to develop a computer program that simulates aerodynamic heating of projectiles in the ram accelerator. Before the simulations were performed, however, the code was tested, in order to verify that reasonably accurate results would be obtained. These tests involve testing the ability of the individual program components to solve the problems of supersonic flow, viscous flow, heat conduction, and structural integrity.

6.2 Inviscid Wedge Flow

The first test involves solving inviscid supersonic flow with oblique shocks. An oblique shock is shown schematically in Fig. 11. The conditions upstream and downstream of the shock in a thermally and calorically perfect gas are related by the following analytic equations:[42]

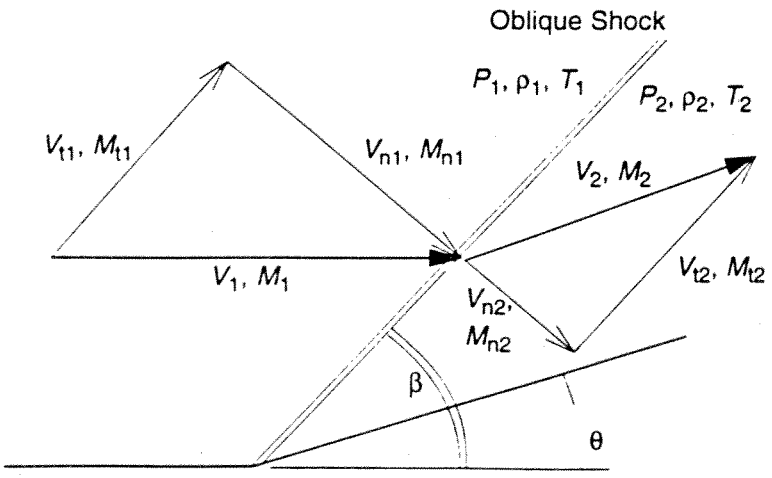

Figure 11. Oblique shock in supersonic flow.

$$M_{n1} = M_1 \sin\beta \tag{6.1}$$

$$\tan\theta = 2\cot\beta \frac{M_1^2 (\sin\beta)^2 - 1}{M_1^2 [\gamma + \cos(2\beta)] + 2} \tag{6.2}$$

$$M_{n2}^2 = \frac{1 + \frac{\gamma - 1}{2} M_{n1}^2}{\gamma M_{n1}^2 - \frac{\gamma - 1}{2}} \tag{6.3}$$

$$M_2 = \frac{M_{n2}}{\sin(\beta - \theta)} \tag{6.4}$$

$$\frac{\rho_2}{\rho_1} = \frac{(\gamma + 1) M_{n1}^2}{2 + (\gamma - 1) M_{n1}^2} \tag{6.5}$$

$$\frac{p_2}{p_1} = 1 + \frac{2\gamma}{\gamma + 1} (M_{n1}^2 - 1) \tag{6.6}$$

Here M is the Mach number, p is the pressure, ρ is the density, β and θ are the shock and flow turn angles, respectively, and γ is the ratio of specific heats. The subscripts 1 and 2 refer to conditions upstream and downstream of the shock, and the subscripts n and t refer to directions normal and tangential to the shock, respectively.

Using these equations, the case of supersonic flow in a converging duct was solved analytically. In this test case, the gas is nitrogen, the freestream velocity is 1150 m/s, the Mach number is 3.295, the pressure is 5.064×10^6 Pa (50 atm.), the density is 58.17 kg/m^3, the temperature is 293.2 K, and the turning angle is 10°. Fig. 12 shows a plot of the analytic shock position and the pressure contours from the corresponding CFD simulation. The analytical and computational solutions in the first two post-shock

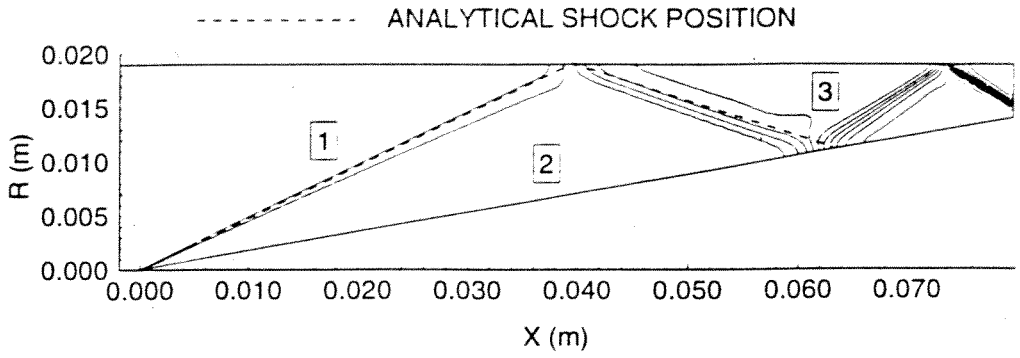

Figure 12. Pressure contours in a supersonic converging duct.

zones are compared in Table 6. The regions between each oblique shock contain uniform flow, and are labeled for reference.

Table 6. Comparison of analytic and CFD solutions to supersonic flow in a converging duct.

Region	Parameter	Analytical Solution (constant c_p)	CFD Solution (thermally perfect gas)
2	Mach Number	2.743	2.739
	Pressure (Pa)	$1.103(10^7)$	$1.100(10^7)$
	Density (kg/m^3)	100.1	99.59
	Temperature (K)	371	372
3	Mach Number	2.293	2.292
	Pressure (Pa)	$2.154(10^7)$	$2.145(10^7)$
	Density (kg/m^3)	160.1	159.2
	Temperature (K)	453	454

The agreement between the two solutions, both behind the first oblique shock and behind the reflected shock, is quite good. The solutions should differ slightly, due to the different thermodynamic models used; that is, the analytic solution assumes a constant value for the specific heat, while the computer solution models its variation with temperature. However, this effect is small, since even downstream of the first reflected shock, the Mach numbers, pressures, and densities of the two solutions differ by less than 1%. Thus, the computer code satisfactorily solves the flow conditions in a supersonic duct.

6.3 Supersonic Conical Flow

The next series of tests are of supersonic flow past a cone. The geometry is similar to that of the previous test, except a cone is substituted for the wedge. Although an exact analytical solution does not exist for this type of flow, both experimentally and numerically obtained solutions have been published by Taylor and Maccoll;[43,44] generally, wave angles for flows of up to about Mach 2 are from photographic experiments,[43] and wave angles for higher Mach number are obtained by numerical integration of the equations of motion.[44] The CFD code was run for three different cone angles, several flow velocities, and two different gases: an ideal gas and nitrogen. The ideal gas had a constant specific heat ratio of 1.4, while the nitrogen simulation used the thermodynamic models described previously in Ch. 5. The CFD and Taylor-Maccoll solutions are compared in Fig. 13.

Evidently, the CFD program satisfactorily solves supersonic flows over cones, as the correct shock angles are reproduced by the computer, for both the ideal gas and nitrogen gas cases.

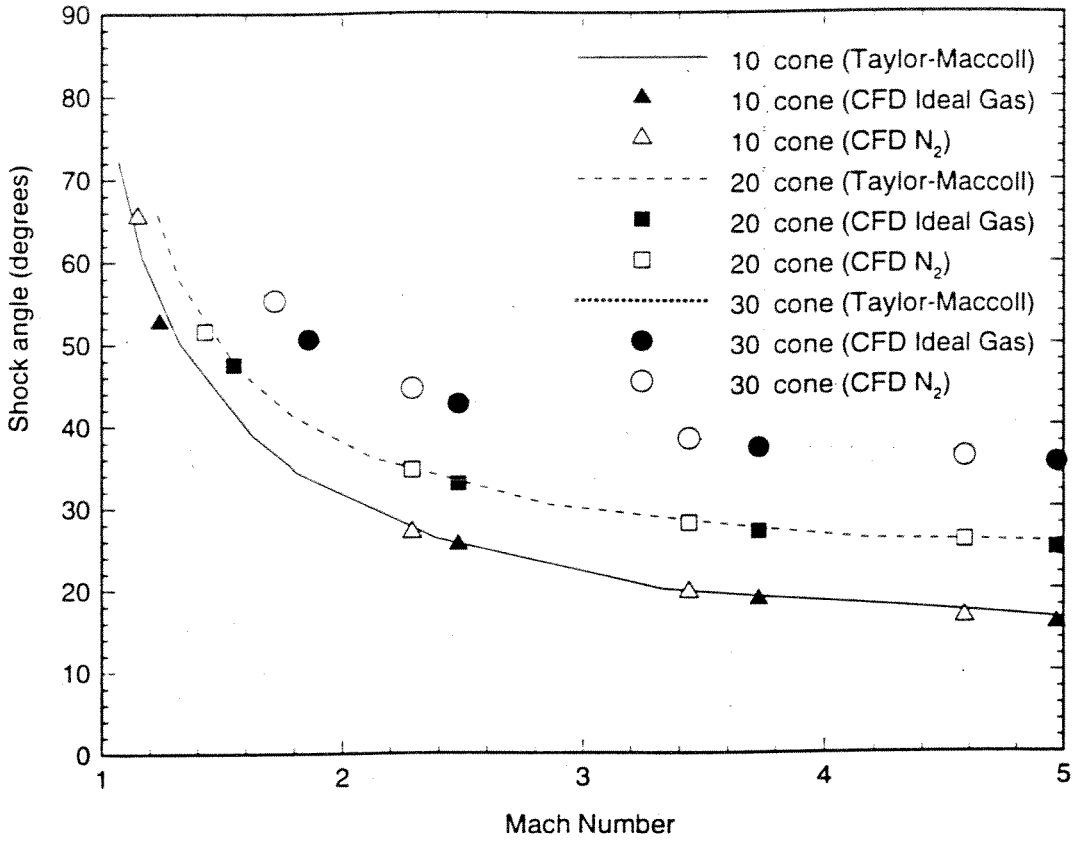

Figure 13. Comparison of conical shock angles computed by Taylor-Maccoll and CFD program.

6.4 Isothermal Flat Plate in Laminar Flow

The next test involves viscous laminar flow of air past a constant-temperature flat plate at zero angle of attack, as shown schematically in Fig.14. Using Crocco's method, Van Driest[45] solved the case of a plate at a temperature of 586.4 K in an air flow at 293.2 K and a velocity of 1376 m/s (Mach 4). The velocity and temperature profiles in the boundary layer obtained from the Van Driest and CFD solutions are compared in Figs. 15 and 16. The profiles shown are at a point 0.5 m from the front of the plate.

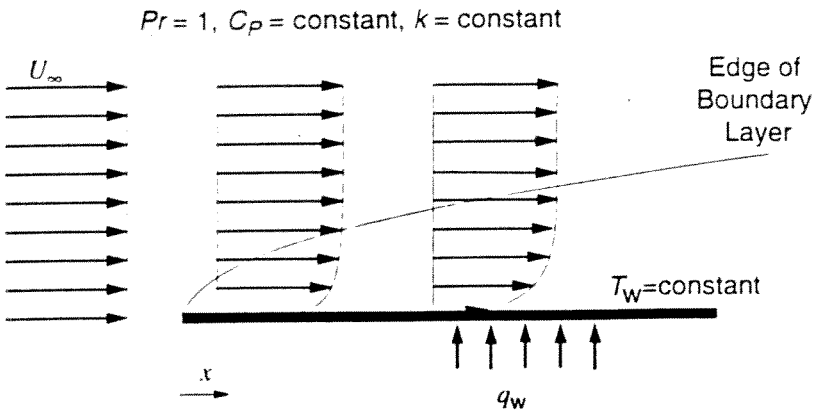

Figure 14. Flat plate heat transfer benchmark test.

Obviously, the profiles agree well. The CFD solution accurately reproduces the variation of both the velocity and the temperature throughout the boundary layer.

6.5 Isothermal Flat Plate in Turbulent Flow

The next test also involves an isothermal flat plate at zero angle of attack, except that now the flow is turbulent. Pappas[46] measured the turbulent flow over isothermal flat plates at various conditions, including the flow of air at Mach 2.27, a stagnation temperature of 118° F (320.9 K), and a wall-to-boundary-layer-edge temperature ratio, T_w/T_e, of 2.19, and a stagnation pressure of 30 psia (2.069×10^5 Pa). The normalized Mach number profile in the boundary layer is shown in Fig. 17, for both Pappas's data and the CFD turbulent flow solution. Pappas showed that the Mach number profiles at various points on the plate were self-similar, collapsing into a single curve when normalized in this manner, so the position on the plate is irrelevant. For comparison, the CFD laminar flow profile is also shown.

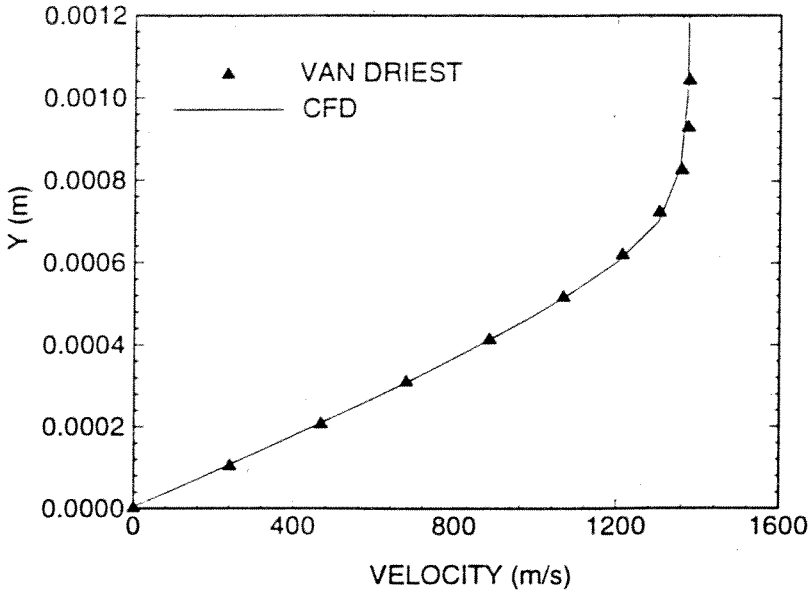

Figure 15. Velocity profile in laminar boundary layer for Van Driest[45] and CFD solutions (air, M_∞=4, T_∞=293.2 K).

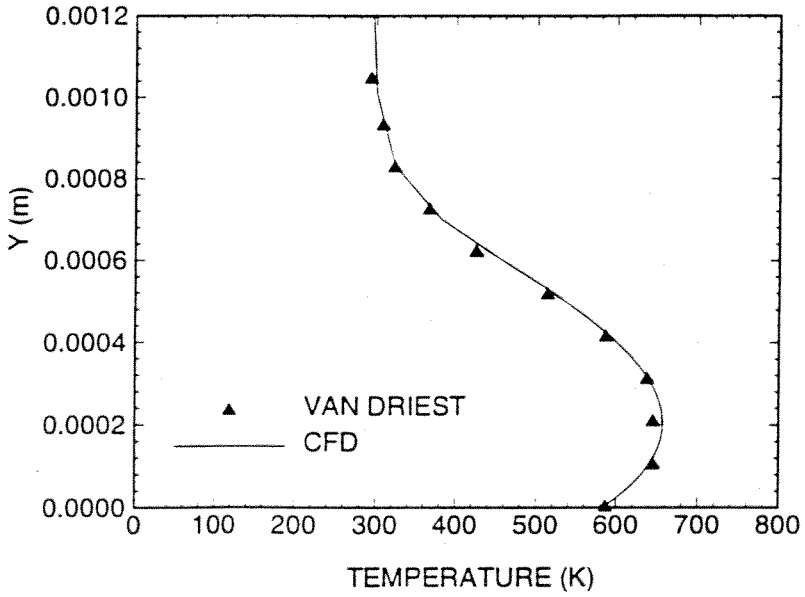

Figure 16. Temperature profile in laminar boundary layer for Van Driest[45] and CFD solutions (air, M_∞=4, T_∞=293.2 K).

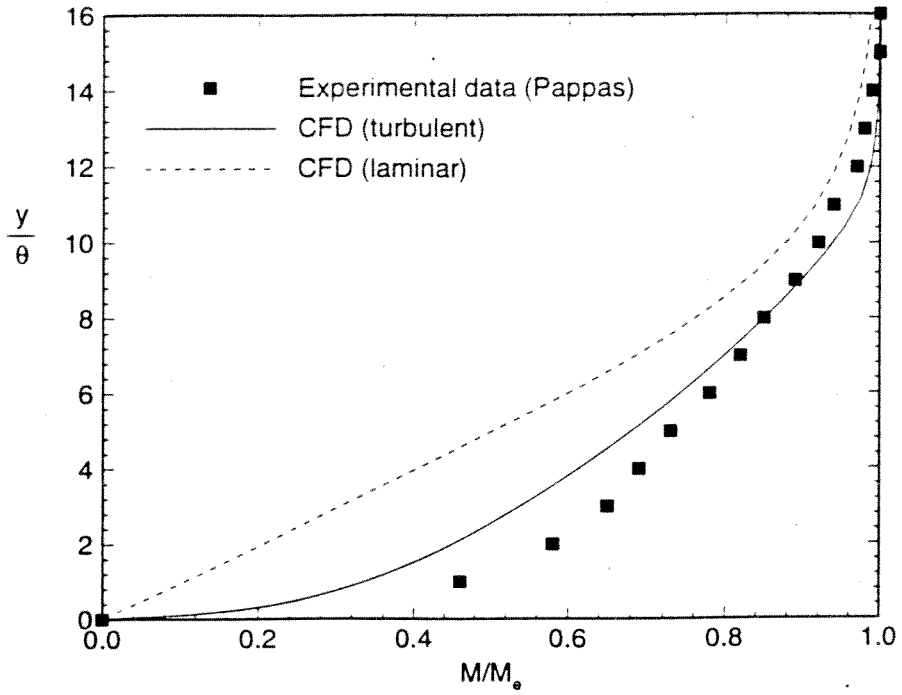

Figure 17. Mach number profile in turbulent boundary layer for Pappas[46] data and CFD solutions (air, M_∞=2.27, T_0=320.9 K, P_0=2.068 Pa, T_w/T_c=2.19).

The CFD solution is similar in character to the experimental data; both profiles show a much steeper gradient at the wall than the laminar flow profile. The slight deviation of the CFD solution from the experimental data results from the limitations of the simple Baldwin-Lomax algebraic turbulence model used in the computer program. However, the gradients at the wall are similar in magnitude, so the modeling of heat transfer to the wall should be sufficiently accurate for ram accelerator simulations.

6.6 One-Dimensional Heat Conduction

The test of the heat conduction solver involves simulation of unsteady one-dimensional heat conduction in a semi-infinite slab, shown schematically in Fig. 18.

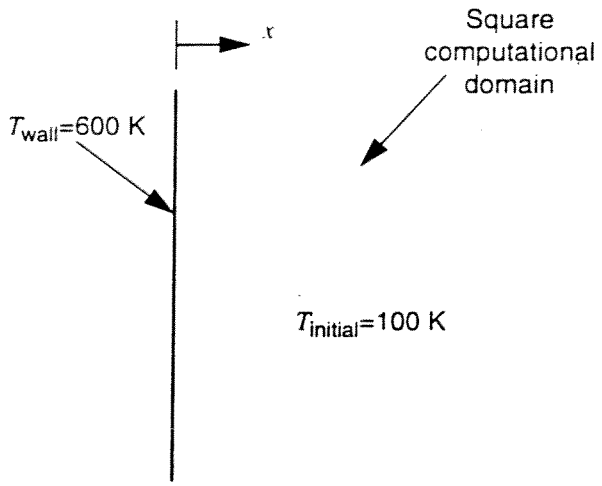

Figure 18. Unsteady heat conduction in a semi-infinite slab.

The semi-infinite slab at an initial temperature $T_{initial}$ has its boundary set to a different but constant temperature T_{wall}. Assuming $T_{wall}>T_{initial}$, then, as heat conducts from the boundary, the temperature in the slab rises in an unsteady manner. An analytical solution[47] for the temperature variation in time and space in the slab is

$$\frac{T(t,x) - T_{wall}}{T_{initial} - T_{wall}} = \text{erf}\left(\frac{x}{2\sqrt{\alpha t}}\right) \tag{6.7}$$

where α is the thermal diffusivity and erf is the error function:

$$\text{erf}(w) \equiv \frac{2}{\sqrt{\pi}} \int_0^w e^{-v^2} dv. \tag{6.8}$$

The A.D.I. method outlined in Chapter 5 is applied to a square region in the slab, with one side coincident with the slab face, as pictured in Fig. 18. The slab face is set to

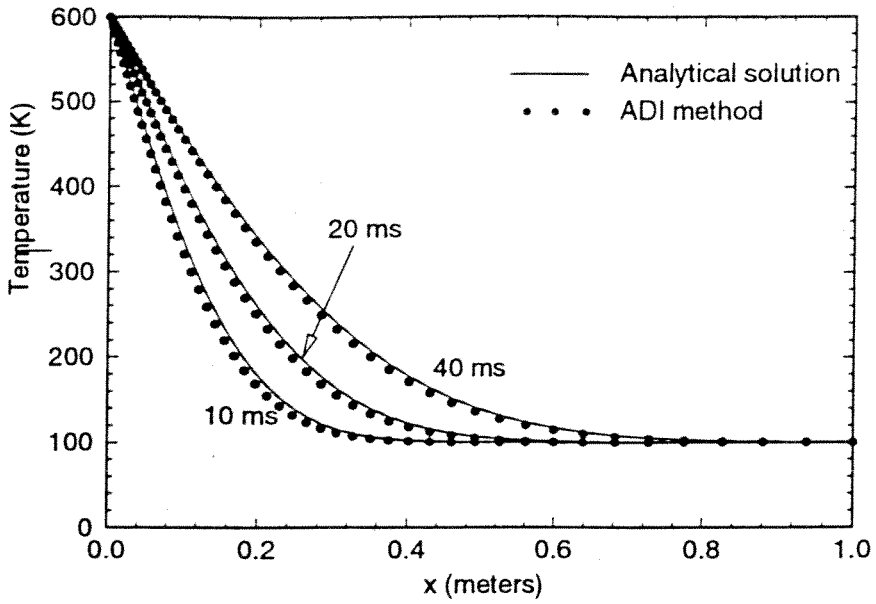

Figure 19. Comparison of analytical and computed temperatures over time in a semi-infinite slab with a thermal diffusivity of 1.0.

a constant temperature of 600 K, and the rest of the slab has an initial temperature of 100 K. The thermal conductivity of the slab is 1 W/m^2-s, the density is 1 kg/m^3, and the specific heat is 1 J/kg-°K, resulting in a thermal diffusivity of 1 m^2/s. From symmetry considerations, the top and bottom of the square can be treated as adiabatic walls. Thus, heat only flows from left to right—the case of one-dimensional heat conduction on a two-dimensional grid. The size of the square has been chosen to be large enough so that the temperature change on the right side over the course of the simulation is negligible. The analytical and computational solutions are compared in Fig. 19. Obviously, the computer solution of the unsteady variation of temperature in the slab agrees well with the analytical solution.

6.7 Test of structural analysis

The last test involves evaluating the structural integrity of a projectile nose. A finite-element computer code, known as Fred,[48] was used to calculate the principal stresses in an object with given boundary conditions. Once the principal stresses are known, then an assessment can be made of whether the object should experience structural failure, using the Von Mises failure criterion, which relates the state of stress to the yield stress.[49] Simply, the Von Mises criterion is that

$$(\sigma_1 - \sigma_2)^2 + (\sigma_2 - \sigma_3)^2 + (\sigma_3 - \sigma_1)^2 = 2\sigma_{yield}^2 \qquad (6.9)$$

when plastic yielding occurs, where σ_1, σ_2, and σ_3 are the principal stresses and σ_{yield} is the uniaxial yield stress of the object material. A useful non-dimensional parameter is then simply

$$\frac{\sqrt{(\sigma_1 - \sigma_2)^2 + (\sigma_2 - \sigma_3)^2 + (\sigma_3 - \sigma_1)^2}}{\sqrt{2}\sigma_{yield}} = \text{"Yield Parameter"}. \qquad (6.10)$$

A "yield parameter" of unity corresponds to a prediction of plastic yielding in the alloy.

The test of this method of analysis involves applying external pressure to a projectile nose, with only atmospheric pressure within its hollow interior, and comparing predicted with actual pressure at failure. In laboratory conditions, in a hydrostatic pressure test a magnesium alloy nose structurally failed at an external hydrostatic pressure of approximately 6.07×10^7 Pa (8800 psi). Using the Fred program, the maximum predicted yield parameter for a pressure of 5.86x107 Pa (8500 psi) is 0.97; for a pressure of 6.20x107 Pa (9000 psi), the maximum yield parameter is 1.03, indicating that the state of stress has exceeded the failure condition. At a pressure of 6.07x107 Pa

(the same pressure as that used to crush the nose in the laboratory), the maximum yield parameter is 1.004, indicating that the state of stress nearly exactly meets Von Mises' yield criterion; contours of the yield parameter in this case are shown in Fig. 20. Once a

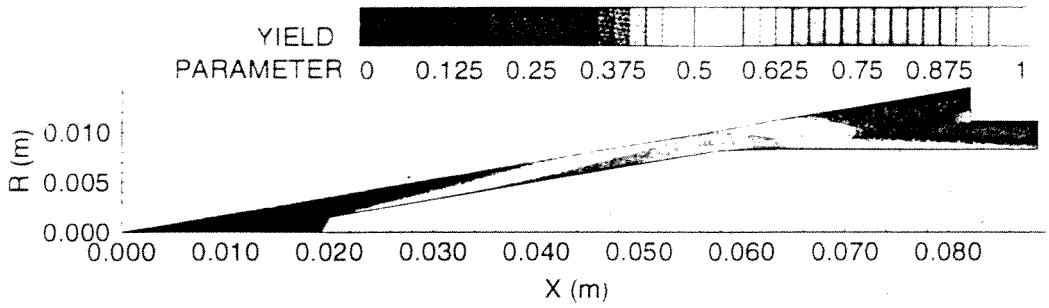

Figure 20. Computed yield parameter contours from simulated hydrostatic pressure test of magnesium projectile nose.

section of metal yields, the internal loads are concentrated into the remaining material that has not yet yielded. The expectation is then that the stress (the force per unit area) will increase in this section, eventually leading to collapse of the wall of the projectile nose. Thus, in this case, the correspondence between laboratory and computer results is excellent. Although the computed yield parameter varies somewhat with the placement of the points of the computational mesh within the boundaries of the simulated object, this method of analysis apparently can be used to predict the onset of failure in ram accelerator noses.

6.8 Summary of Tests

These simulations show that the individual components of the computer program match analytical solutions of simple test cases. The gas flow subroutines successfully simulate supersonic flow in a converging channel, supersonic conical flow, and

supersonic laminar and turbulent flow over flat plates. The heat conduction subroutines match the analytical solution of unsteady conduction in a solid. Finally, computer predictions of yielding under stress, applying the Von Mises yield criterion to the stress state given by the finite-element Fred code, have been shown to match a laboratory hydrostatic crush test. Now that the components have been shown to work separately, they can be combined into a single program, to simulate and analyze the state of the projectile nose in ram accelerator operation.

7. Computer Simulations of Ram Accelerator Experiments

7.1 Introduction

As previously noted, computer simulations can generate much more detailed data than laboratory experiments. The computer code can be used either to simulate prior ram accelerator experiments, in order to fill in gaps in data obtained and provide additional insight into the processes occurring in the ram accelerator, or to perform parametric studies which, for whatever reason, have not been performed or understood sufficiently in the laboratory. Presented here are data from numerical simulations of both prior experiments and as yet unperformed experiments, in a brief study of the effects of heat transfer to ram accelerator projectiles.

7.2 Simulations Of Laboratory Experiments

The projectile distance-time histories from laboratory experiments can be used to develop velocity-time profiles for the computer simulations. A seventh-order polynomial function models the position of the projectile over time in each experiment: the coefficients of the polynomial were found by minimizing the sum of squares of differences between the polynomial and the known positions of projectiles at recorded times. Each polynomial was then differentiated with respect to time to obtain a sixth-order polynomial that modeled the projectile velocity over time. Since the order of the polynomial is far less than the number of experimental positional data points, the polynomial tends to smooth any high-frequency oscillations occurring in central-difference calculations of velocities.

Aluminum Noses: HS 1062 & HS 1064

The first experiment to be simulated is HS 1062, which used a projectile made entirely of aluminum. The polynomial model of the projectile velocity history is shown in Fig. 21; for comparison, the velocities obtained from centrally-differencing the

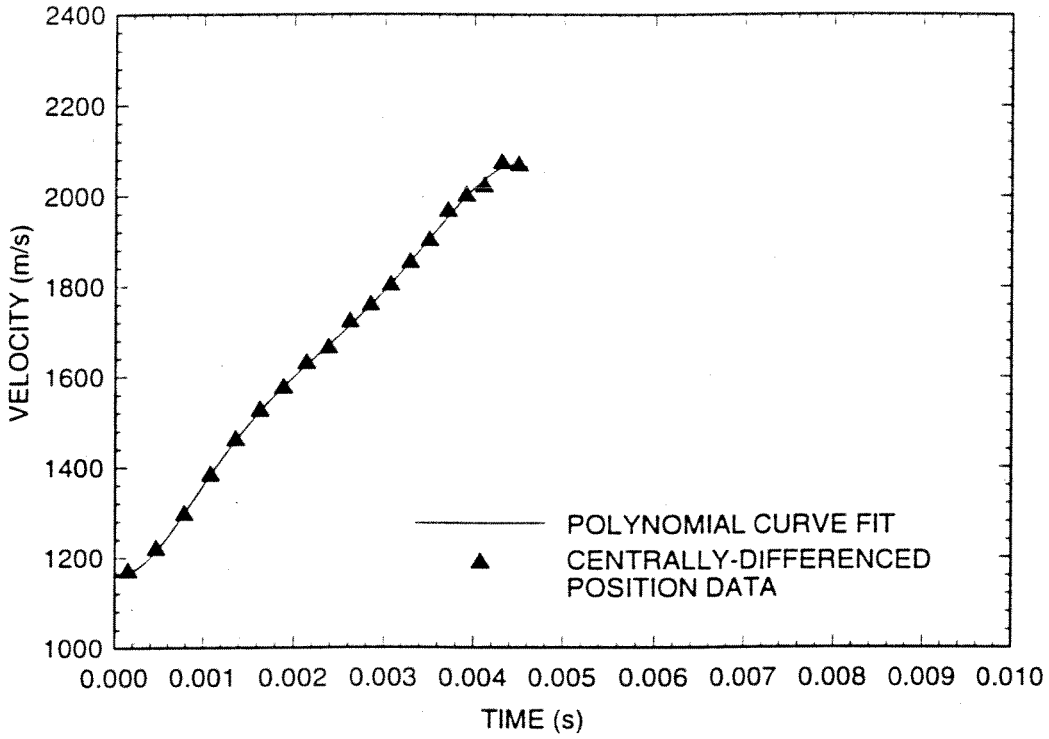

Figure 21. Velocity history of projectile in experiment HS 1062.

position data are also shown. The computer code used this polynomial model of velocity, along with the properties of the gases filling the ram accelerator tube, in its simulation of the heating of the projectile nose over the course of the experiment.

Figure 22 shows a diagram of the region in physical space simulated by the computer program. Since the projectile nose centered in the tube forms an axisymmetric configuration, the resulting gas flow and heat conduction are axisymmetric as well. The

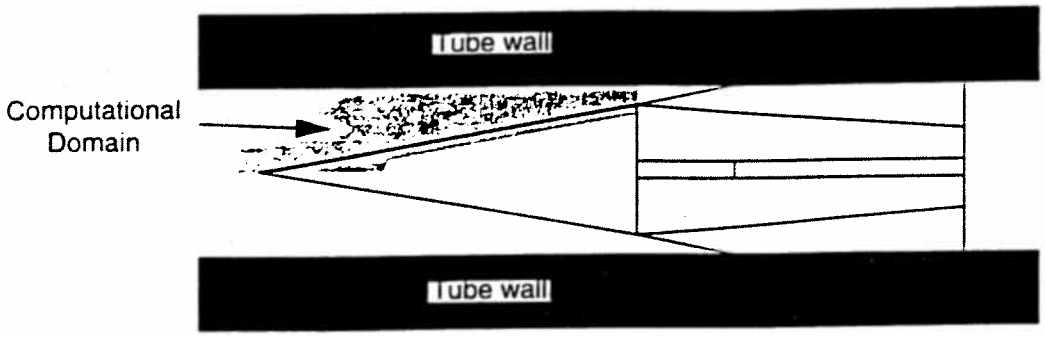

Figure 22. Physical region for computer simulation (domain shown in light gray).

conditions around the circumference are thus completely characterized by a computer solution in the small region shown. The computational grids used in simulating HS 1062 are shown in Fig. 23. For clarity, also pictured is a diagram showing the

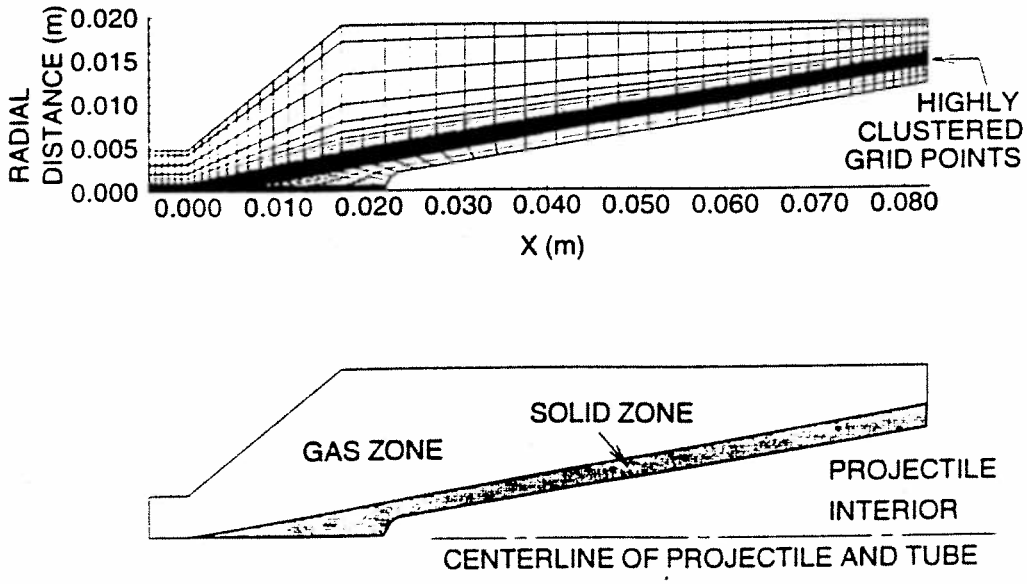

Figure 23. Computational mesh for simulation of experiments.

boundaries of each zone, without the highly clustered mesh. Small spacing between grid points near the gas-solid interface is necessary to resolve the gradients, particularly in temperature, in the extremely thin boundary layer of the projectile nose. Due to limitations in computer memory and speed, variable grid spacing is used. Thus, mesh points near the interface are clustered together, and points far from the interface are spread further apart, minimizing the total number of grid points necessary to cover the computational domain while still resolving the boundary layer. The mesh spacing in the gas zone in the radial direction ranges from a maximum of 3.75 mm in the freestream down to a minimum of approximately 1.4 μm in the boundary layer, and the spacing in the solid zone ranges from a maximum of 6.73 mm at the inner surface to 1.8 μm at the outer surface.

Note that the meshes extend only to the inner surface of the solid wall of the projectile nose. No attempt is made to model the heat transfer within the hollow chamber of the nose. The expected temperature gradients and thermal diffusivity of the air in the hollow chamber are much lower than those of the projectile alloy, so that the conductive heat flux in the chamber is very small. Also, the temperatures in the chamber are anticipated to remain close to room temperature, so that the radiative heat transfer within the chamber is insignificant. Thus, the heat flux within the chamber is negligible compared to the heat flux in the projectile solid, and so the inner surface is assumed to be adiabatic.

Figure 24 shows the computed temperatures in the flow and in the projectile at various times over the duration of the experiment. The contours in each plot range over the same temperature scale, in order to clearly illustrate the rise in temperature over time (however, the maximum temperature in the region shown is not necessarily equal to the

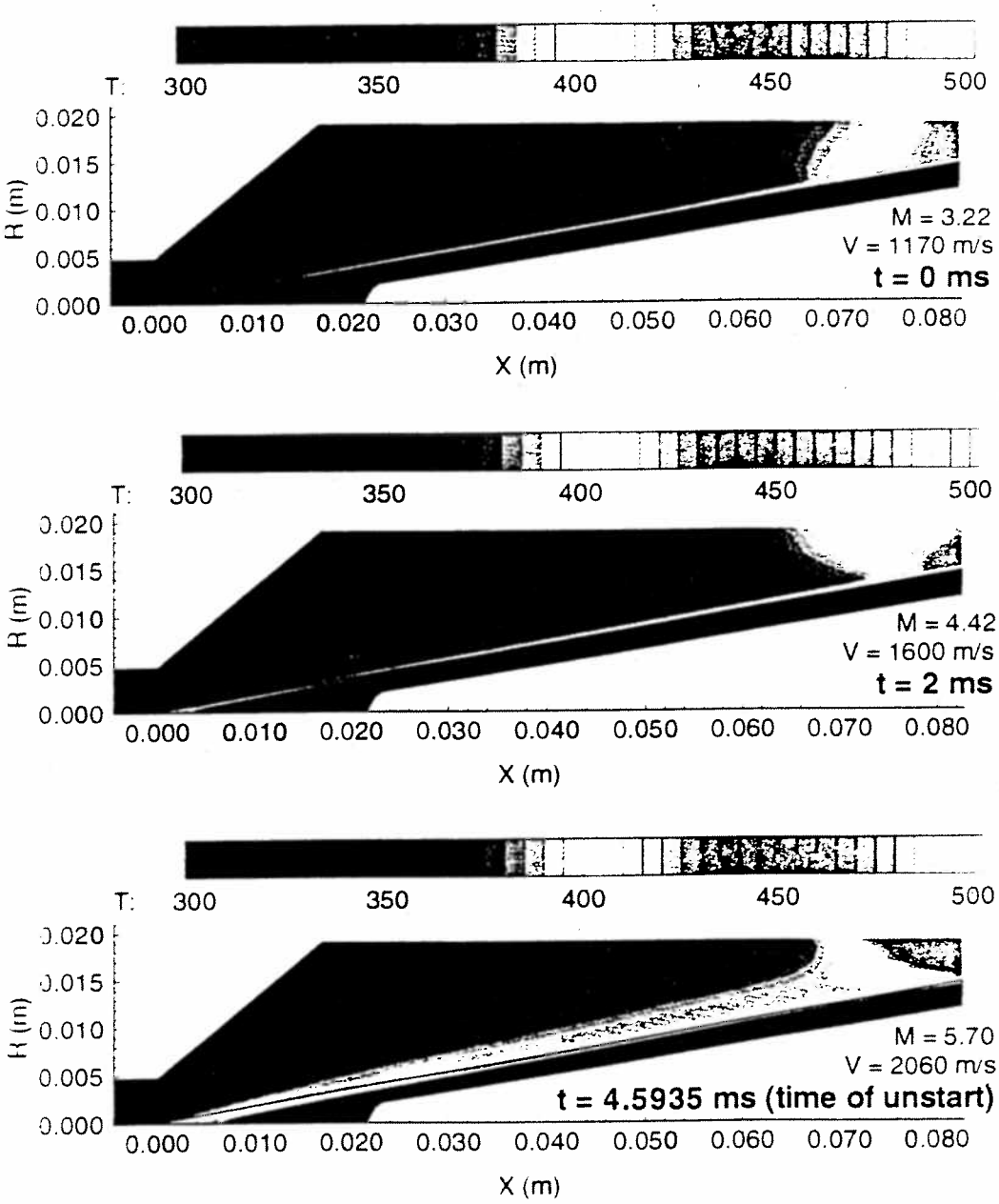

Figure 24. Temperature distribution in gas flow and projectile nose in simulation of HS 1062 (Al nose, Al body).

upper limit of the contour range). In the first few milliseconds, the oblique shocks are relatively weak, and the flow is not heated to a very high temperature. The reflection of the shock off the upper tube wall is more visible, impinging on the projectile surface just upstream of the throat (located at the far right of each figure). The visible curvature in the shock at the wall is due to the low resolution of the computational mesh away from the projectile. As time progresses and the projectile accelerates to higher Mach numbers, the shocks also grow stronger and hence more visible. The reflected shock moves further back towards the throat, and eventually the reflection barely impinges on the nose, just in front of the throat.

A close inspection of Fig. 24 reveals a thin hot boundary layer next to the projectile surface. Figures 25 and 26 shows typical temperature and velocity profiles, respectively, near the projectile surface at a location approximately 3 mm from the tip of the nose. As time progresses, the temperature in the boundary layer rises faster than the temperature just outside the boundary layer.

Close examination of Fig. 24 also shows that most of the heating of the alloy occurs in a thin layer at the surface of the projectile. The heat penetrates deepest at the tip of the nose, close to the front stagnation point. Except for this hot outer layer, the projectile does not experience a significant rise in temperature.

Figure 27 shows the surface temperature along the nose. Note that the abscissa is the distance along the surface, instead of the distance along the axis. Two local maxima in temperature can be seen: at the front (near the nose tip) and at the rear (near the projectile throat). Figure 28 shows the corresponding heat flux from the gas to the projectile, normal to the solid surface. The peaks in heat flux correspond to the regions with the highest temperatures: at the nose tip, where the boundary layer is thinnest and

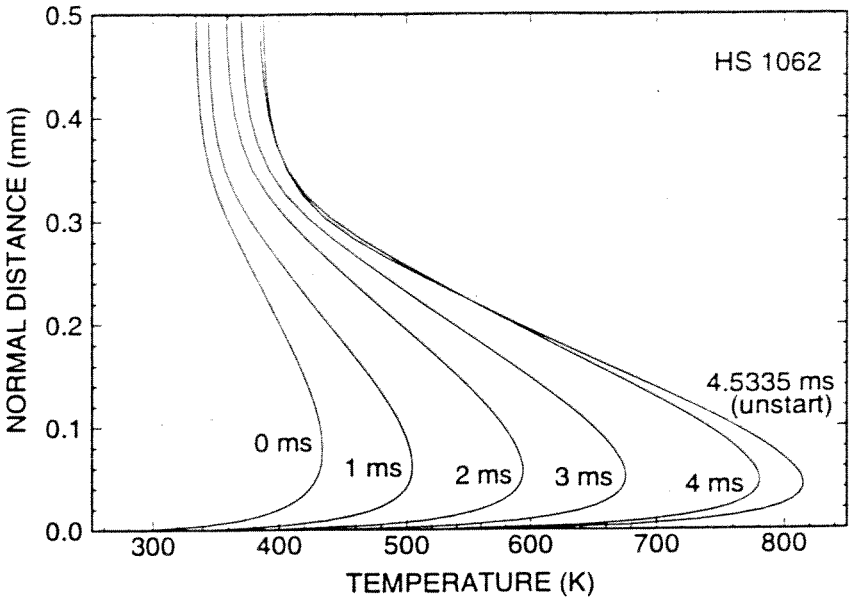

Figure 25. Temperature in boundary layer, 3 mm from nose tip, in simulation of HS1062 (Al nose, Al body).

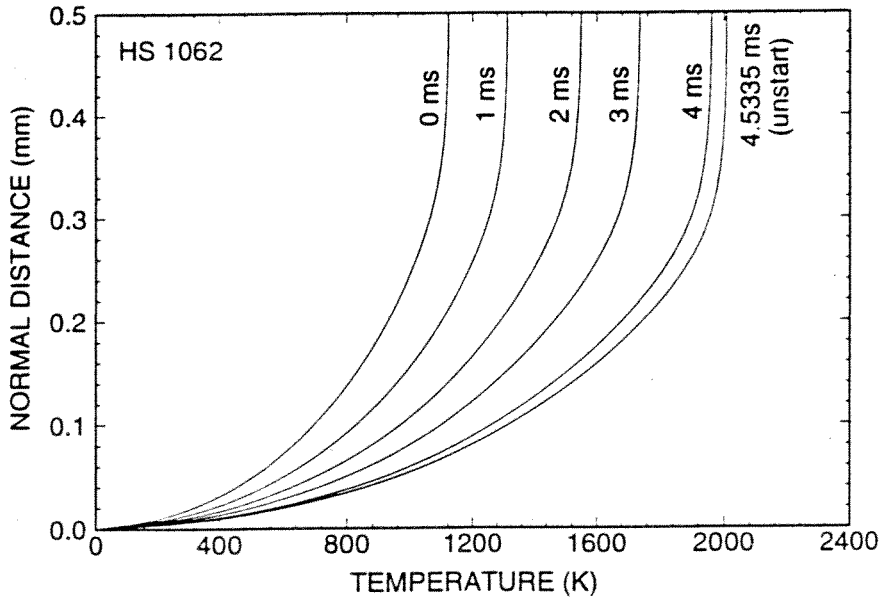

Figure 26. Velocity in boundary layer, 3 mm from nose tip, in simulation of HS 1062 (Al nose, Al body).

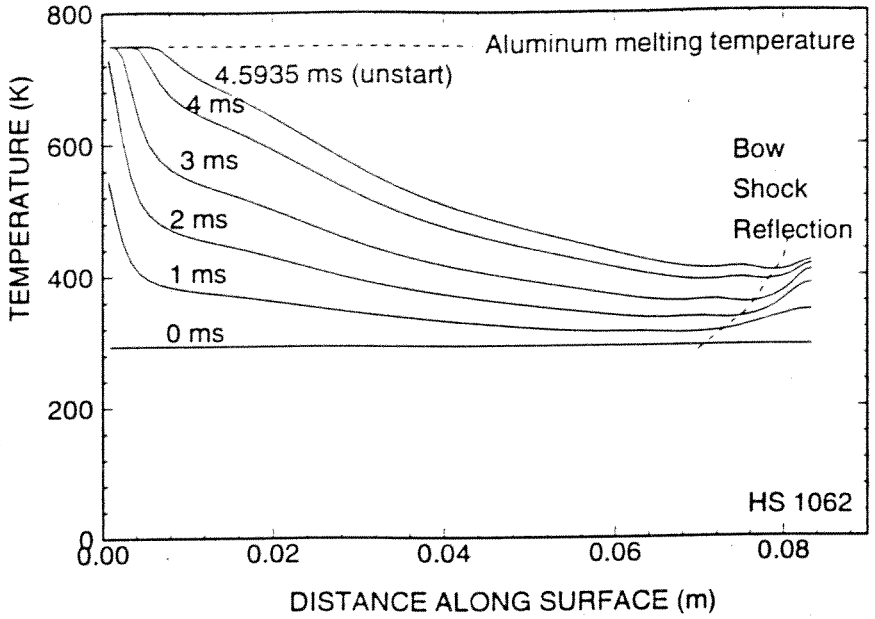

Figure 27. Surface temperature profiles of projectile nose in simulation of HS 1062 (Al nose, Al body).

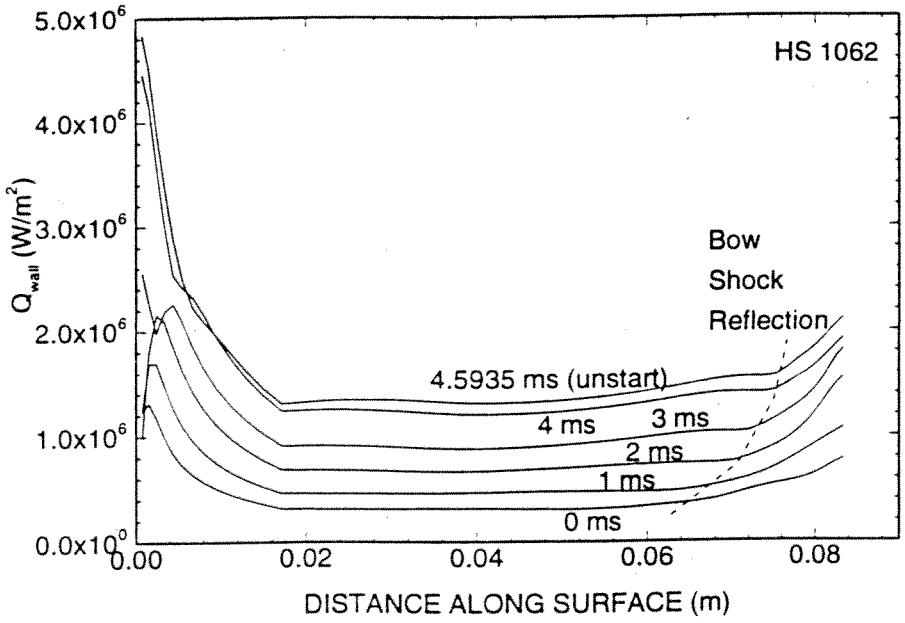

Figure 28. Variation of normal heat flux to surface of projectile nose in simulation of HS 1062 (Al nose, Al body).

the gradients are high, and just downstream of the reflected shock, where the gas has been shock-heated. Evidently, the computer simulation indicates that aerodynamic heating at the nose tip is more severe than that at the shock impingement, as expected. In fact, the nose tip reaches the melting temperature of the aluminum alloy at roughly three milliseconds after the start of the experiment, while the throat region rises only about 150 K in temperature.

The next figures illustrate the structural integrity of the projectile nose. Figure 29 shows contours of the yield parameter in the nose (as described in Ch. 6). Note that in these figures, the yield parameter in most of the nose never exceeds a level of 0.15. In fact, the highest stress level in the hollow section occurs at the beginning of the experiment, and corresponds to the point of contact of the reflected shock on the nose; as the projectile accelerates, the oblique shock angle decreases, moving the contact point further back towards the throat, where the projectile nose shell is reinforced by the end wall of the nose, and thus is better able to withstand external pressure. The conclusion is that, for a smoothly accelerating projectile, although the external pressure on the nose is greatest behind the reflected shock, the nose structure is unlikely to fail from just the shock pressure. (Note, however, that this conclusion does not take into account any balloting of the projectile within the tube (which would require a three-dimensional analysis), nor the severe stresses occurring during transit through the stage-separation diaphragms, nor the lesser stresses resulting from the acceleration of the projectile itself.)

However, a closer look shows that not all of the nose is free from damage. Careful examination of the nose tip, shown in Fig. 30, reveals that the stresses there meet the Von Mises failure criterion (which is to be expected, since Fig. 27 shows the tip

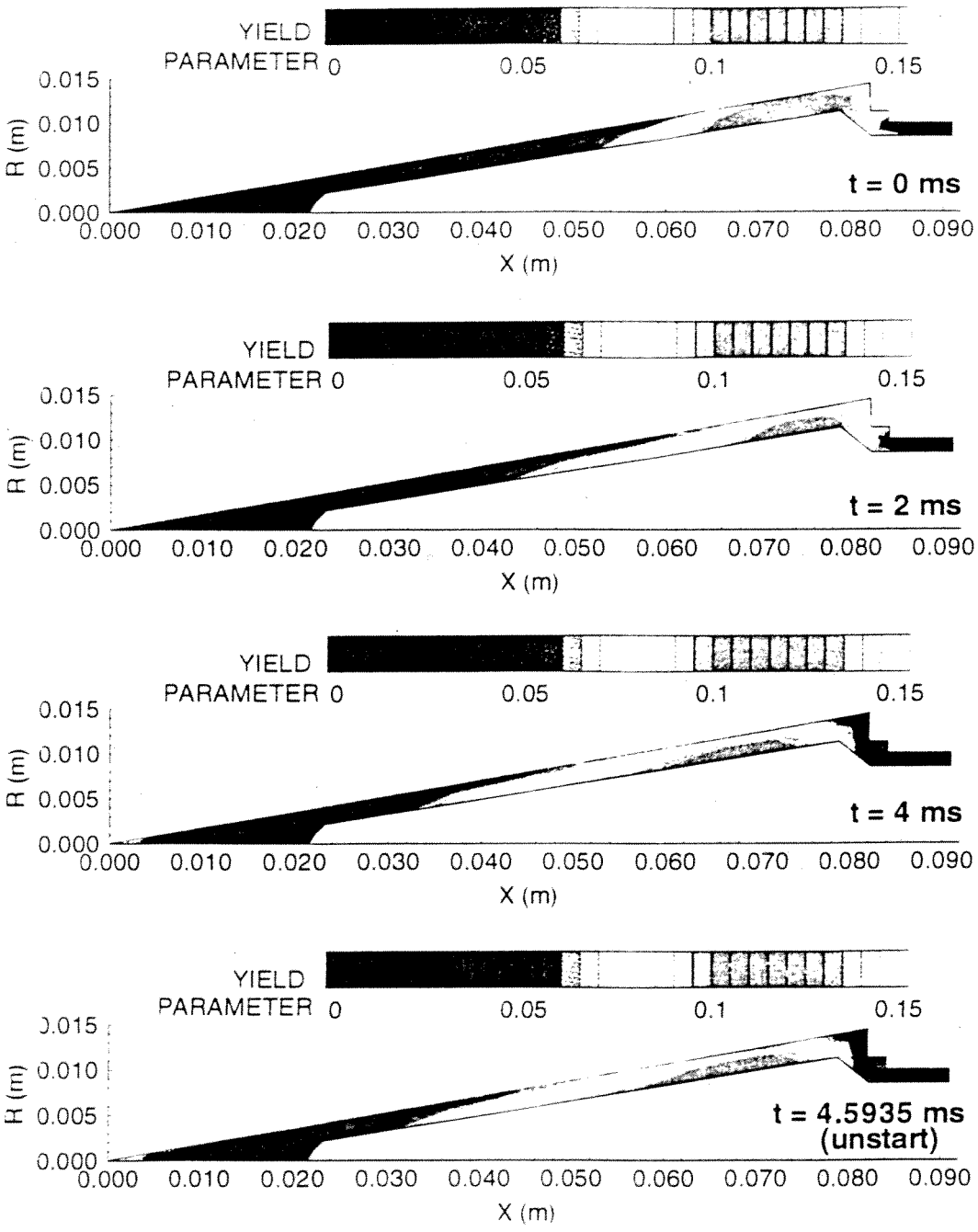

Figure 29. Yield parameter distribution in nose of projectile in simulation of HS 1062 (Al nose, Al body) from start to unstart.

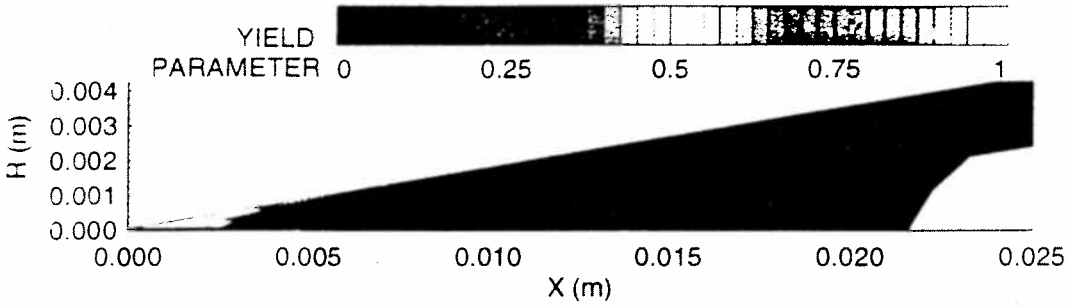

Figure 30. Yield parameter distribution in tip of nose of projectile in simulation of HS 1062, at unstart.

to be melting). Thus, this simulation shows that the nose tip is likely to be damaged, probably by ablation.

The next computer simulation is of another experiment using a projectile with an aluminum alloy nose, HS 1064. Figure 31 shows the experimental velocity profile used in the simulation. The projectile in this experiment did not experience as high an acceleration as the projectile in HS 1062, and also did not attain as high a peak velocity; thus, the projectile experienced a somewhat longer heating time, but also at lower Mach numbers and lower temperatures.

Figure 32 shows the temperature contours for the computer simulation of HS 1064. The contours vary over the same temperature range as that of Fig. 24. Again, the shocks strengthen and are thus easier to discern as the projectile accelerates to higher Mach numbers. Here, however, the peak projectile velocity is less, so the conical shock angle at the end of the experiment is greater than at the end of HS 1062; consequently, the reflected shock impinges on the nose further upstream than for the earlier

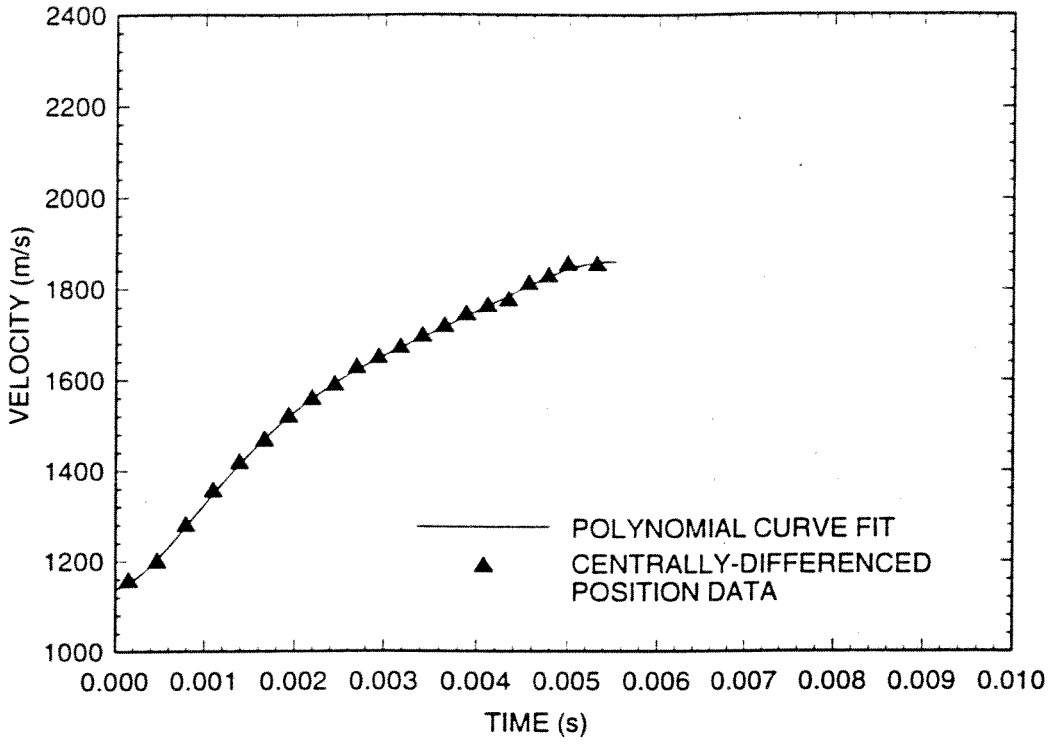

Figure 31. Experimental velocity history for HS 1064 (Al nose, Ti body).

experiment. One can also see the layer at the surface of the nose in which the temperature has risen, particularly around the tip. At the end of the experiment, just before the unstart, the heated layer has reached thicknesses of up to 1 mm. The tip has heated significantly to an axial length of 5 mm; although the Mach number, and thus the resulting shock temperature, is lower than in HS 1062, the duration of the heating is longer, resulting in a similar temperature distribution.

Figure 33 shows the temperature along the surface of the nose cone of the projectile in HS 1064. Figure 34 shows the corresponding normal heat flux flowing from the boundary layer into the surface. As in HS 1062, local peaks in heat flux and temperatures occur at two areas: at the nose tip and behind the reflected shock. Also, the

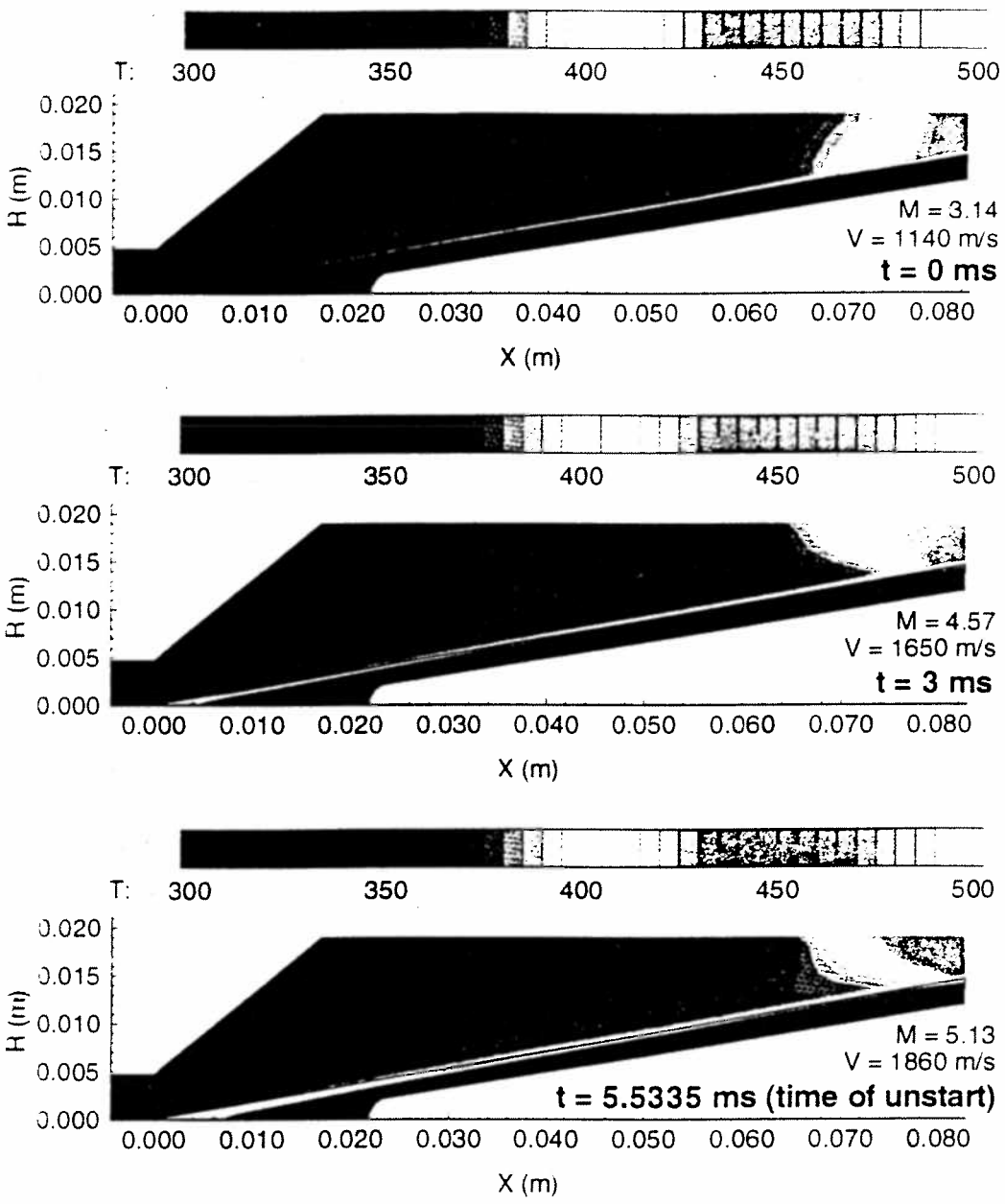

Figure 32. Temperature contours in gas flow and projectile nose in simulation of HS 1064 (Al nose, Ti body) from start to unstart.

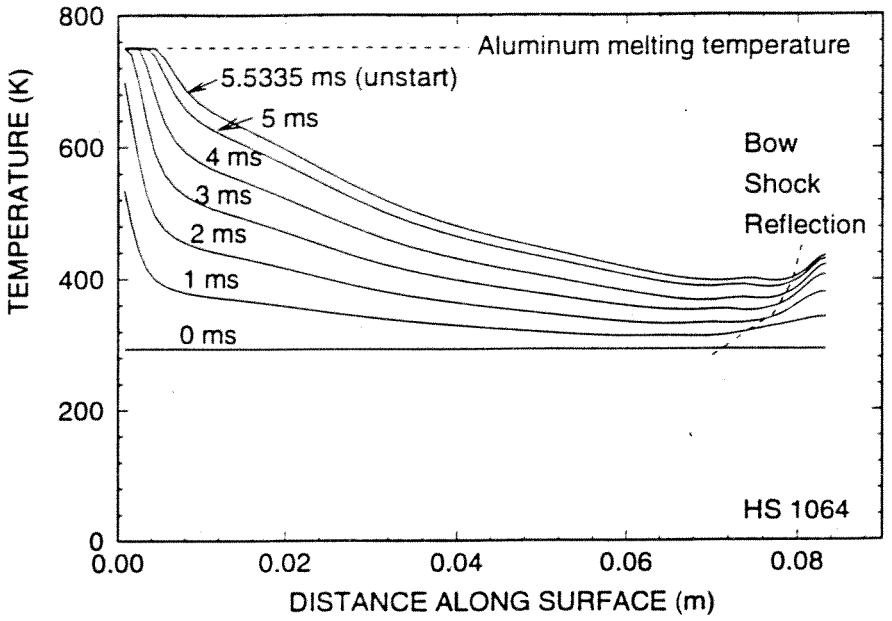

Figure 33. Surface temperature profiles of projectile nose in simulation of HS 1064 (Al nose, Ti body).

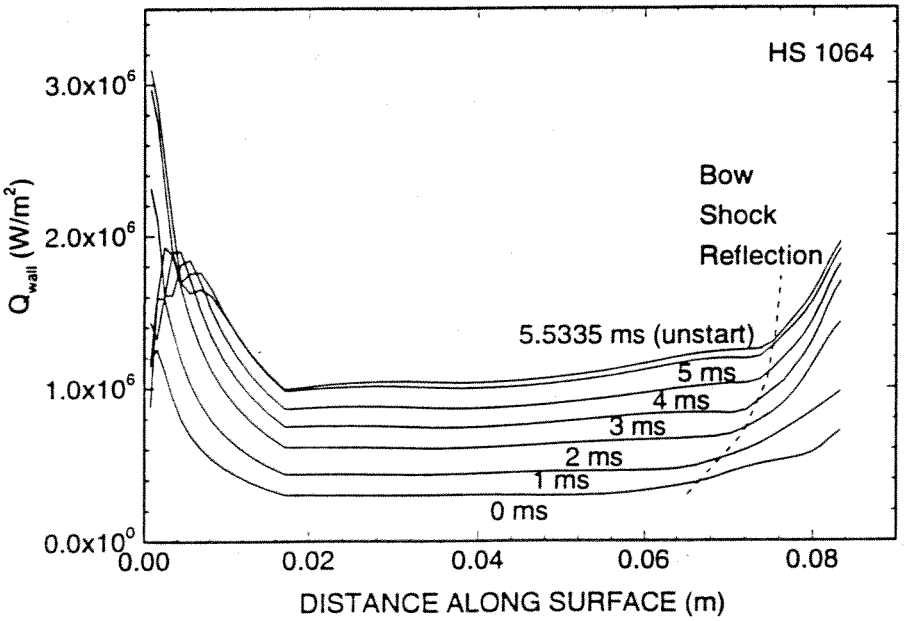

Figure 34. Variation of normal heat flux to surface of projectile nose in simulation of HS 1064 (Al nose, Ti body).

tip reaches the melting temperature by approximately three milliseconds after the start of the experiment, as in the case of HS 1062.

Figure 35 shows the yield parameter in the projectile nose over the course of the experiment. As in HS 1062, the yield parameter in the bulk of the hollow part of the projectile nose in HS 1064 never approaches failure, with the maximum yield parameter of approximately 0.15 occurring in an area in front of the throat. Here, the reflected shock impinges on the thin section of wall just in front of the end wall of the nose, and at the section of the nose with the largest diameter. The only visible part to fail in these conditions is the nose tip, shown in an expanded view in Fig. 36. Note that the surface has reached the melting point over the front 4 mm. Based on this analysis, the nose tip is also expected to have blunted.

Titanium Noses: HS 1063 & HS 1066

The next two series of figures show the results of computational simulations of experiments using titanium alloy noses. Figure 37 shows the velocity history of the projectile in HS 1063. Obviously, the experimental velocity data fluctuate greatly after about 4.5 milliseconds into the experiment, indicating that the thrust on the projectile was not steady. The reason for this irregularity in the thrust is unknown; however, the maximum velocity attained by the projectile in this experiment is higher than that of any of the other experiments in this series, so the fluctuations in thrust and velocity may be related to the high velocity of the projectile. The polynomial approximation should be considered suspect for times beyond five milliseconds, particularly at the end of the experiment. Nevertheless, the pictured velocity function is an adequate approximation for simulating this experiment, and is used here.

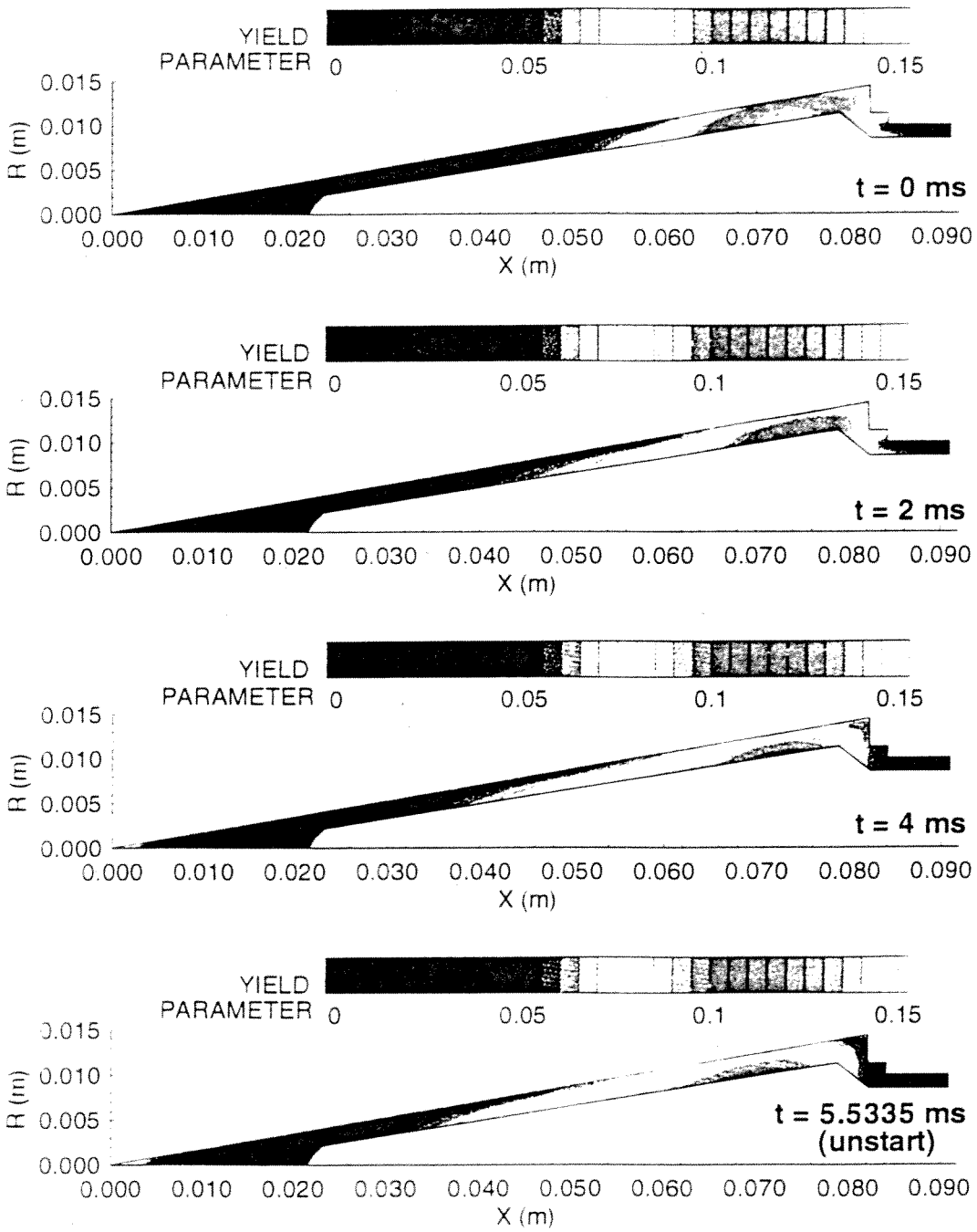

Figure 35. Yield parameter in projectile nose in simulation of HS 1064 (Al nose, Ti body) from start to unstart.

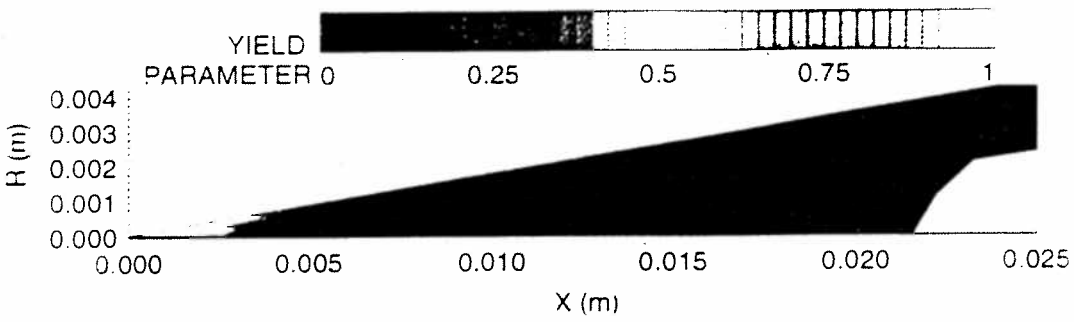

Figure 36. Yield parameter in tip of nose of projectile in simulation of HS 1064 (Al nose, Ti body) at time of unstart.

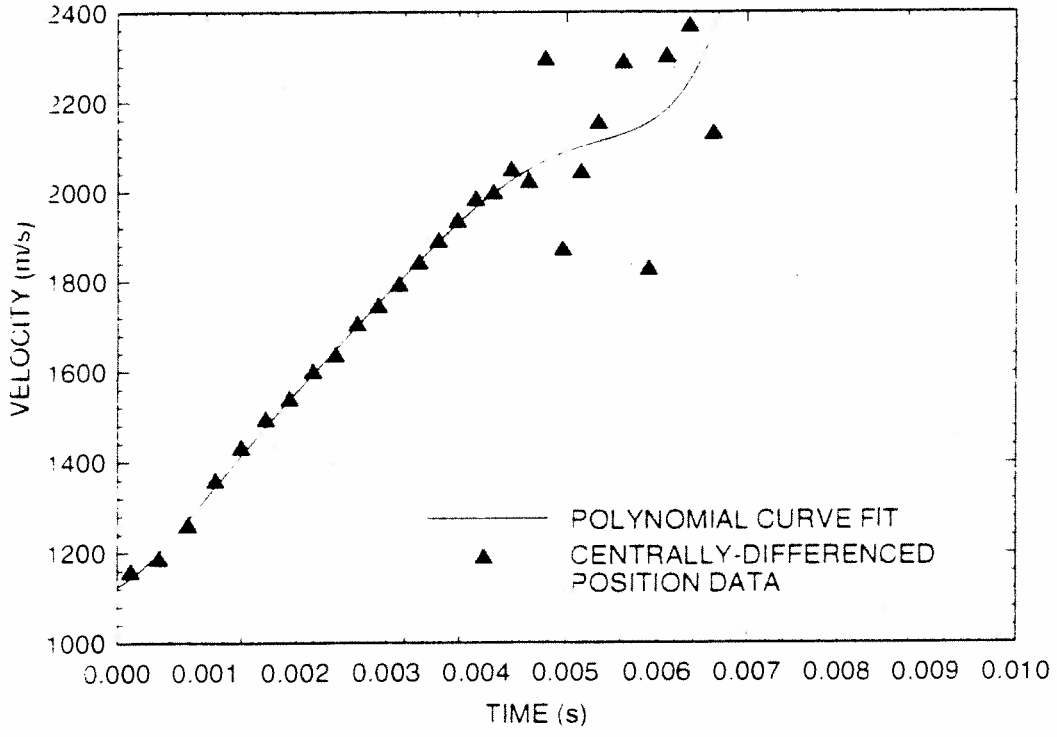

Figure 37. Velocity history of projectile in HS 1063.

Figure 38 shows the temperature contours in the flow and the projectile nose over the course of this experiment. As in the aluminum-nose experiments, the shock angles decrease as the projectile accelerates over time, and the contact point of the reflected shock on the nose moves back towards the throat. The temperature in the flow behind the shocks ranges from about 400 K to 500 K, with much higher temperatures found in a thin boundary layer next to the projectile surface, as shown in Figs 39 and 40. Unlike the aluminum noses, however, the titanium nose does not heat up appreciably beyond a rather thin depth; the computed temperatures of an aluminum and a titanium nose are compared in Figs. 41 and 42. This decrease in thickness of the heated layer can be largely attributed to the relatively low thermal diffusivity of the titanium alloy; however, a concomitant effect is that since heat is not conducted away readily, the temperature of the surface layer should rise much faster.

Indeed, this effect can be seen in Fig. 43, which shows the temperature at the surface of the nose. (Note that the ordinate of this plot covers a wider range in temperatures than in Figs. 27 or 33.) The temperature at the tip reaches the melting temperature of aluminum (about 750 K) after only two milliseconds, and continues to rise rapidly beyond that time. However, at no time during the experiment does the surface temperature reach the melting point of the titanium alloy. As in the aluminum nose experiments, local peaks in temperature occur at the tip and behind the reflected shock; however, although the temperature rise is higher everywhere on the nose surface, the reflected shock creates a far less significant temperature rise (relative to the rest of the temperature profile) than in the aluminum nose experiments.

Figure 44 shows the corresponding normal heat flux to the surface. Note that the computer simulation indicates a negative heat flux at the nose tip; the gas appears to

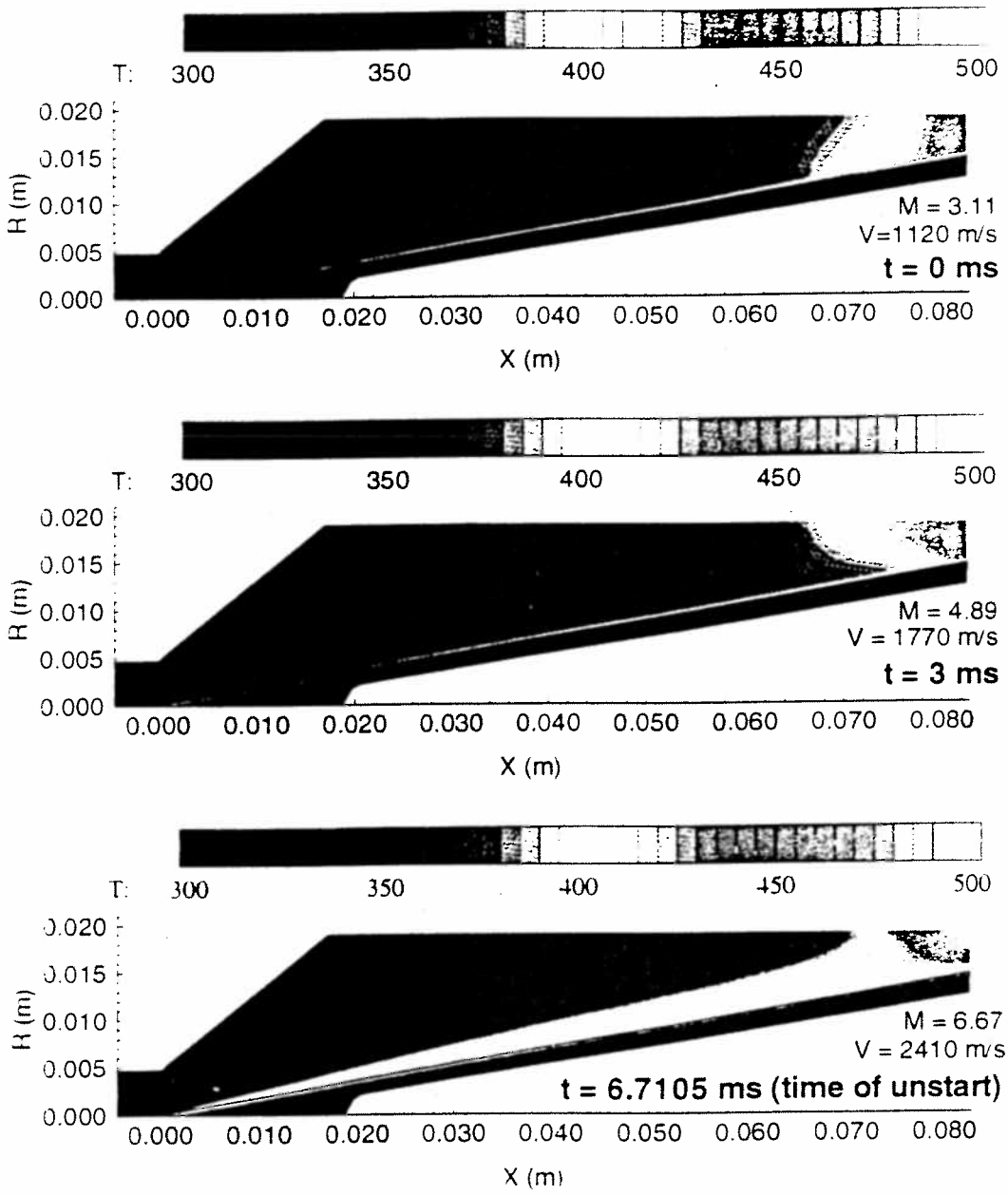

Figure 38. Temperature contours in gas flow and nose of projectile in simulation of HS 1063 (Ti nose, Al body) from start to unstart.

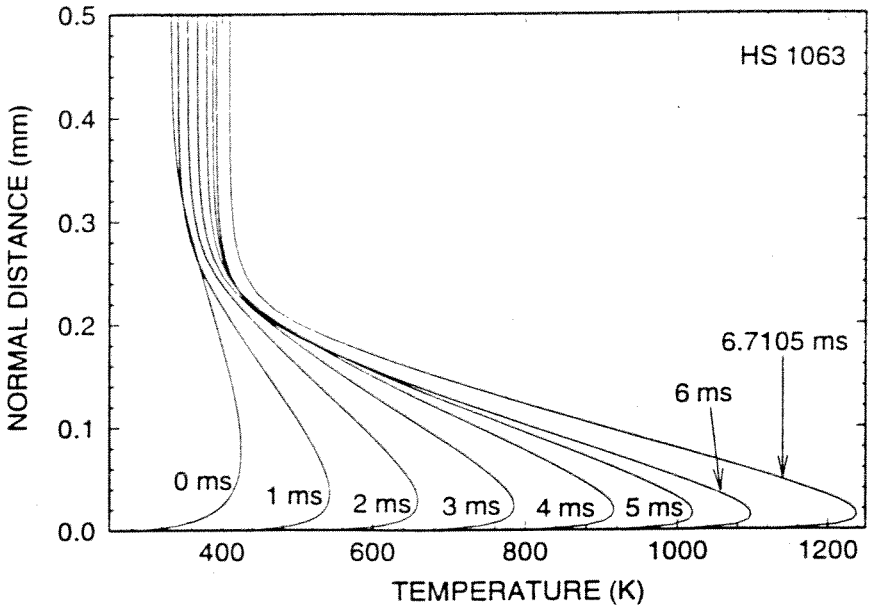

Figure 39. Temperature in boundary layer, 3 mm from nose tip, in simulation of HS1063 (Ti nose, Al body).

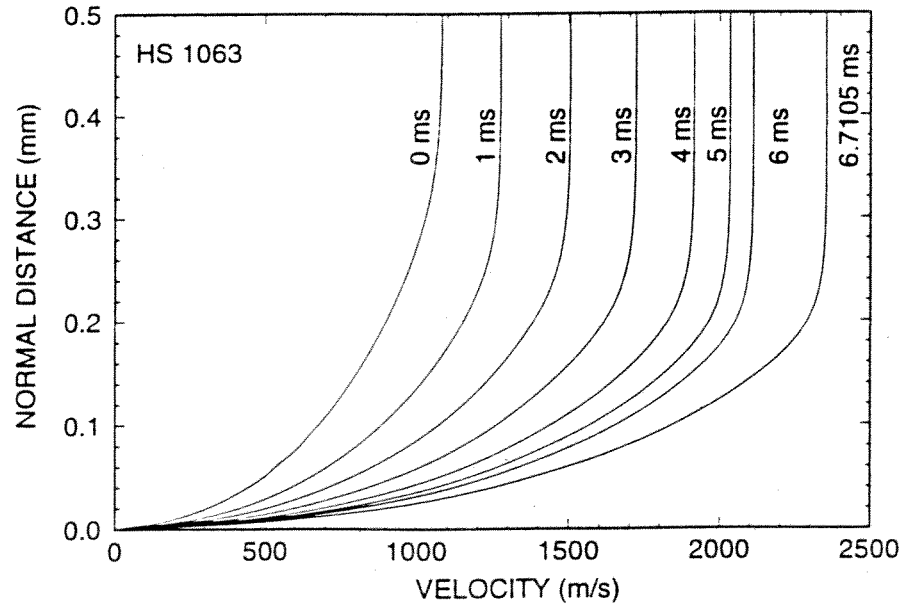

Figure 40. Velocity in boundary layer, 3 mm from nose tip, in simulation of HS1063 (Ti nose, Al body).

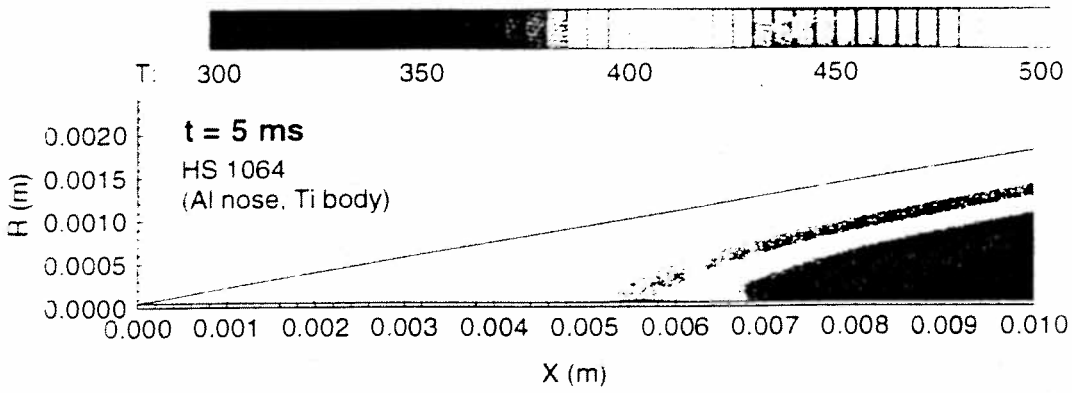

Figure 41. Temperature distribution at tip of Al nose in HS 1064.

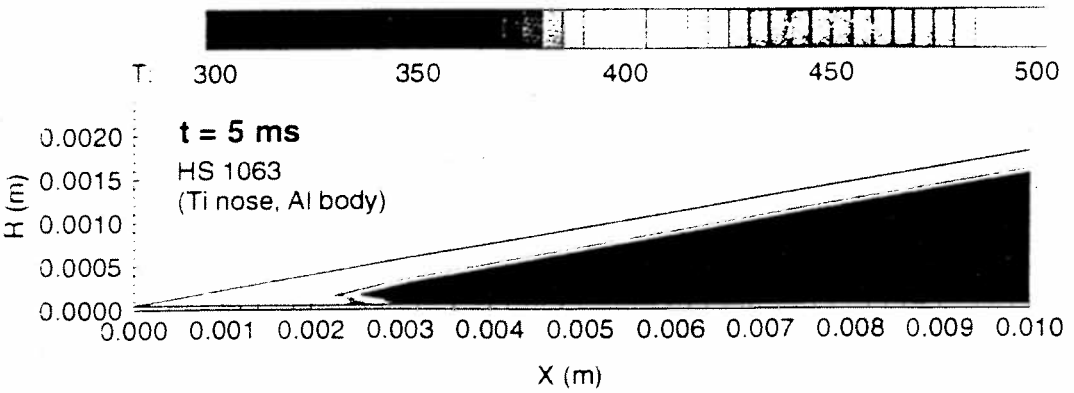

Figure 42. Temperature distribution at tip of Ti nose in HS 1063.

conduct heat away from the nose tip, contradicting the increase in temperature over time. However, the contradiction results from the limitation in the minimum grid spacing and the method of calculating the conductive heat flux at the wall, as shown in Fig. 45. Far from the tip, the temperature boundary layer is significantly thicker than the grid spacing, and the second-order calculation of the temperature gradient results in a good approximation of the heat flux at the surface. Near the tip, however, the boundary layer is thinner than the grid spacing, and the second-order calculation of the

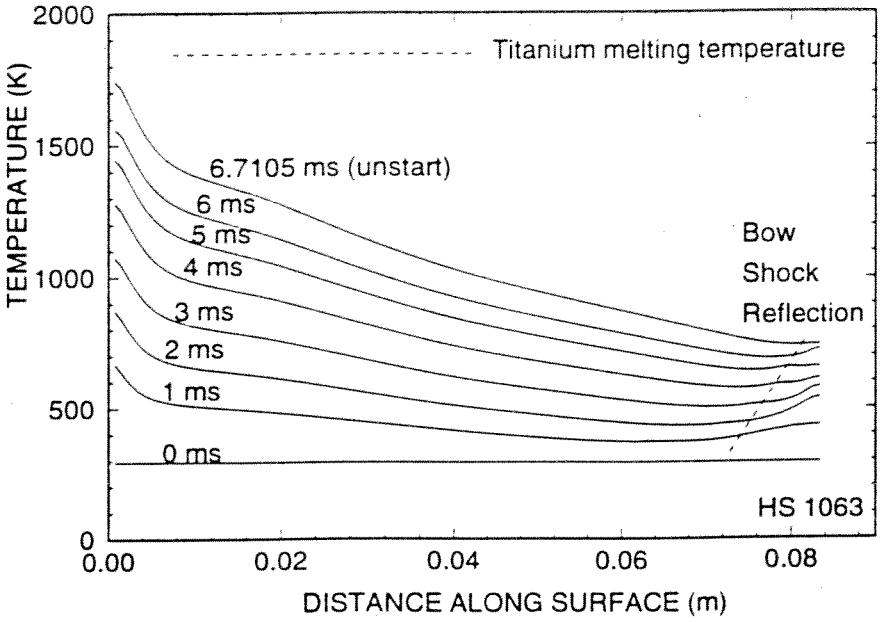

Figure 43. Temperature along surface of projectile nose in simulation of HS 1063 (Ti nose, Al body).

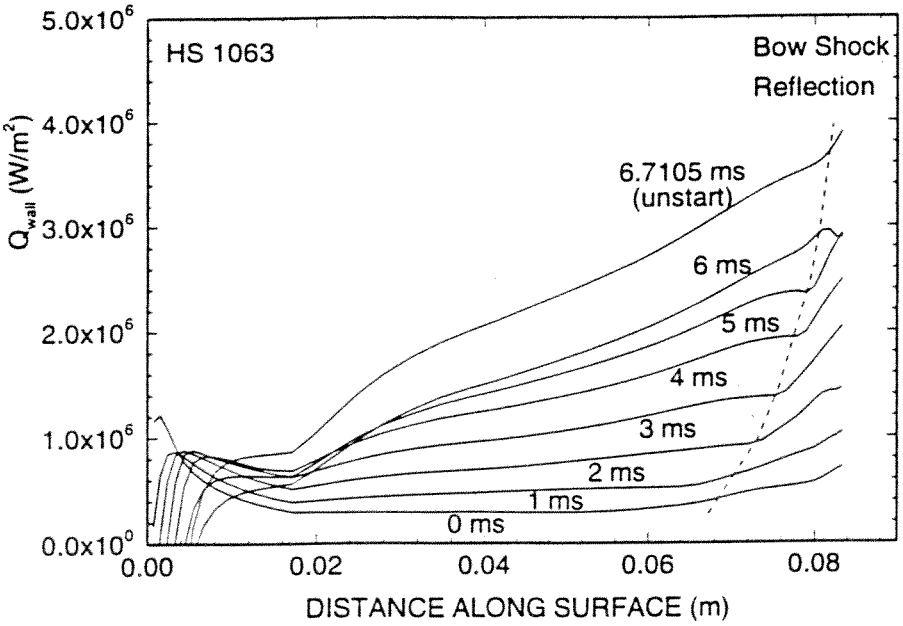

Figure 44. Variation of normal heat flux to surface of projectile nose in simulation of HS 1063 (Ti nose, Al body).

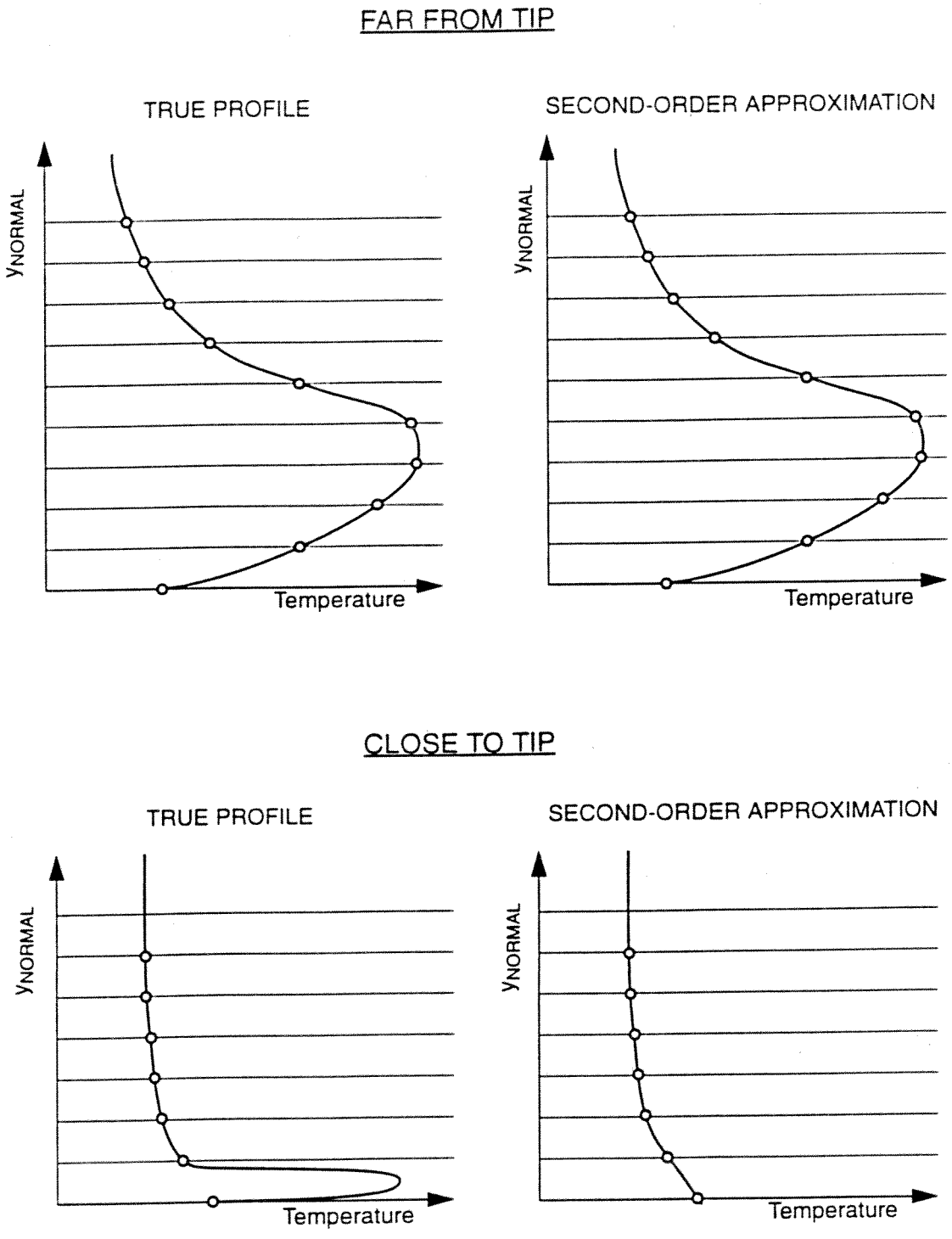

Figure 45. Schematic of boundary layer far from tip and close to tip.

temperature gradient results in the incorrect sign and magnitude of the heat flux. Fortunately, the interface condition is solved using a finite-volume method, which does not directly involve the calculated heat flux at the surface. As discussed in Ch. 5, the fluxes normal to the interface are calculated on cell boundaries located away from the interface itself. The gradients do not vary so much on these boundaries, so the calculated temperature gradient is more accurate than at the interface. Also, on the cell boundaries on the gas side, the energy flux includes both conduction and viscous dissipation terms, so that the precision in the calculation of the conductive flux is not as critical as it would be on the interface itself. Finally, using a finite-volume form of the Navier-Stokes equations always maintains energy conservation, so although the temperature profile in the boundary layer may be too thin to resolve, the calculated temperature at the surface should be correct.

Contours of the yield parameter for the titanium nose are shown in Fig. 46. The yield parameter levels are even lower than those seen in the aluminum noses, never exceeding a level of 0.075. If only aerodynamic stresses are considered, the nose structure is probably overdesigned--that is, the walls of the hollow titanium nose is thicker than absolutely necessary, and, given the undesirably high mass of a titanium nose and the accompanying penalty in acceleration (for a given gas fill pressure), noses with thinner walls should be used. Also notable is the fact that the maximum yield parameter in the nose tip remains below unity, as shown in Fig. 47; that is, the tip is predicted to not erode in this simulation.

The velocity history for the next titanium nose experiment, HS 1066, is shown in Fig. 48. Note that the velocity data show a much smoother acceleration than the data of HS 1063; hence, the polynomial approximation used here models the velocity more

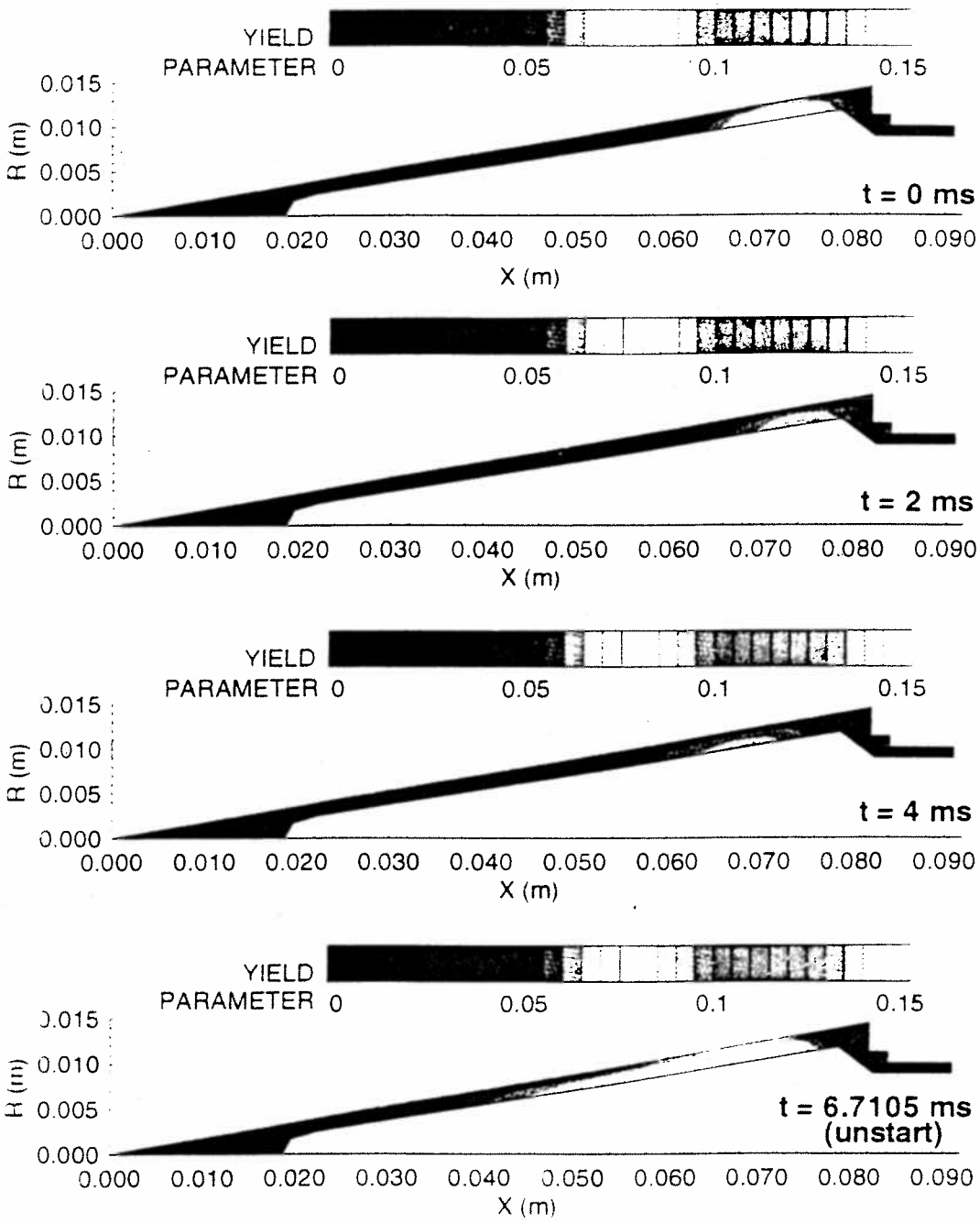

Figure 46. Yield parameter contours in projectile nose in simulation of HS 1063 (Ti nose, Al body) from start to unstart.

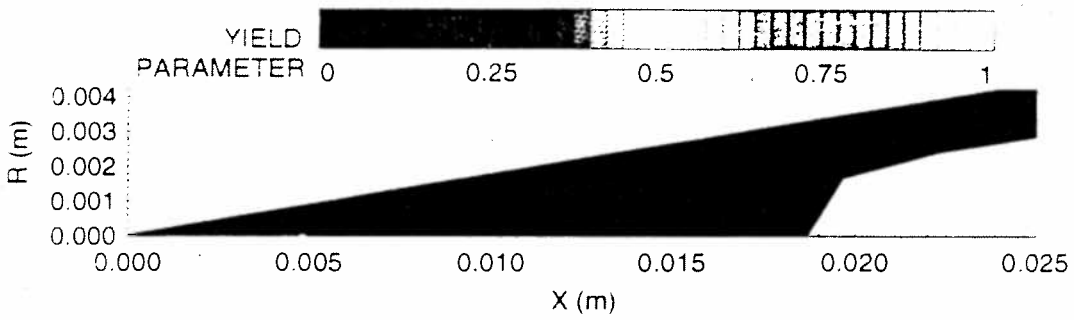

Figure 47. Yield parameter in tip of nose of projectile in simulation of HS 1063 (Ti nose, Al body) at time of unstart.

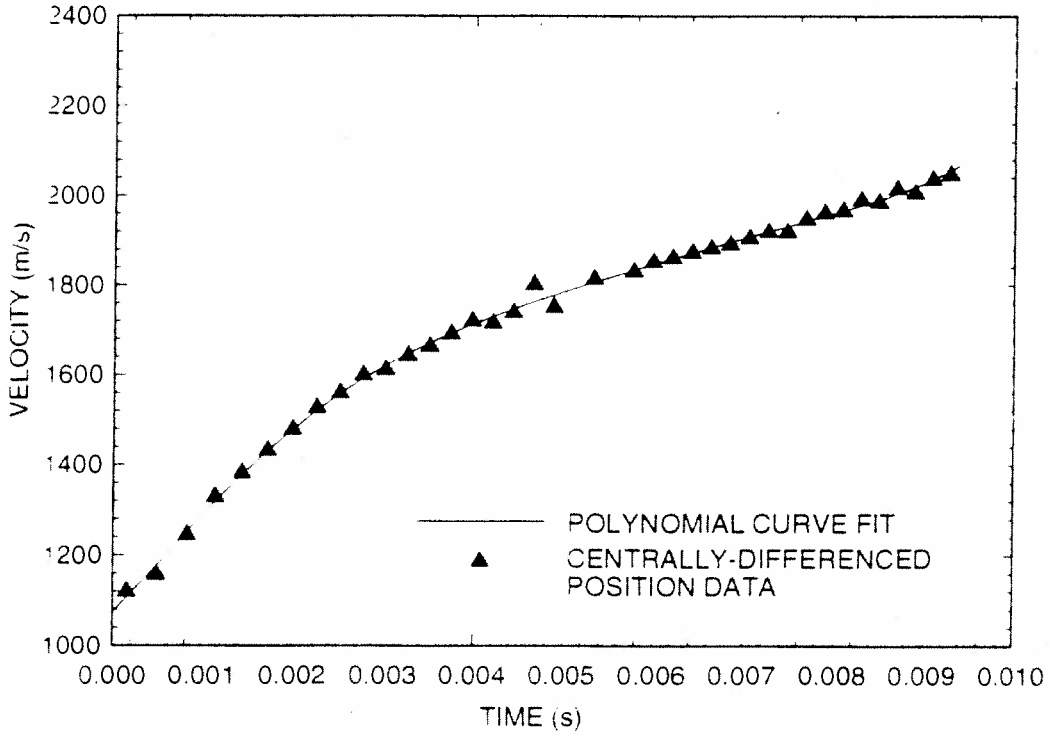

Figure 48. Velocity history of projectile in experiment HS 1066 (Ti nose, Ti body).

accurately. The projectile in this experiment experienced the longest time of heating, as well as attaining a high maximum velocity; thus, the projectile in this experiment is subjected to the most severe possible conditions for aerodynamic heating.

Figure 49 shows the temperature contours over the duration of HS 1066. Again, the conical shock and its reflections can be seen, with the temperature in the main flow rising to about 450 K at the throat (at the far right of each plot), and to much higher temperatures in a thin boundary layer at the surface of the projectile. As in the previous titanium nose simulation, the high temperature does not conduct very far into the solid alloy, remaining instead in a thin layer near the surface.

Figures 50 and 51 show the surface temperature and heat flux from the gas to the surface of the nose, respectively. The temperature at the nose tip never reaches the melting point of titanium; however, after only two milliseconds, the temperature is hot enough to melt aluminum, and continues to rise rapidly after that point. In this case, with a much smoother velocity history (in particular, one that does not dramatically increase at the end of the simulation), the attained temperature is much lower than that of HS 1063, even with the significantly longer exposure to the hot boundary layer. Again, the calculated heat flux to the nose tip is negative for much of the experiment, indicating that the radial grid spacing at the tip is too coarse to calculate the surface heat flux. Fortunately, as previously explained, the interface temperature is calculated using energy fluxes located a small distance away from the surface, so the correct surface temperature is calculated.

Figure 52 shows the contours of the yield parameter in the projectile nose of HS 1066. As in the simulation of HS 1063, the yield parameter in most of the nose never exceeds a level of 0.05, except for the area immediately in front of the throat

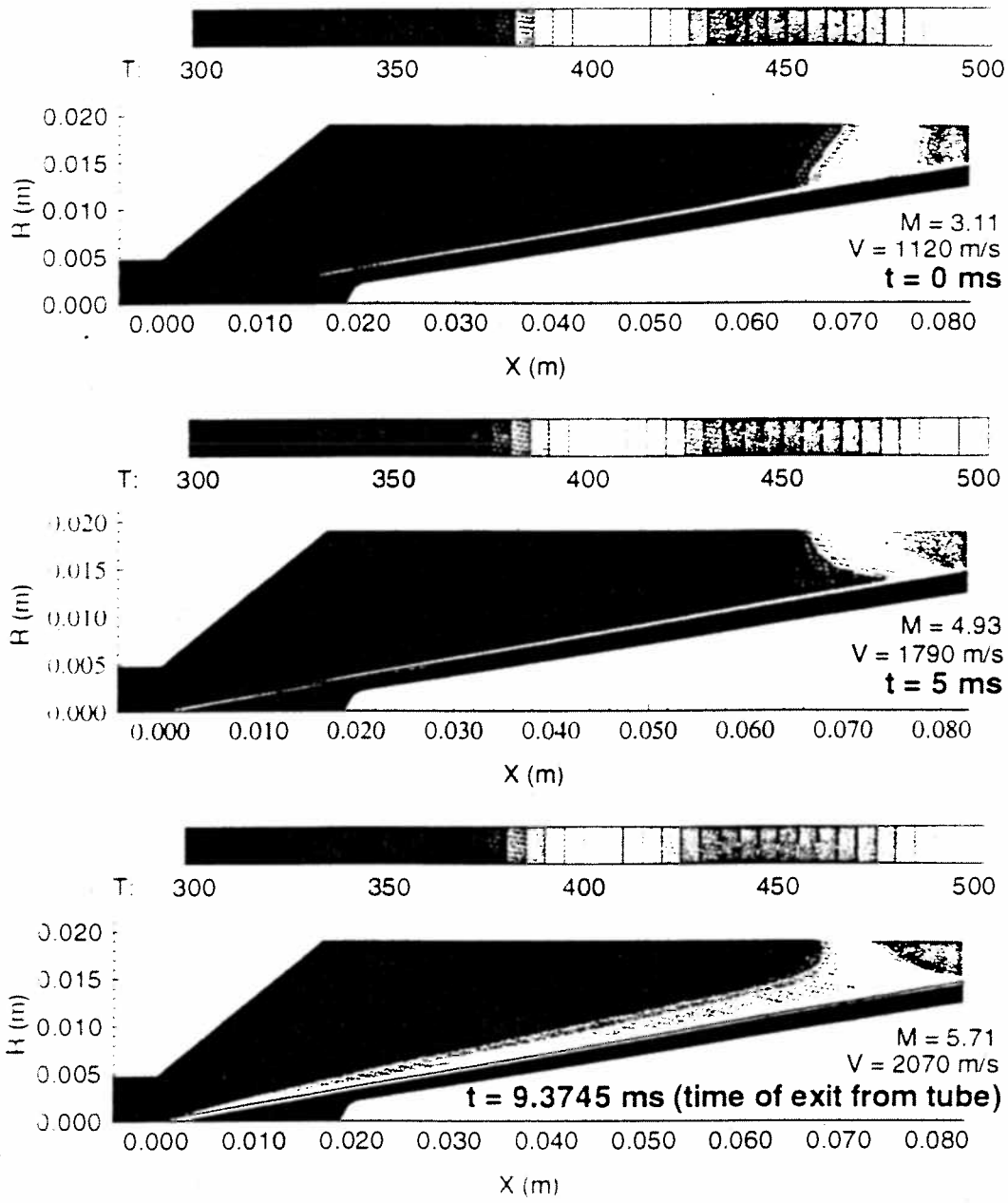

Figure 49. Temperature contours in gas and projectile nose in simulation of HS 1066 (Ti nose, Ti body) from start to end of experiment (drove out tube).

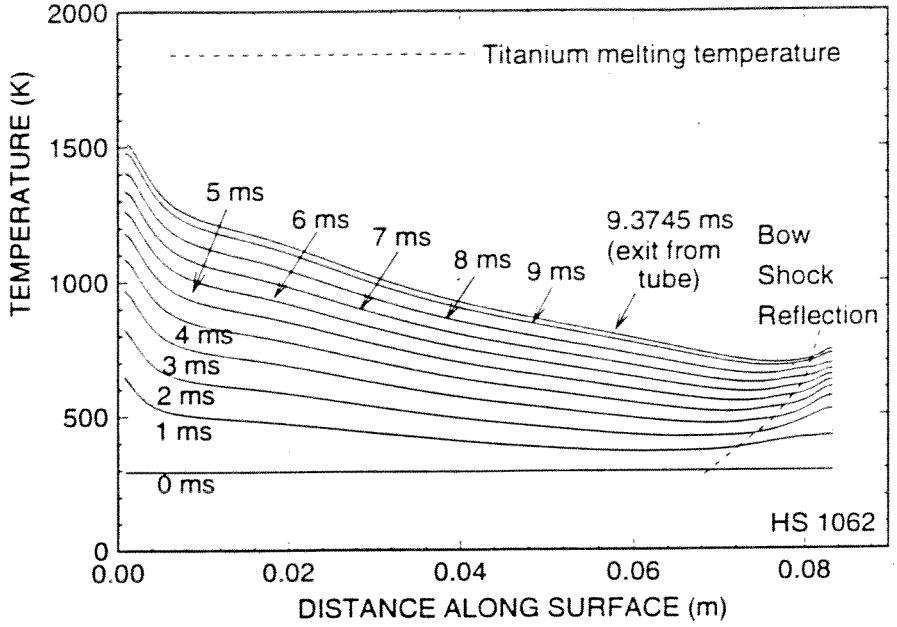

Figure 50. Temperature along surface of projectile nose in simulation of HS 1066 (Ti nose, Ti body).

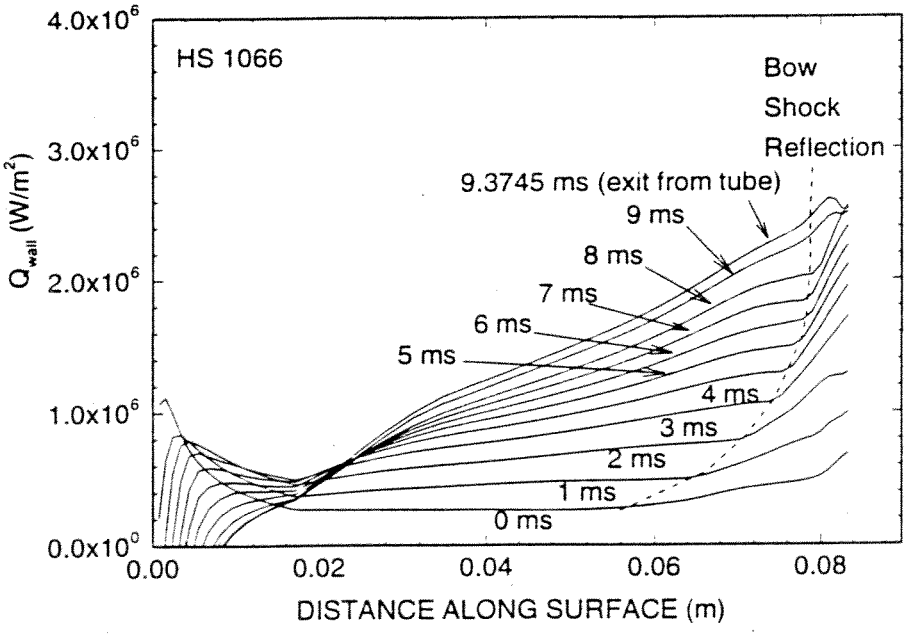

Figure 51. Variation of normal heat flux to surface of projectile nose in simulation of HS 1066 (Ti nose, Ti body).

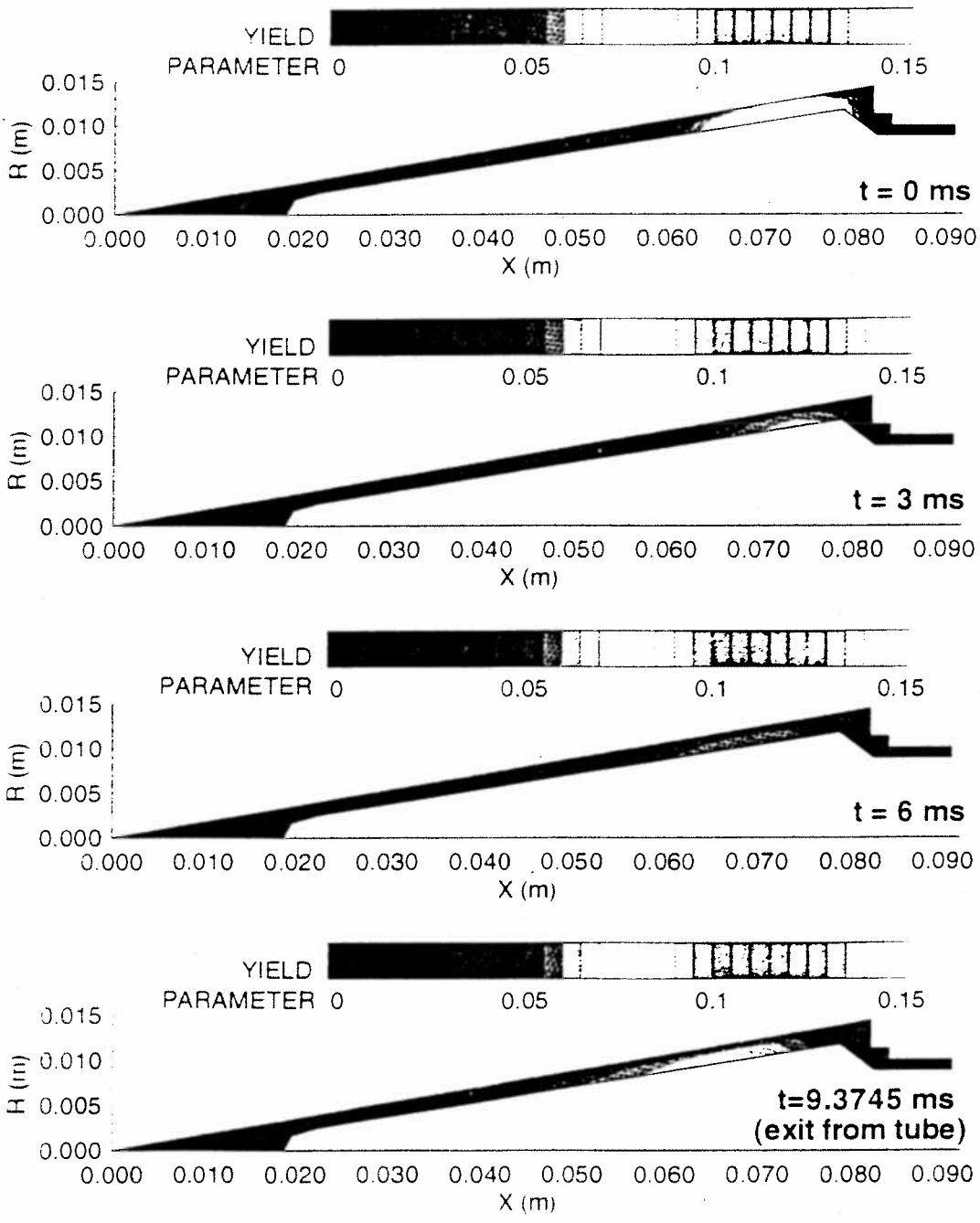

Figure 52. Yield parameter contours in projectile nose in simulation of HS 1066 (Ti nose, Ti body).

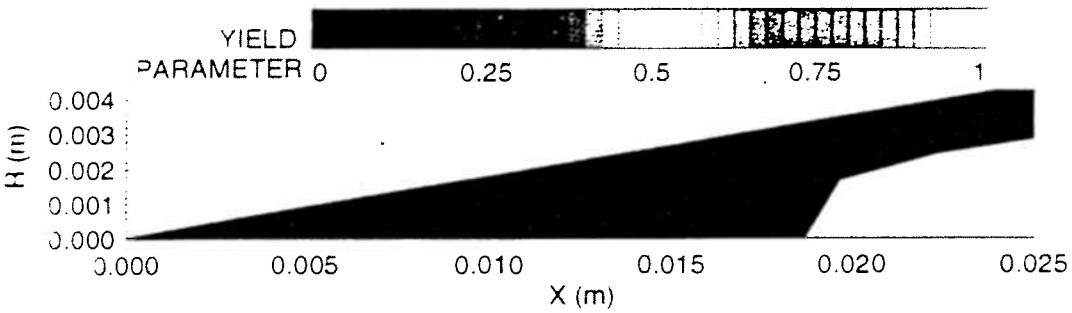

Figure 53. Yield parameter contours at tip of nose of projectile in simulation of HS 1066 (Ti nose, Ti body) at time of exit from ram accelerator tube.

where the reflected shock impinges on the projectile), which peaks at about 0.075. Figure 53 shows an expanded view of contours of the yield parameter at the nose tip as the projectile reaches the end of the ram accelerator. Again as in the other titanium nose simulation, the nose tip shows no sign of approaching a state of plastic yield; the temperature is well below the melting point, and the external pressure produces no stress that even approaches yielding. Thus, in neither titanium nose case should the tip erode from aerodynamic heating and stresses. Of course, as in the aluminum nose simulations, the effects of projectile canting, balloting, and passage through the Mylar diaphragms sealing each stage are not included in this analysis; some damage to the nose from these events may occur.

7.3 Additional simulations

Unfortunately, due to limitations in resources, other experiments to study projectile nose heating could not be performed in the laboratory. However, such experiments can be simulated on a computer. These simulations are used to parametrically study the effects of using other materials and geometric configurations;

the effects of variations in other parameters were minimized by using the experimental conditions and velocity histories of past experiments.

Blunt Noses

Since the computer simulations indicate that aluminum noses yield at the nose tip, blunting is highly likely. As shown in Chapter 1, a sharp nose blunts quickly at first; as the radius increases, the local heat flux on the tip should decrease, reducing the rate of blunting. The heat flux is closely coupled to the shape of the nose tip and the resulting flow around it. Obviously, then, the heat flux to the nose tip varies over time in a highly complex manner. The next two simulations investigate the heating of blunt nose tips.

To this point, the heating pattern of the nose tip has only been simulated with the assumption of a sharp nose tip; obviously, this assumption only holds at the very beginning of an experiment. As an experiment progresses, the tip is expected to blunt, either from aerodynamic stresses or from passage through the Mylar diaphragms which seal each gas stage in the ram accelerator. The modeling of the recession of the alloy surface as it melts is beyond the scope of this analysis, thus only constant-radius nose tip geometries will be used.

The first simulation involves a nose tip with a 1 mm radius. Since the mass of such a nose would be similar to that of a sharp aluminum nose, the velocity history of HS 1062 was used in the simulation. The computational mesh is shown in Fig. 54. Note that here, unlike the sharp-nose meshes, the mesh curves around the nose tip; this shape is intended to improve the resolution of the flow around the tip, as well as minimizing any effect of the computational boundary conditions at the corner of the mesh on the stagnation point.

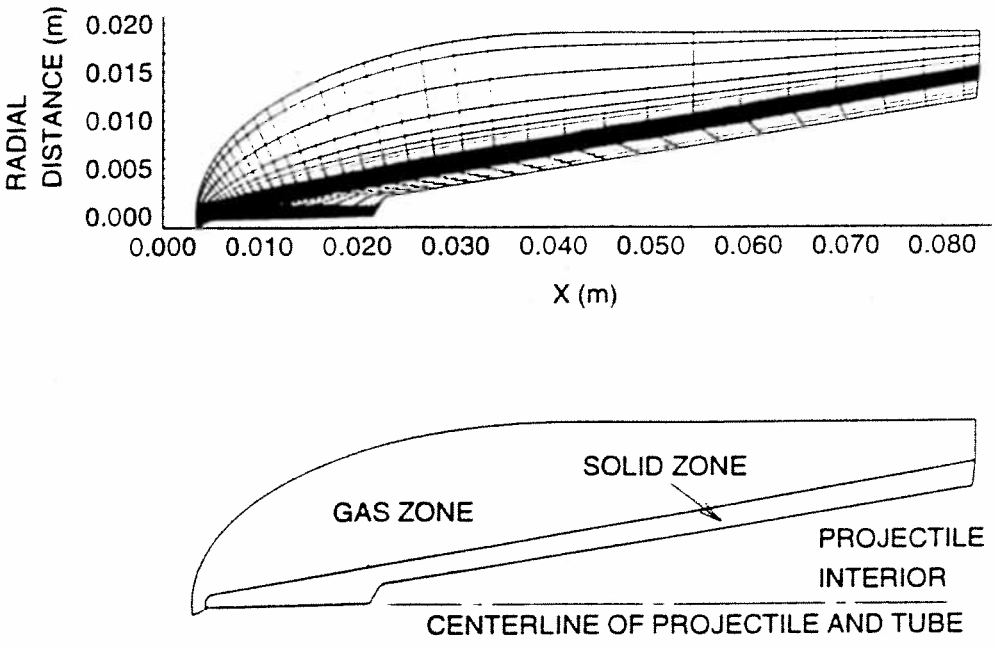

Figure 54. Computational mesh for one-millimeter radius nose.

Figure 55 shows the temperature contours in the gas and solid zones for this projectile nose. Compared with the temperatures seen in the corresponding sharp-nose simulation (Fig. 24), one can see a larger heated region in the gas behind the bow shock, along with an "entropy layer" along the nose surface which is thicker than the boundary layer of the sharp nose. Although blunting of leading surfaces is often used to reduce heat transfer, this blunted nose still experiences significant heating, as can be seen by the hot nose tip in Fig. 55.

The surface temperature on the nose is shown in Fig. 56, and can be compared with the similar plot, Fig. 27, for the sharp nose. As expected, the temperature on the

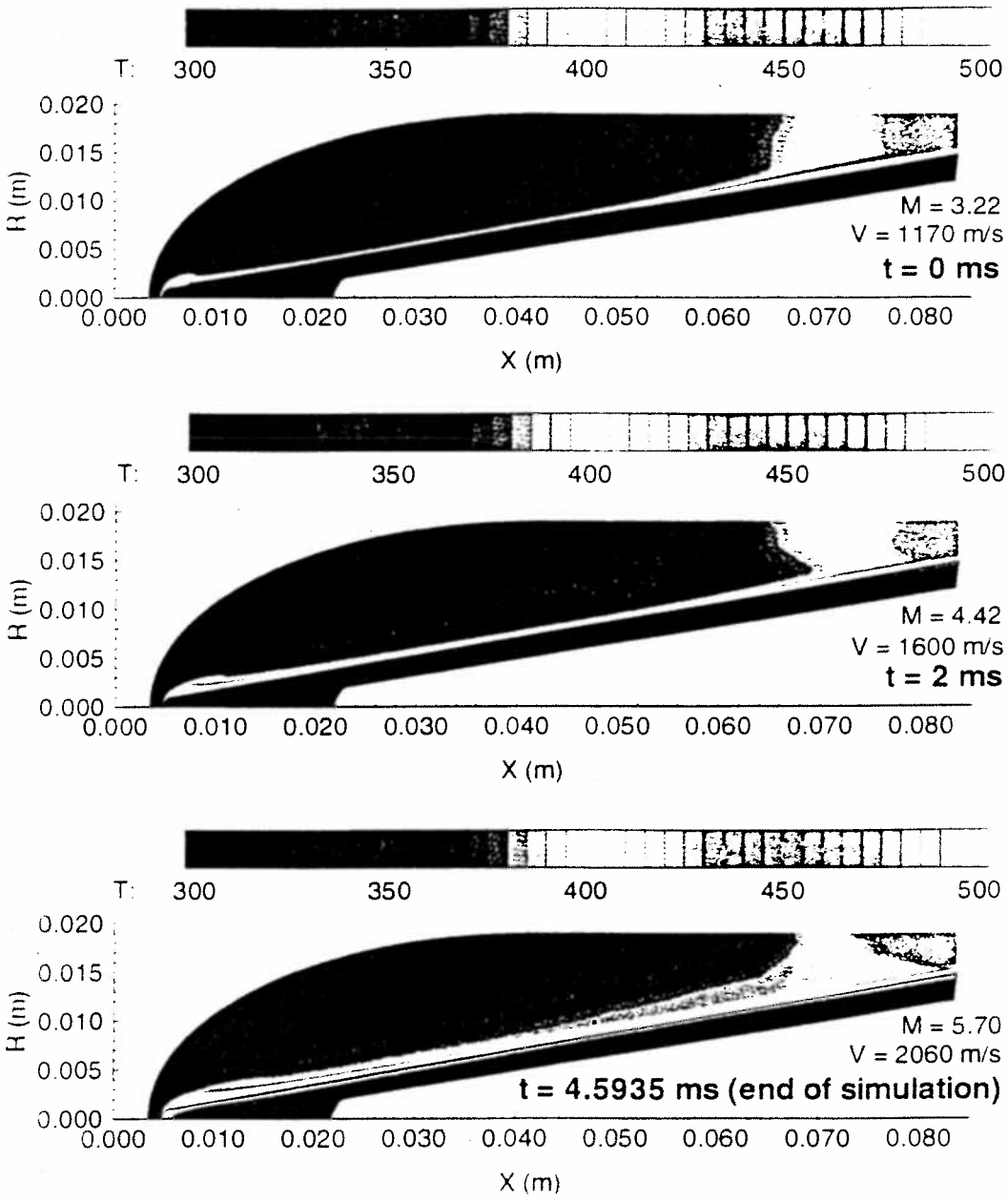

Figure 55. Temperature contours in gas and solid zones in simulation of projectile with a 1 mm radius nose tip, from start to 4.5935 ms.

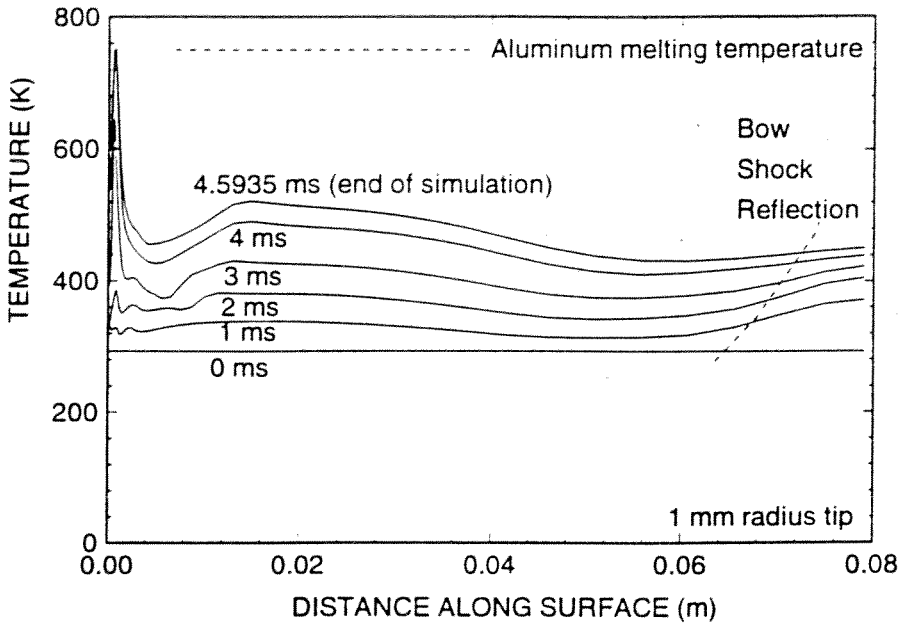

Figure 56. Surface temperature profiles of projectile nose with a 1 mm radius tip.

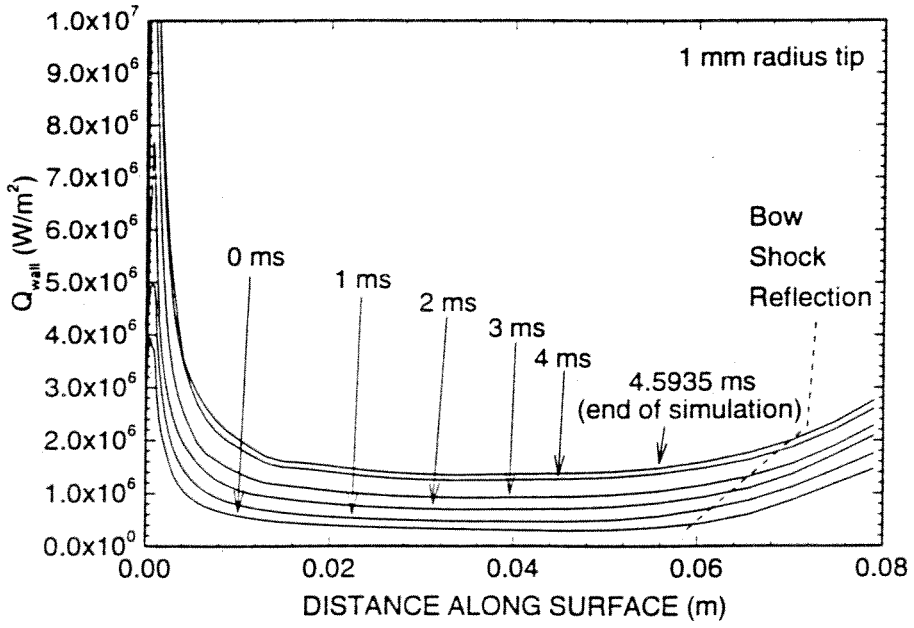

Figure 57. Variation of normal heat flux to surface of projectile nose with a tip radius of 1 mm.

surface of the blunted nose rises more slowly than in the case of the sharp nose; indeed, only the very tip of the nose even approaches the melting temperature of the alloy.

Figure 57 shows the heat flux in the gas normal to the surface of the rounded nose (compare to the corresponding plot for the sharp nose in Fig. 28). The conductive heat flux at the surface is higher than for the sharp nose at the end of the simulation, largely because the temperature at the surface of the blunt nose is less, resulting in higher gradients in temperature between the hot entropy layer and the relatively cool alloy. Although the heat flux is lower at the tip of a sharp nose, there is very little alloy at the tip to absorb the heat, leading to a greater rise in temperature for sharp nose tips than for blunt ones. Therefore, the blunting of the nose leads to a lower overall temperature increase in the nose.

The calculated yield parameter in the nose is illustrated in Fig. 58. As in the simulation of the sharp nose, the hollow section of the nose approaches the yield point most closely in the region just ahead of the throat, peaking below a yield parameter level of 0.1 at the very start of the simulation, and declining as the reflected shock moves toward the thicker section at the rear of the nose. As with the sharp nose, this nose is thus not expected to fail here, assuming no canting or balloting of the projectile in the tube, and ignoring the stresses of passage through Mylar diaphragms and the acceleration of the projectile.

Note that, even though the temperatures in the solid tip are generally lower than in the sharp nose simulation, the yield parameter in the tip still reaches a quite high level. An expanded view of the yield parameter contours in the tip of this nose is shown in Fig. 59. Obviously, the tip meets the yielding criterion, so a nose of this configuration is predicted to erode. Thus, a blunt nose is susceptible to further erosion, and blunting of

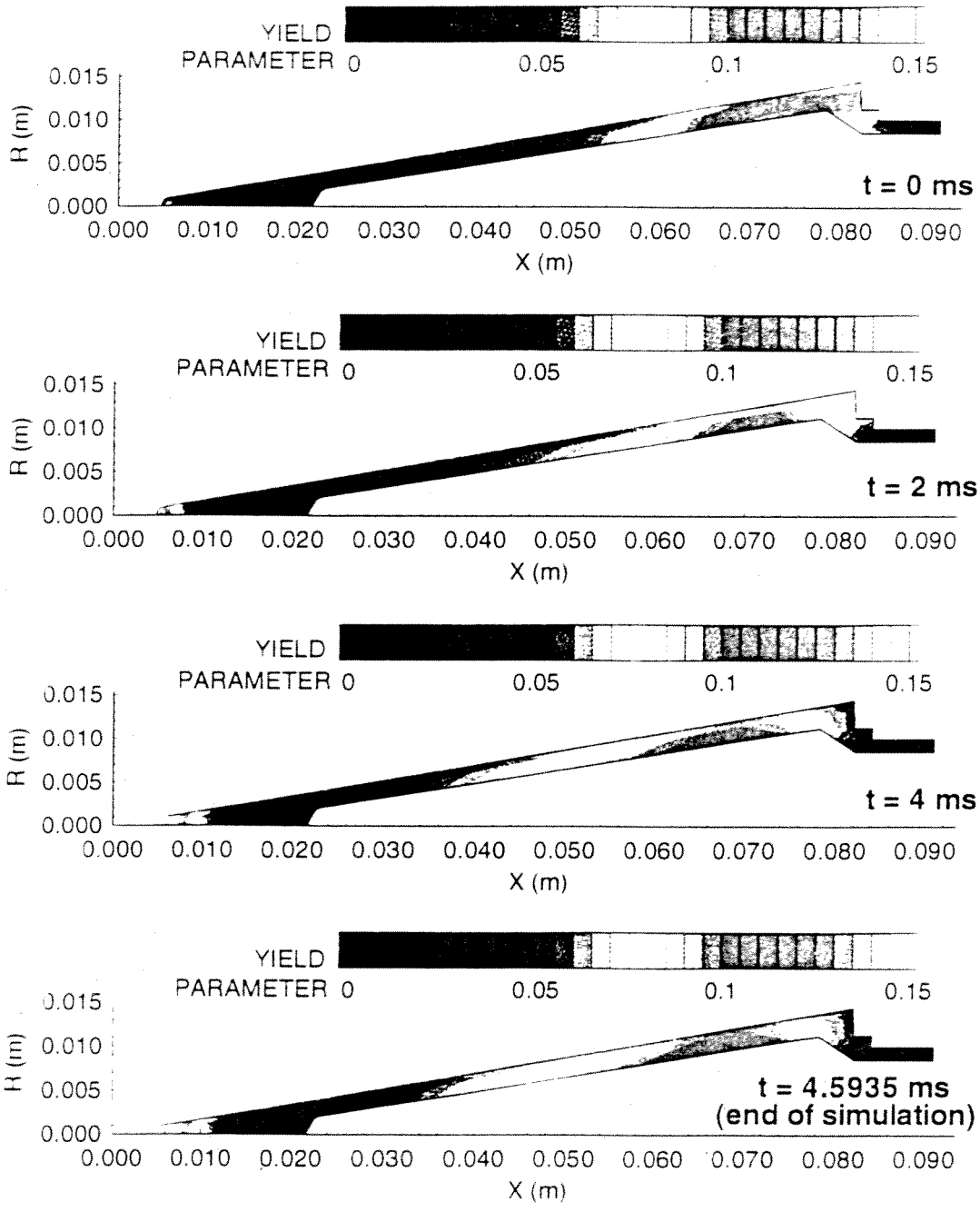

Figure 58. Yield parameter contours in projectile nose with a tip radius of 1 mm, from start to 4.5935 ms.

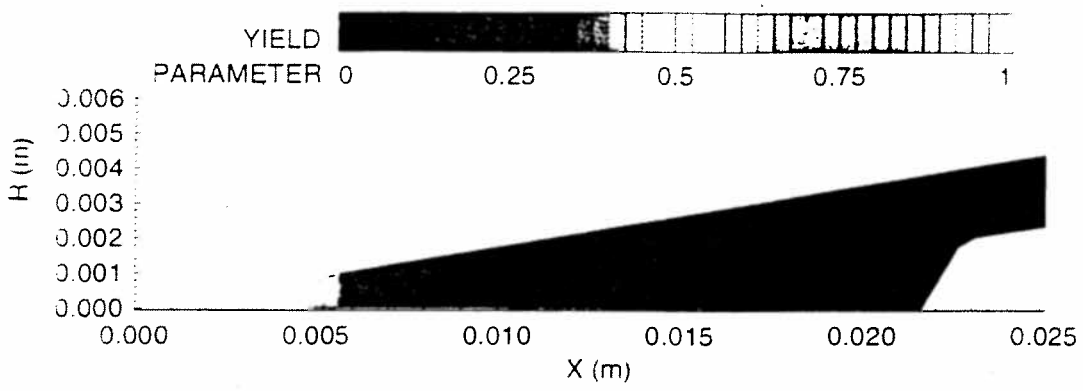

Figure 59. Yield parameter contours in projectile nose tip with a radius of 1 mm at end of simulation.

the nose prior to operation (intended to protect the tip against aerodynamic heating) would not be completely effective at this radius.

The next series of figures shows the results of a simulation of a projectile with a much blunter nose tip, with a radius of 2.5 mm. The computational mesh is shown in Fig. 60; the origin of the coordinate system is chosen to keep the position of the projectile throat at a constant coordinate. Again, the mesh curves around the centerline axis in order to more accurately resolve the conditions at the front stagnation point. Also, since the projectile configuration, except for the blunt nose, is the same as that of HS 1062, the velocity history of that experiment was used in this simulation as an approximation.

The resulting temperature contours are shown in Fig. 61. In these plots, the origin of the coordinate system is the point where the sharp nose tip would be. The most

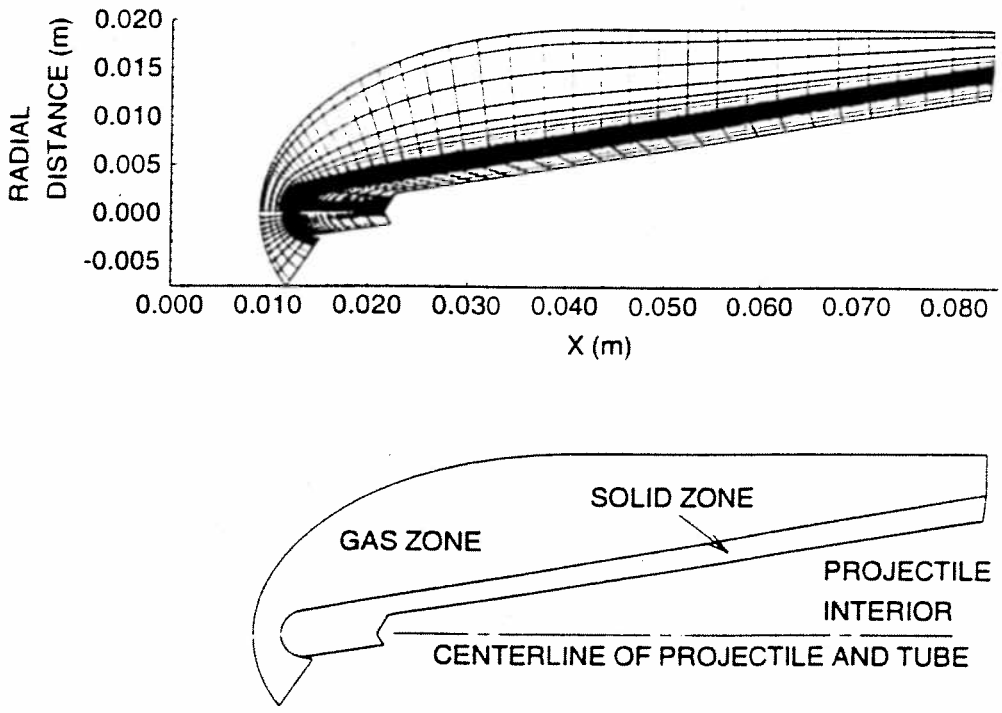

Figure 60. Computational mesh for nose tip with a radius of 2.5 mm.

noticeable feature in these figures is the bow shock and entropy layer, the hot region in the gas next to the projectile nose surface. This layer is roughly as hot as the boundary layer of the sharp-nose projectile, but is much larger in thickness. Although the greater thickness tends to reduce the gradients in temperature and velocity (and hence the heat flux to the solid surface), the blunt nose tip still experiences significant heating, on the order of hundreds of degrees. The presence of the bow shock and entropy layer produces large variations in temperature in the gas flow, which somewhat overshadow the smaller variations in temperature due to the "conical" shock. However, even though the shock angle is very high near the stagnation streamline, there seems to be minimal effect on the downstream flow around the projectile, as can be seen in Fig. 62, which

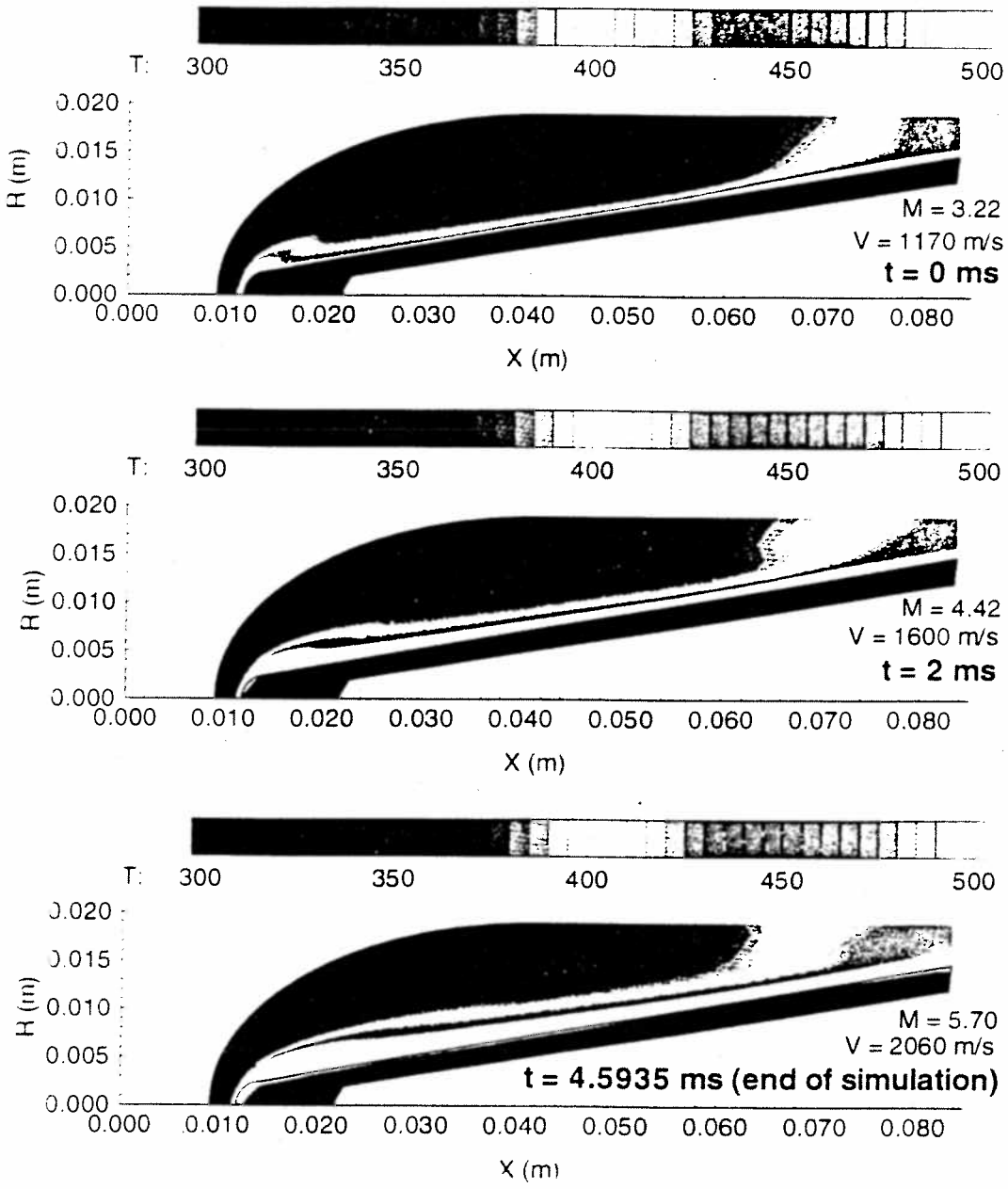

Figure 61. Temperature contours in gas and solid zones in simulation of projectile with a 2.5 mm radius aluminum nose tip, from start to 4.5935 ms.

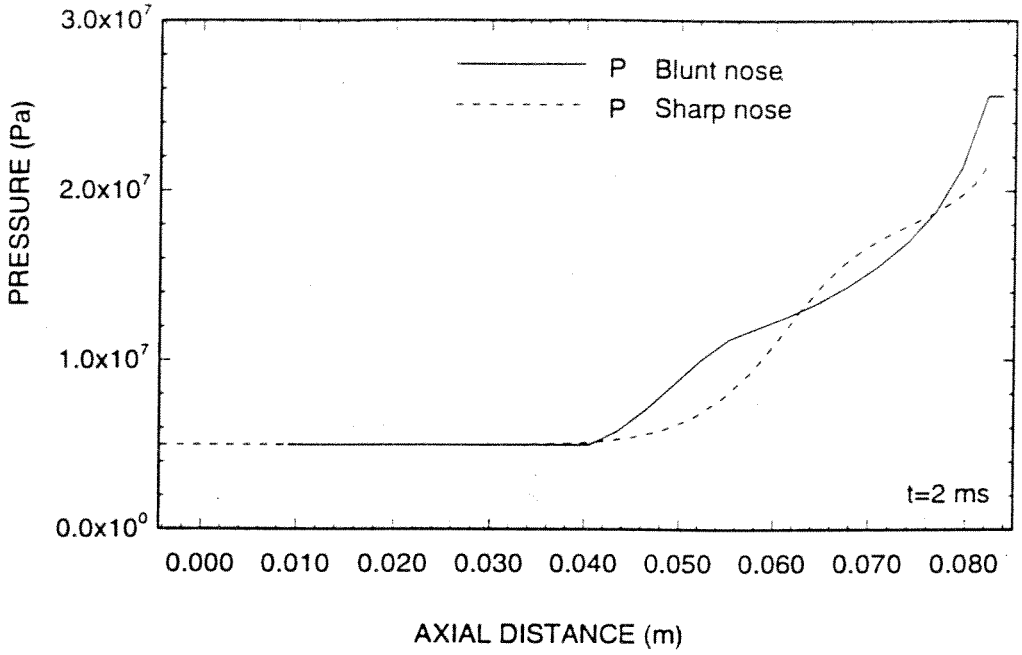

Figure 62. Comparison of pressure profile at tube wall for 2.5 mm radius and sharp aluminum nose tips, 2 ms after start.

shows the pressures at the tube wall for both blunt and sharp noses. The pressure profiles are somewhat similar in form; the magnitudes of the pressure rises at the tube wall are not significantly altered. Although the nose itself is much shorter than a sharp nose, the character of the pressure profile does not change significantly; only the position of the profile shifts, moving less than 1 cm forward from the throat. One effect is that the pressure profile of such a blunted nose would be difficult to distinguish from those of moderately canted or displaced sharp-nosed projectiles.[50] The current laboratory configuration, with its limited instrumentation density, is thus limited in its ability to study the aerodynamic heating of ram accelerator projectiles.

The surface temperature history of this projectile is shown in Fig. 63. Figure 64 shows the normal heat flux to the surface of the nose. From comparison of the two figures, one can see that the surface temperature peaks just downstream of the stagnation point at the tip, where the normal heat flux in the gas at the surface is at a maximum. Comparing Fig. 63 with the corresponding plot for the sharp nose (Fig. 27), the surface temperature of this blunt nose rises much more slowly than that of the sharp nose, showing that blunting the nose does reduce the aerodynamic heating. Note, however, that the melting temperature is still reached by the time of unstart of HS 1062.

The yield parameter in the 2.5 mm nose are shown in Fig. 65. The yield parameter in the region near the projectile throat is, as in the sharp nose simulation, well below unity, though the peak yield parameter is slightly greater here (which is expected, due to the slightly greater pressure behind the reflected shock of the blunt nose). An unexpected feature of these figures is the noticeable increase in the yield parameter in the solid nose tip. Although the levels here are no higher than those in the walls near the throat, they are higher than the general levels found in a sharp nose. Figure 66 shows an expanded view of the nose tip. Apparently, even at this large radius, the surface of the tip would still melt, albeit not in a spherical manner.

Variation in Nose Cone Angle

In an attempt to improve the reliability and robustness of ram accelerator experiments, projectile configurations other than the standard shown in Figs. 4 and 5 have been suggested. Among these suggestions is a variation in the nose cone angle. Thus, the next simulation presented here is that of a projectile with a 15°-angle nose. The dimensions used in this simulation are shown in Fig. 67; the internal dimensions were arbitrarily chosen to give a slightly thicker wall than in the 10°-nose, since the

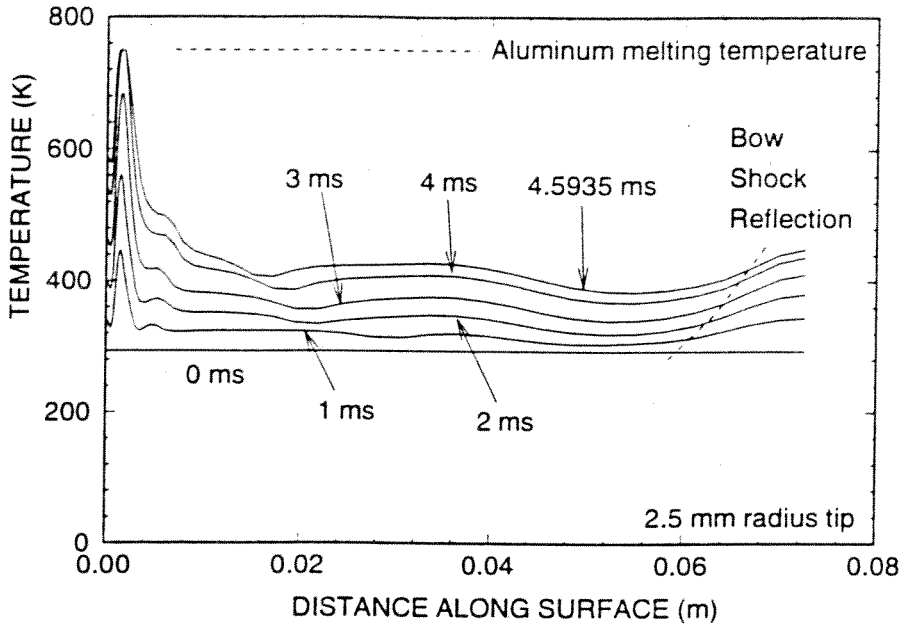

Figure 63. Surface temperature of aluminum projectile nose with a 2.5 mm radius tip.

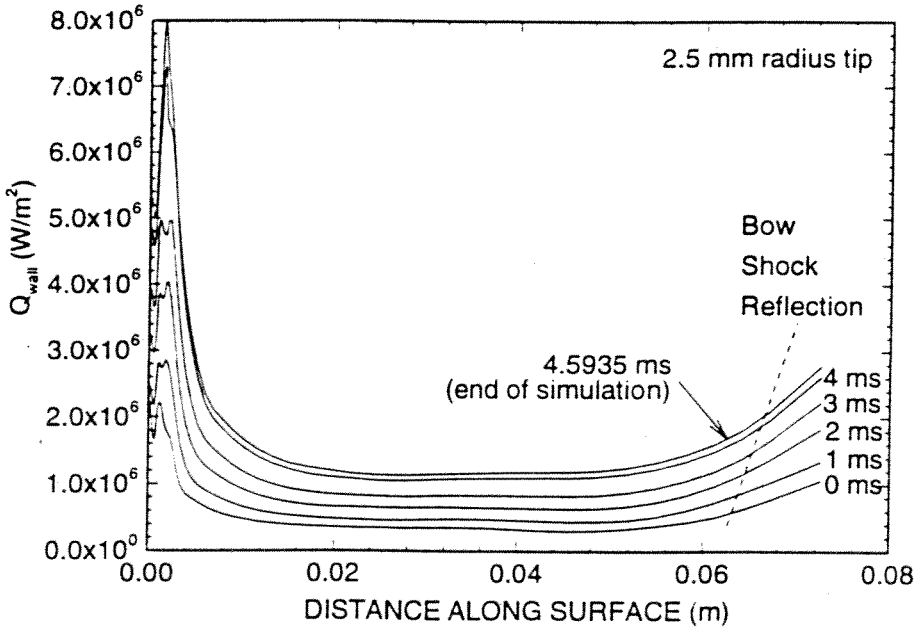

Figure 64. Variation of normal heat flux to surface of projectile with 2.5 mm radius aluminum nose tip.

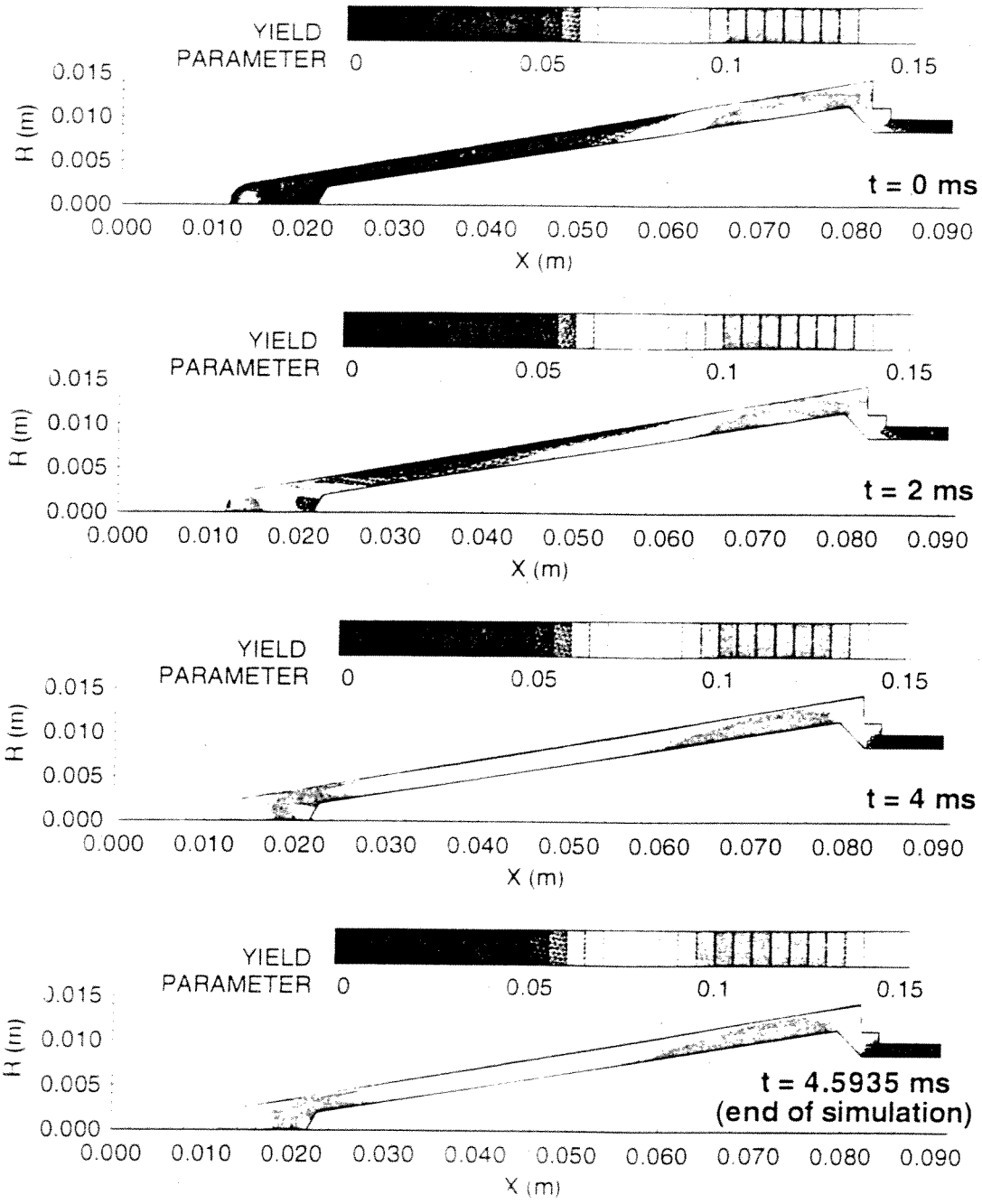

Figure 65. Yield parameter contours in projectile nose with a tip radius of 2.5 mm.

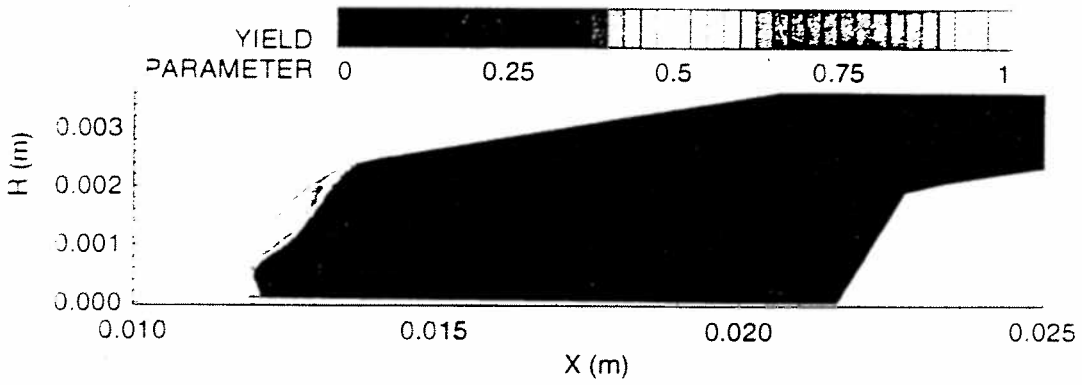

Figure 66. Yield parameter contours in projectile nose tip with a radius of 2.5 mm at end of experiment.

slight increase in mass here is more than compensated by the decrease due to the reduction in nose length. The velocity history and gas mixture imposed in this case are the same as those used in the simulation of HS 1062, allowing for a direct comparison between the two nose angles.

The resulting temperature contours are shown in Fig. 68. As expected, the shocks are stronger than for the 10°-noses, as can be seen by comparison with previous figures. The shock reflection impinges the surface of the nose closer to the throat than in the smaller angle noses, and reaches the throat by about 1 ms after the start of the experiment. From a cursory inspection of the temperature contours in the solid zone, the rate at which a significant temperature rise penetrates into the surface is roughly of the same order of magnitude as that of the 10° aluminum nose.

The surface temperature is shown in Fig. 69, and the normal heat flux of the gas at the surface of the nose is shown in Figure 70; these can be compared with Figs. 27 and 28. The normal heat flux is slightly greater than that of the 10° aluminum nose, but

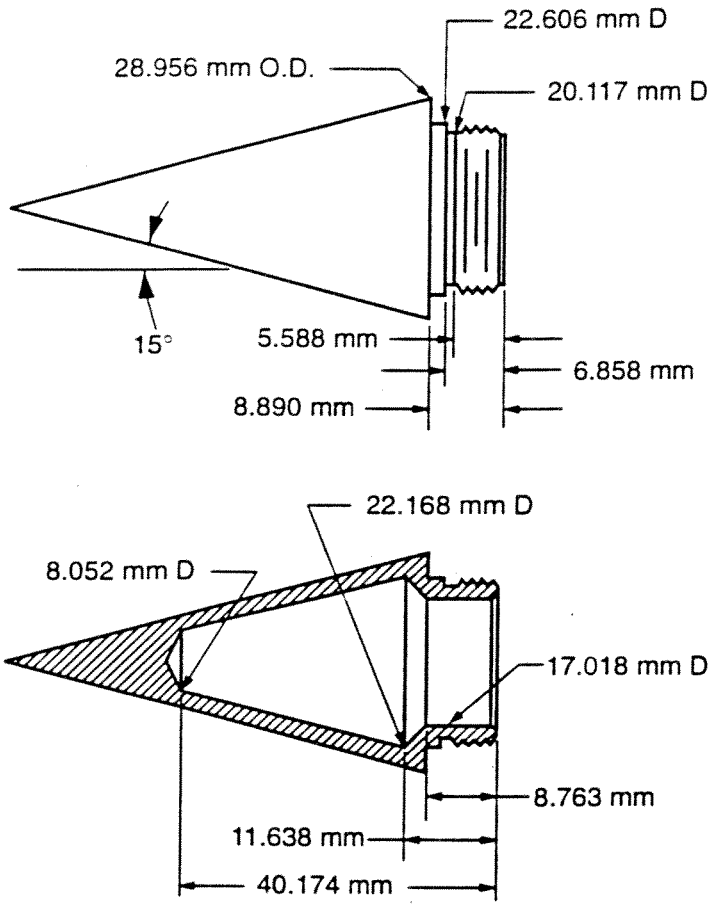

Figure 67. Dimensions of 15°-nose used in computer simulation.

the surface at the nose tip increases in temperature much more quickly, and eventually, at the end of the simulation, a much larger area has reached the alloy melting temperature. Apparently, the heating of noses with large cone angles is more severe than with noses with shallower angles. The increase in heating is probably caused by the greater temperatures behind the steeper shock angle of the larger-angle nose.

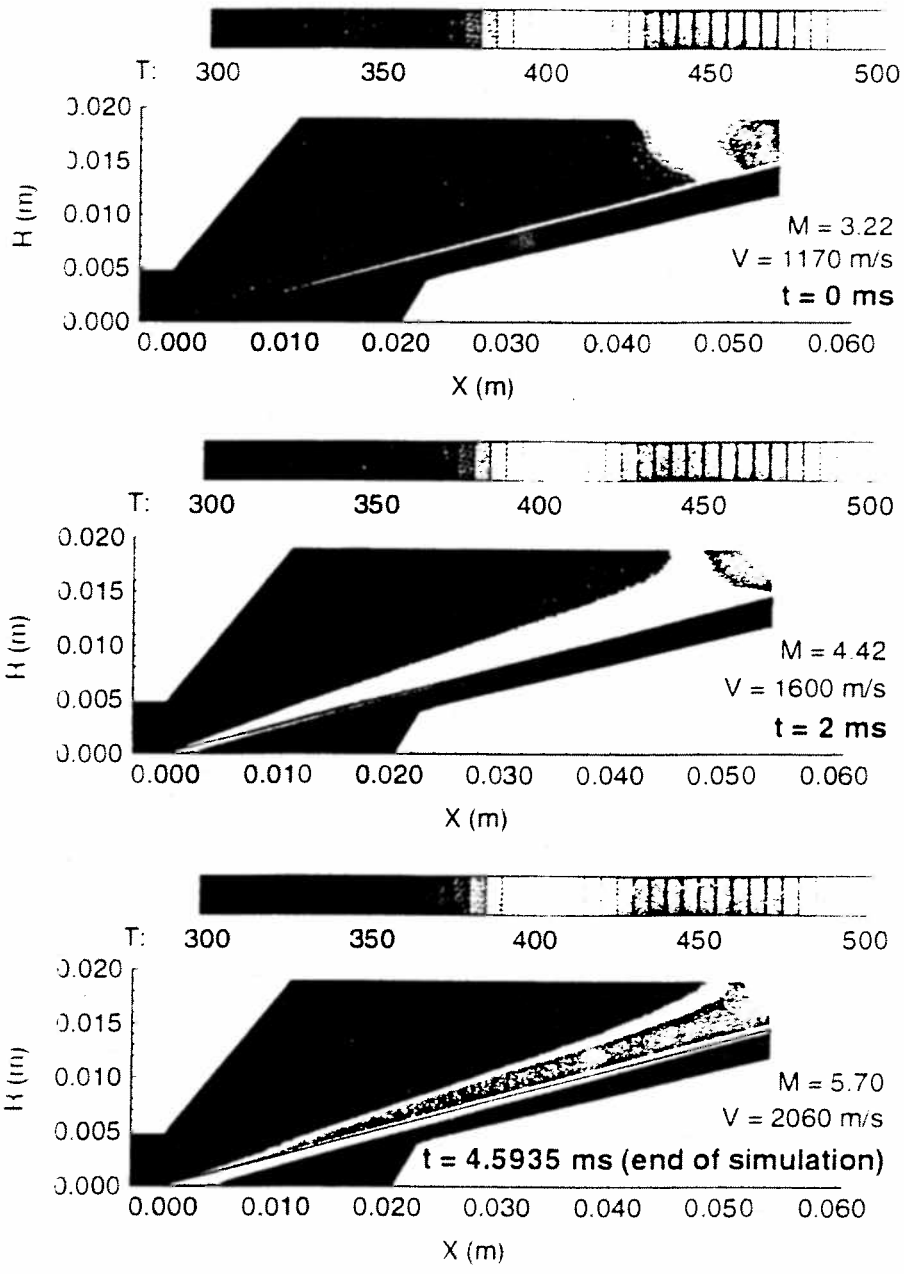

Figure 68. Temperature contours in gas and solid for the 15°-nose case

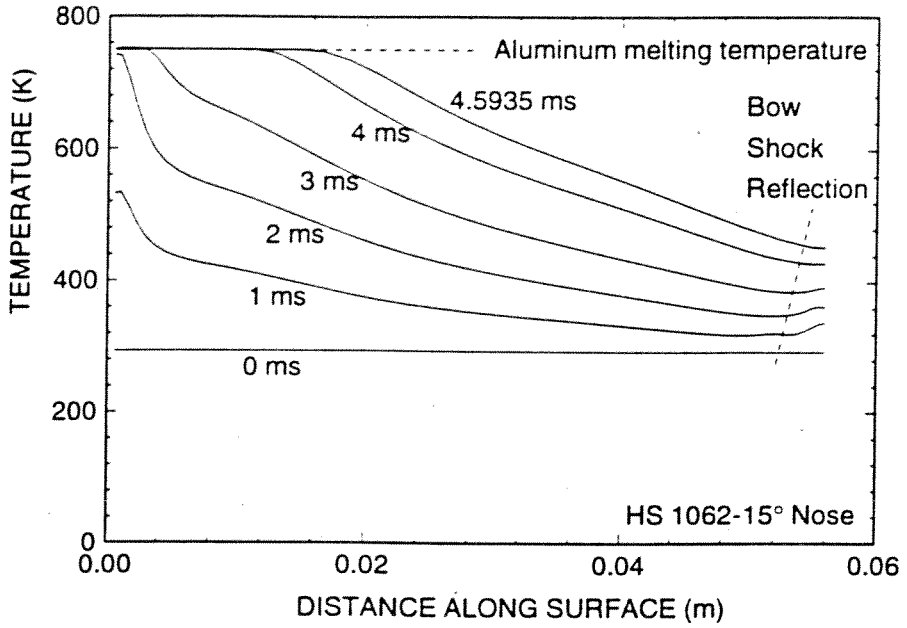

Figure 69. Surface temperature distribution of 15°-nose.

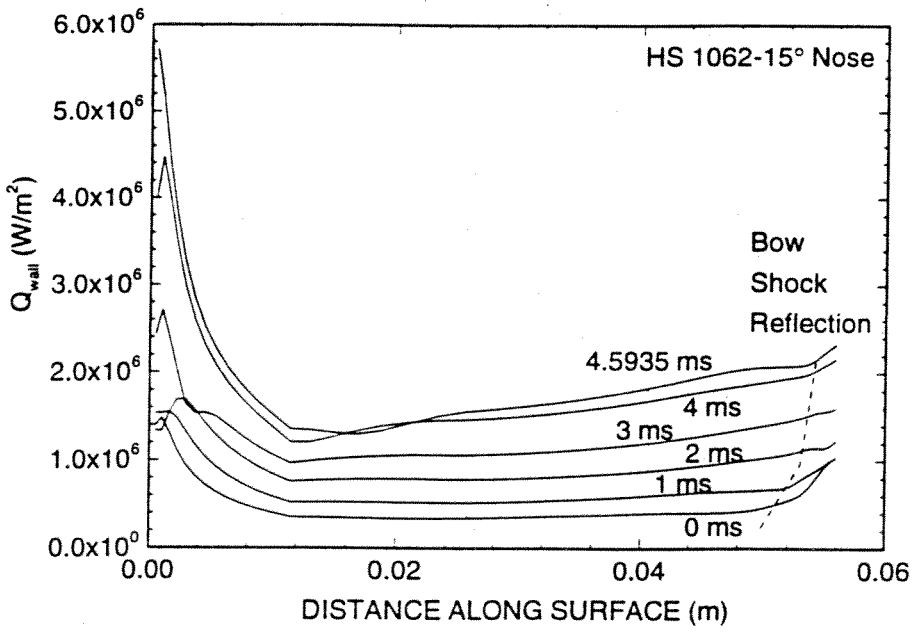

Figure 70. Variation of normal heat flux to surface of 15°-nose.

This result is different from that of the blunt-nose cases, probably because of the different characteristics of the two flows. The bow shock around a blunt nose is detached, producing a hot entropy layer on the nose. In contrast, a sharp large-angle nose produces an attached conical shock, resulting in conical self-similar flow with no entropy layer and only a thin hot boundary layer at the tip. The heat flux to the nose depends on the temperature gradient in the flow, which in turn depends on the temperature and the thickness of the layer of hot gas; that is,

$$q = -k\frac{\partial T}{\partial n} \approx -k\frac{\Delta T}{\Delta n} \tag{7.1}$$

where q is the heat flux, k is the thermal conductivity, T is the temperature, and n is the distance normal to the surface. A larger nose tip radius produces a thicker entropy layer, while the temperature behind the normal shock is ideally constant, hence resulting in a lower heat flux for blunter (larger radius) nose tips. Since the thickness of the boundary layer is relatively independent of nose cone angle, higher temperatures behind higher shock angles should result in higher heat fluxes for sharp large-angle noses.

Figure 71 shows the yield parameter for this 15°-nose. Unlike the 10°-nose, in this case the peak yield parameter in the hollow section occurs not at the start, but at the end of the simulation. The peak yield parameter is also higher, reaching a level of approximately 0.2. The shift in the timing and magnitude of the peak yield parameter is due to the increased pressure behind the steeper shock of the 15°-nose. Fig. 72 shows the pressure along the nose surface for the 10°-nose of HS 1062; the abscissa is the axial distance from the tip, normalized to the length of the nose. Over the course of the experiment, the pressure increases by less than 50%. Fig. 73 shows the corresponding pressure on the 15°-nose. Although this simulation used the same velocity history as

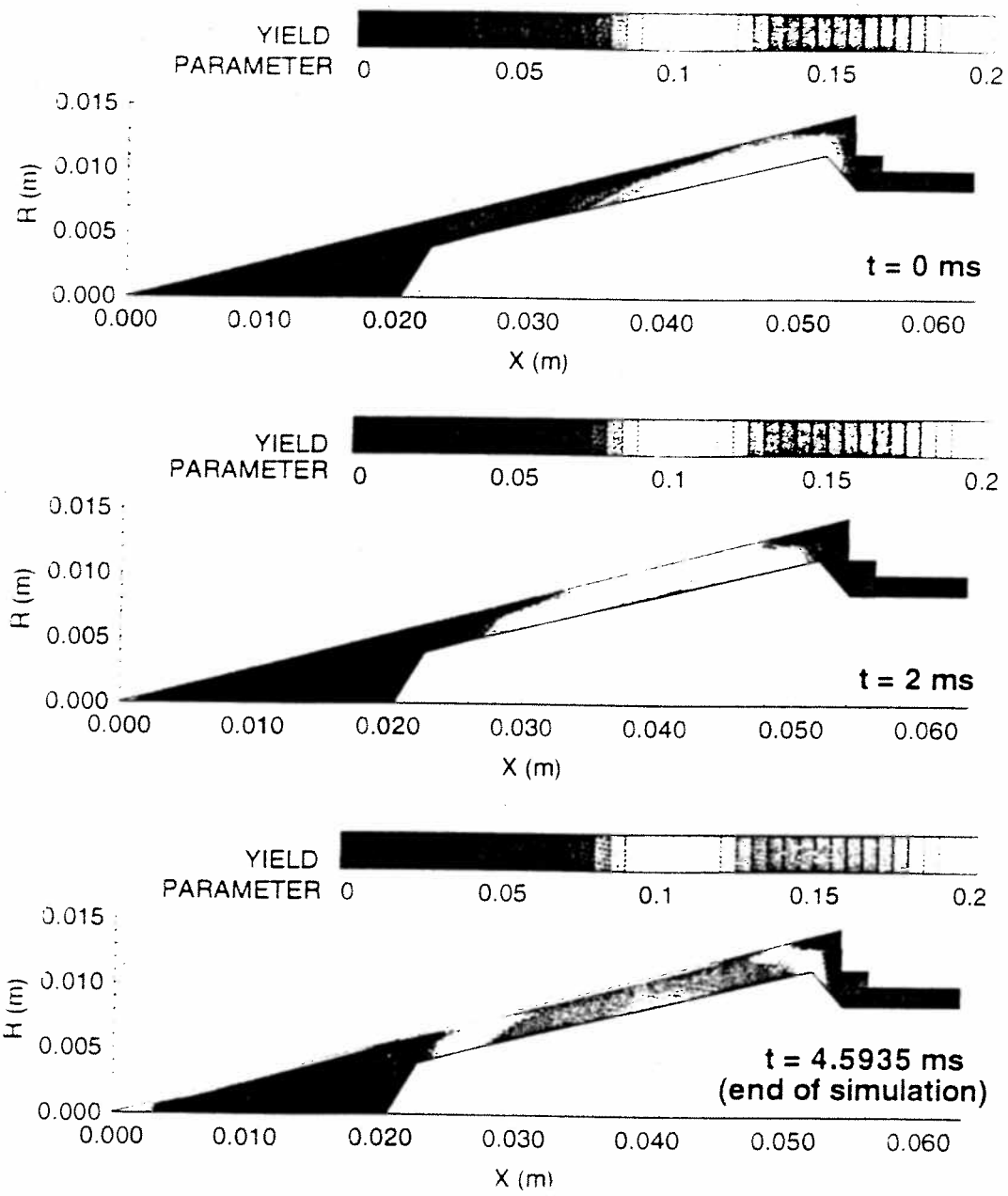

Figure 71. Yield parameter contours for a 15°-nose using the velocity history of HS 1062.

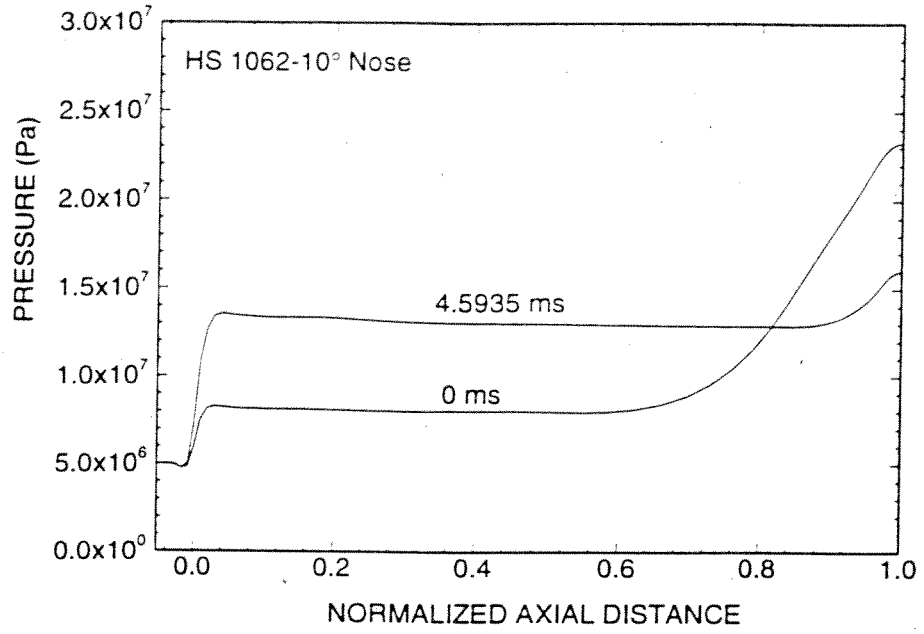

Figure 72. Pressure at surface of 10°-nose, at start and end of simulation of HS 1062

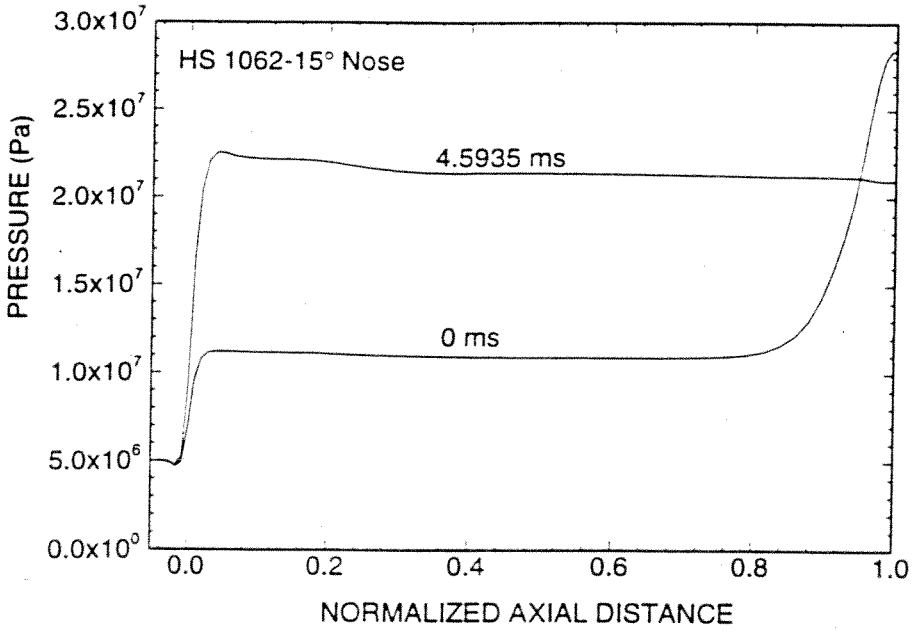

Figure 73. Pressure at surface of 15°-nose, at start and end of simulation

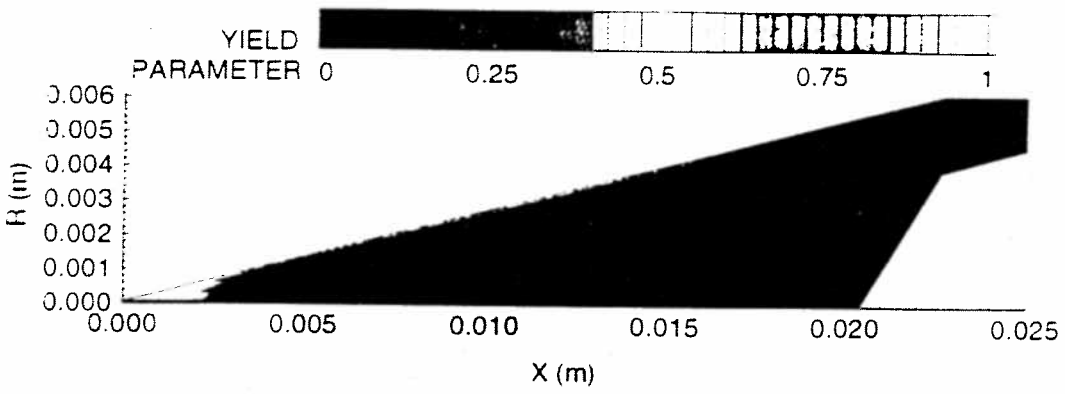

Figure 74. Yield parameter at tip of 15° nose at end of simulation.

was observed for HS 1062, the surface pressure is much higher than for the 10°-nose. Also, the surface pressure roughly doubles over the time of the simulation. The much greater rate of increase in pressure causes the yield parameter to peak much later in the simulation than before; the greater overall pressure also results in a somewhat higher peak. Contours of the yield parameter in the tip of the solid section can be seen more clearly in Fig. 74. Obviously, the tip is expected to fail; thus, although a larger cone angle is usually expected to increase the robustness of the nose cone, this nose tip is actually predicted to blunt in a fashion similar to the sharper noses.

Steel noses

Although the durability of titanium noses seems to be satisfactory, other alloys may be used in the future. One such alloy is a commonly used high-strength steel, SAE 4130. The relevant properties of this alloy are shown in Table 7.[22]

Table 7. Properties of 4130 steel.

Melting Temperature (K)	1810
Density (kg/m^3)	7845
Thermal Conductivity (J/m-s-K)	43-26 (310-1140K)
Specific Heat (J/kg-K)	461-586 (310-1140K)
Yield Tensile Strength (10^8 Pa)	11.7 (310K) 4.1 (810K)

In order to partially compensate for the much higher density of steel, the wall thicknesses of the hollow section have been reduced from those of standard aluminum projectiles. The ratio of wall thicknesses is approximately the inverse of the ratio of relative yield strengths; the intent is to produce similar yield parameter levels in the steel noses as in the aluminum noses. The resulting dimensions are shown in Fig. 75.

Although aluminum is only about 36% as dense as steel, the steel wall is 41%-57% as thick as in a standard aluminum nose. Thus, the mass of a steel nose is expected to be greater than that of a standard aluminum nose. In fact, comparing Tables 1 and 7

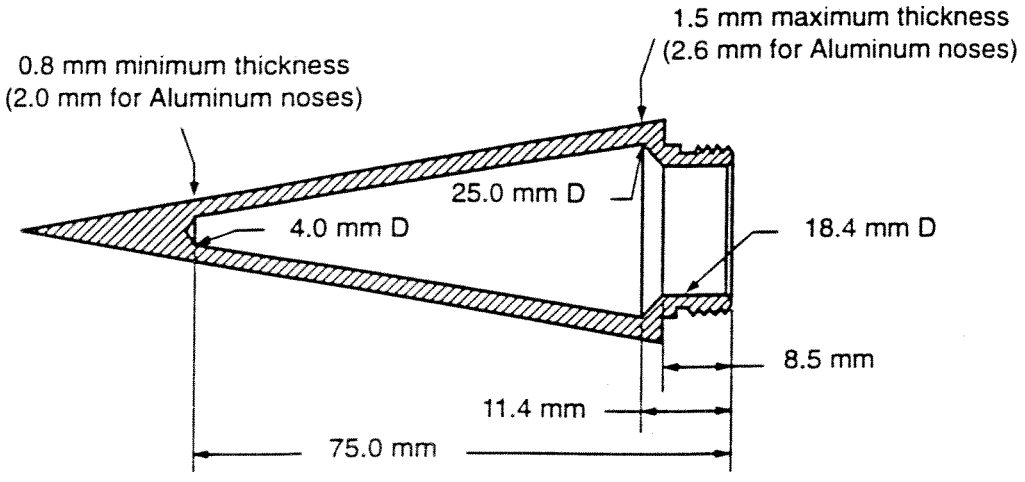

Figure 75. Internal dimensions of steel nose used in simulation.

shows that the physical properties of a steel nose would be closer to those of a titanium nose than to those of an aluminum nose. Thus, the velocity history of a steel nose is expected to be similar to that of the titanium projectiles, and so the velocity history of HS 1066 is used for a simulation of an experiment using a projectile with a steel nose.

Temperature contours from the resulting simulation are shown in Fig. 76; these can be compared with the corresponding contours for the titanium nose in Fig. 49. The two sets of figures look very similar; the thermal diffusivities of the titanium and steel alloys are both much lower than that of the aluminum alloy, leading to the relatively thin depth of penetration for the heat in both of the denser metals.

The next picture, Figure 77, shows the temperatures on the surface of the steel nose during the simulation; this figure can be compared with Fig 50. The steel surface does not heat quite as rapidly as the titanium nose, though the peak temperatures at the tip are very close. The smaller rate of rise in temperature is due to the somewhat higher thermal diffusivity of steel, which allows the heat to be conducted away from the surface more readily than in titanium. As is the case with the titanium nose, the steel nose does not approach its melting point.

The corresponding normal heat flux in the gas is shown in Fig. 78. Once again, the calculated conductive heat flux at the tip surface is negative, indicating that the boundary layer at the tip is too thin to be resolved well, resulting in the incorrect calculation. For the most part, the heat flux plots looks much like those of the titanium nose, seen in Fig. 51.

The yield parameter experienced by the steel nose is shown in Fig. 79. Over the course of the simulation, the failure levels in the hollow section never exceed a peak

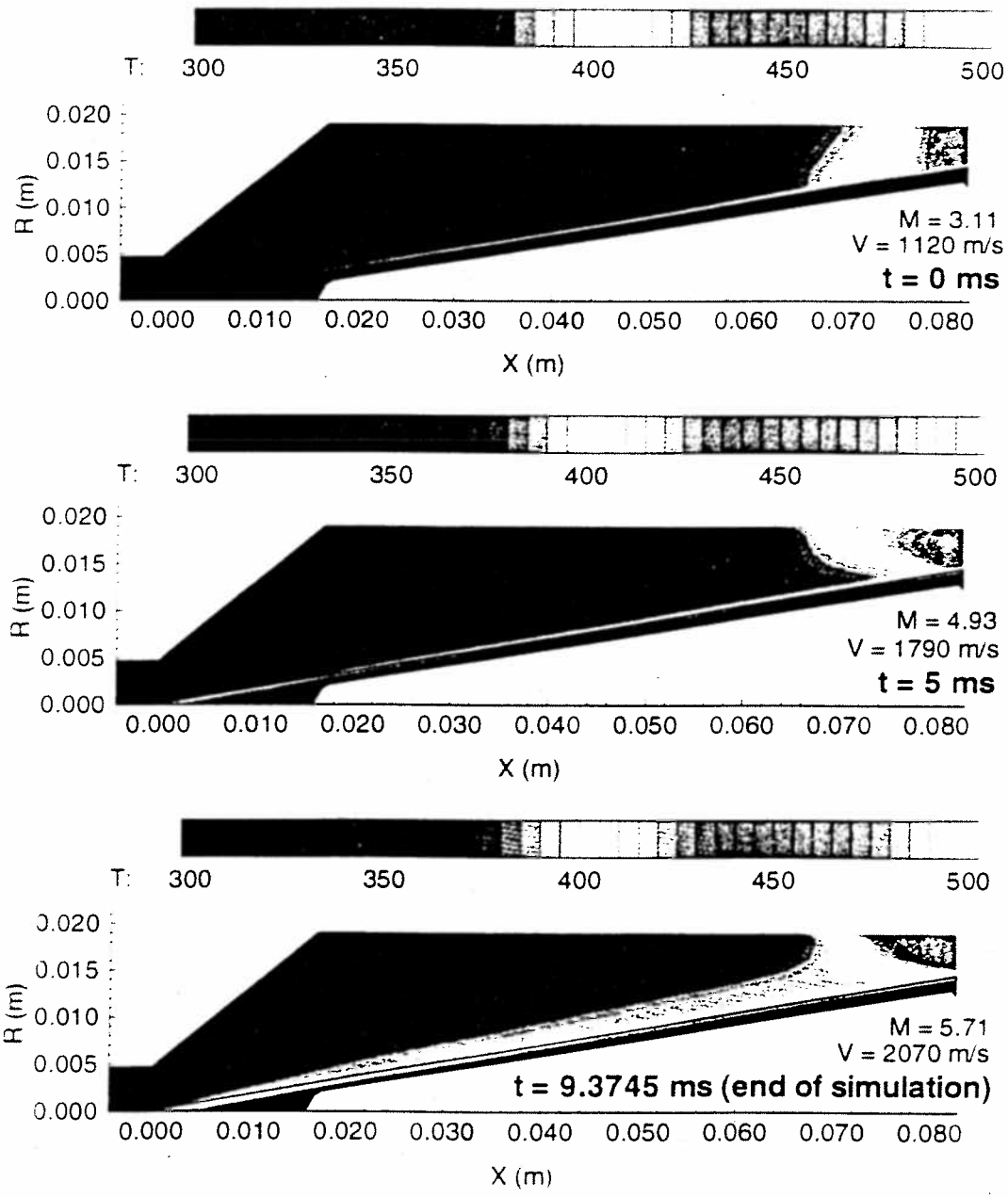

Figure 76. Temperature contours in gas and solid zones in simulation of projectile with a steel nose (start-9.3745 ms).

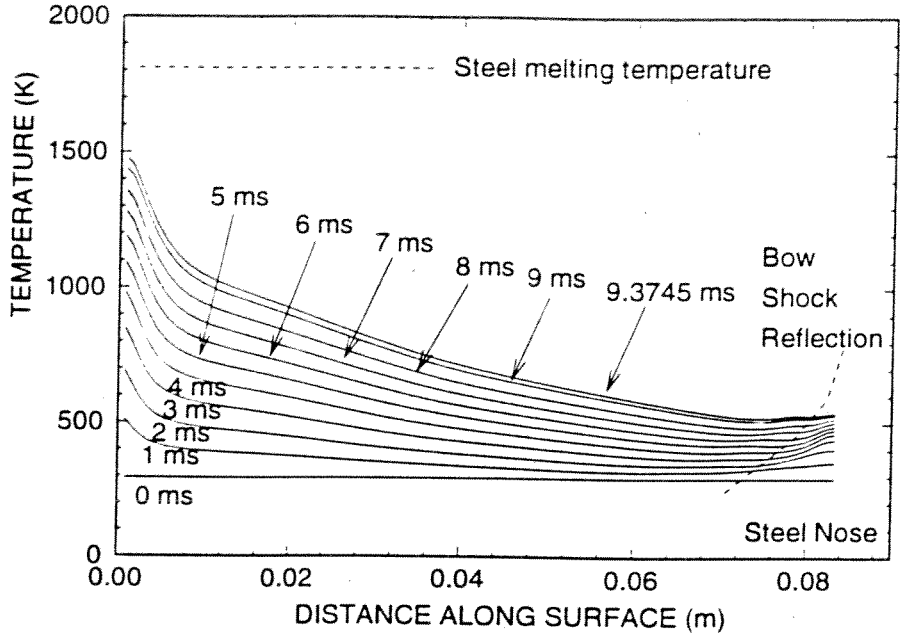

Figure 77. Surface temperature for steel nose.

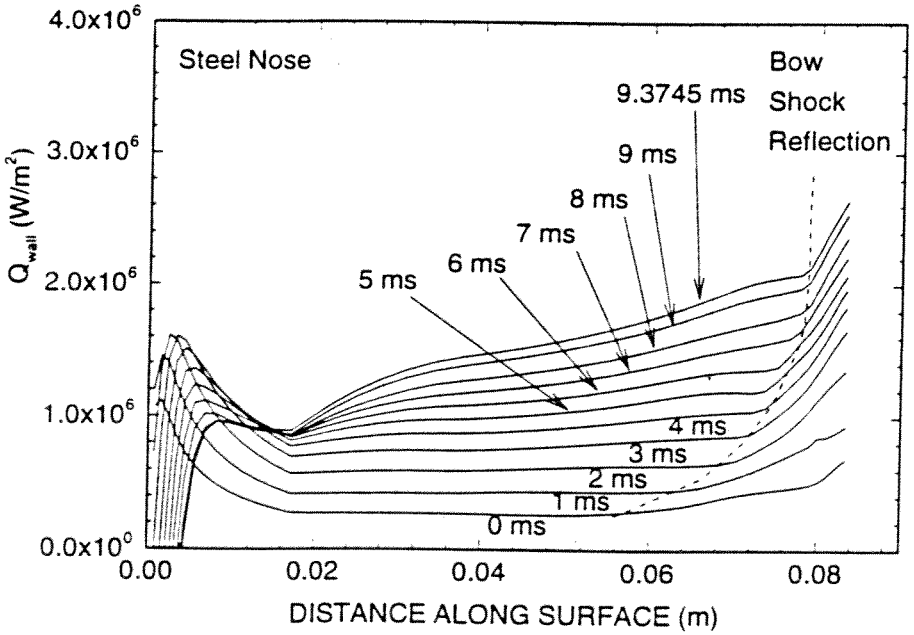

Figure 78. Calculated normal heat flux to surface of steel nose. (Negative values are due to insufficient grid resolution at the tip, where the boundary layer is thinnest.)

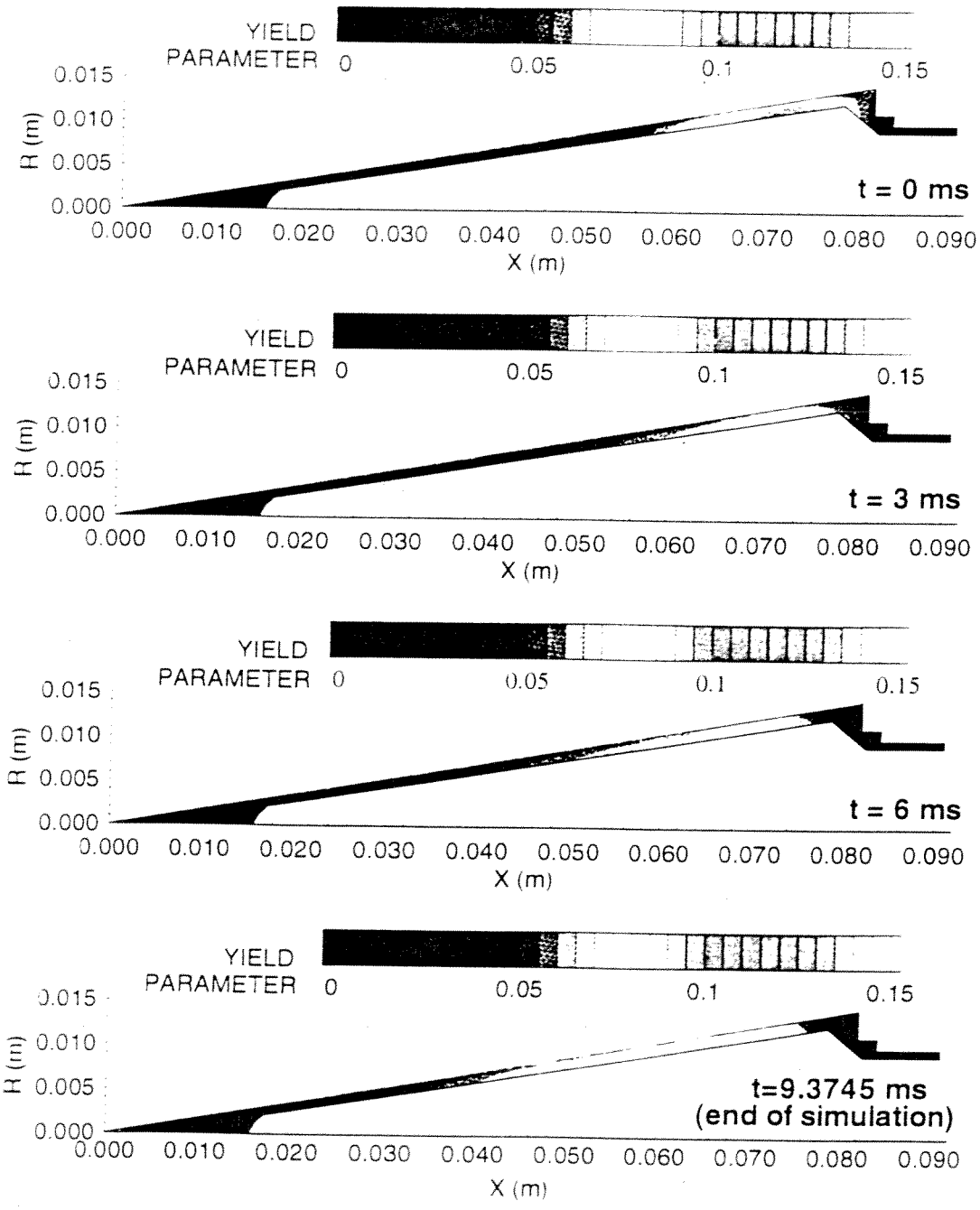

Figure 79. Yield parameter contours for steel nose using the velocity history of HS 1066, from start to end of simulation.

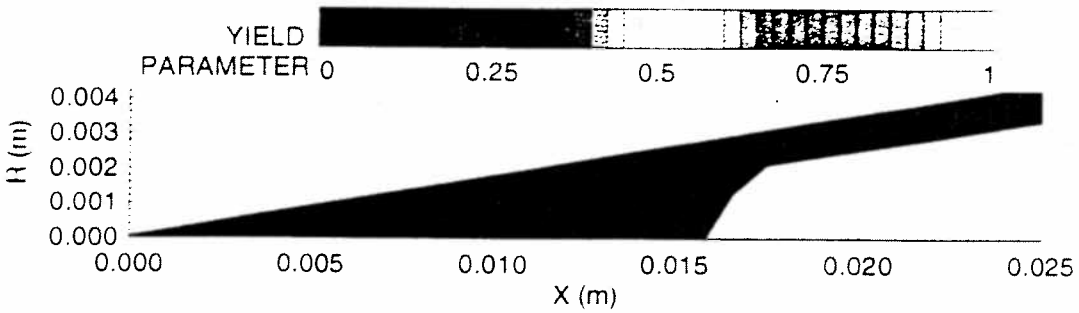

Figure 80. Yield parameter at tip of steel nose at end of simulation.

of 0.1, found at the start of the experiment in the area just ahead of the thick-walled region near the projectile throat. Note the similarity in the peak value of the yield parameter to those calculated for the aluminum noses, indicating that the specification of the wall thickness of the steel nose has been properly scaled for the difference in alloy strengths.

In contrast, the yield parameter distribution in the solid tip section does not resemble that of the aluminum nose. Contours of the yield parameter at the tip of the steel nose are shown in an expanded view in Fig. 80. Obviously, the tip shows little indication of approaching the yield criterion, as expected, since the surface does not approach the melting temperature of the alloy very closely. Thus, like the titanium nose tip, a steel nose tip should not erode from aerodynamic heating or stresses.

Composite noses

One suggestion for dealing with the harsh conditions within the ram accelerator has been to apply a protective coating on an otherwise standard projectile. Generally, these coatings either carry excessive heat away from the surface of the solid or act as a

barrier to heat. Heat carriers include highly conductive materials, which conduct heat away from a hot exterior surface to the cooler interior, spreading out the heat load, and ablative materials, which absorb the excess heat into the heat of fusion or vaporization and are carried away by the surrounding flow. Unfortunately, since aluminum is already a good conductor of heat, coating aluminum projectiles with another good conductor is not expected to significantly improve their durability. Also, the application of significant thicknesses of ablative coatings is difficult, and to date the use of a durable ablator has not been perfected.

The application of a heat-resistant coating, however, may be more feasible. A standard aluminum nose can be coated with a more refractory alloy, such as the titanium alloy used previously in experiments. Such a composite nose should have many of the heat-resistant qualities of the solid titanium noses, without the penalty of large mass incurred by using the denser alloy for the entire nose.

Thus, the next computer simulation is of a standard projectile nose, but with a thin layer of titanium applied to the surface; since the outer dimensions are the same as those of a standard nose, this layer effectively replaces an equivalent thickness of aluminum. The computational mesh is very similar to that shown in Fig. 23, except for the addition of a thin zone between the previous gas and solid zones. This zone, with a thickness of approximately 0.1 mm, simulates the presence of a very thin layer of titanium. Since the layer is so thin, the mass of the nose is expected to be similar to that of standard aluminum noses; with a standard mass, a velocity history similar to that of HS 1064 (at least up to the time of unstart of HS 1064) is expected for this projectile configuration. Thus, the velocity history of that experiment is used in this simulation.

The temperature contours of the titanium-coated nose are shown in Fig. 81. Since the Mach number history is unchanged, the temperature contours of the gas flow appear much the same as those shown in Figs. 32, as expected. However, due to the low thermal conductivity of the titanium, the temperature contours of the coated nose show much less penetration of heat into the underlying aluminum. Figure 82 shows expanded views of the temperature contours in the coating at the end of the simulation. The inner surface of the titanium coating is much cooler than the outer surface; the inner surface heats up significantly only at the tip. Expanded views of the uncoated and coated nose tips are compared in Figs. 83 and 84. Obviously, the coated nose shows much less heating of the aluminum, with most of the high temperature staying within the titanium layer and a small volume of aluminum alloy approaching its melting temperature.

The surface temperatures of this nose are shown in Fig. 85. The corresponding normal heat fluxes to the nose are shown in Fig. 86. As expected, the form of the surface temperatures and heat fluxes resemble more those of titanium noses than aluminum noses: a temperature of 750 K is reached at the tip in two milliseconds, and the normal heat flux in the gas at the tip is negative for much of the simulation (once again indicating that the surface heat flux at the tip cannot be properly calculated, due to the coarseness of the grid spacing).

The temperatures at the interface between the titanium layer and the underlying aluminum are shown in Fig. 87. Evidently, the lower thermal diffusivity of titanium limits the heat flux reaching the underlying aluminum, and so the latter does not heat up rapidly. Thus, the presence of the coating has delayed the onset of melting in the aluminum, at least beyond the time of unstart of HS 1064.

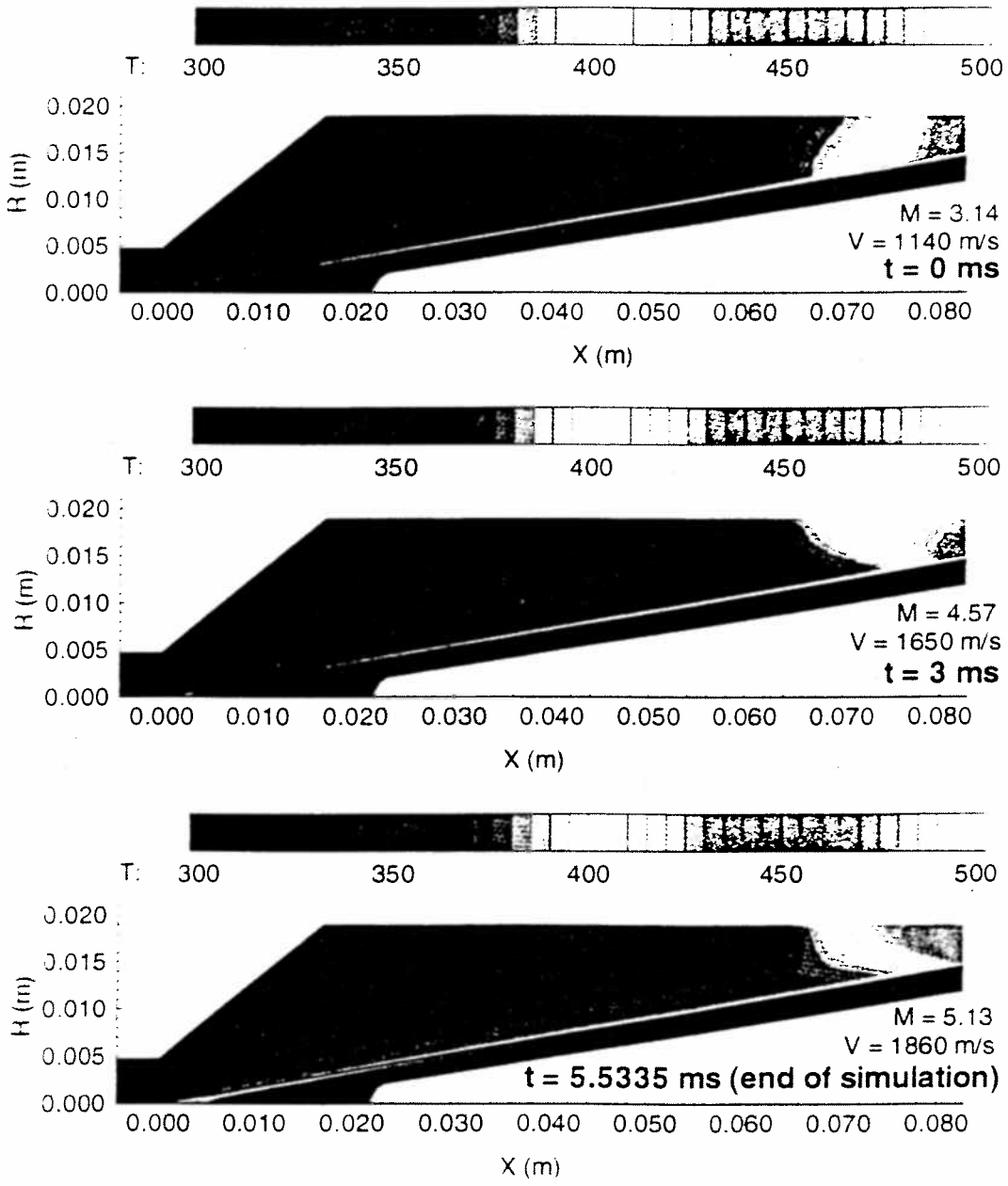

Figure 81. Temperature contours for titanium-coated projectile nose. (Ti layer is 0.11 mm thick.)

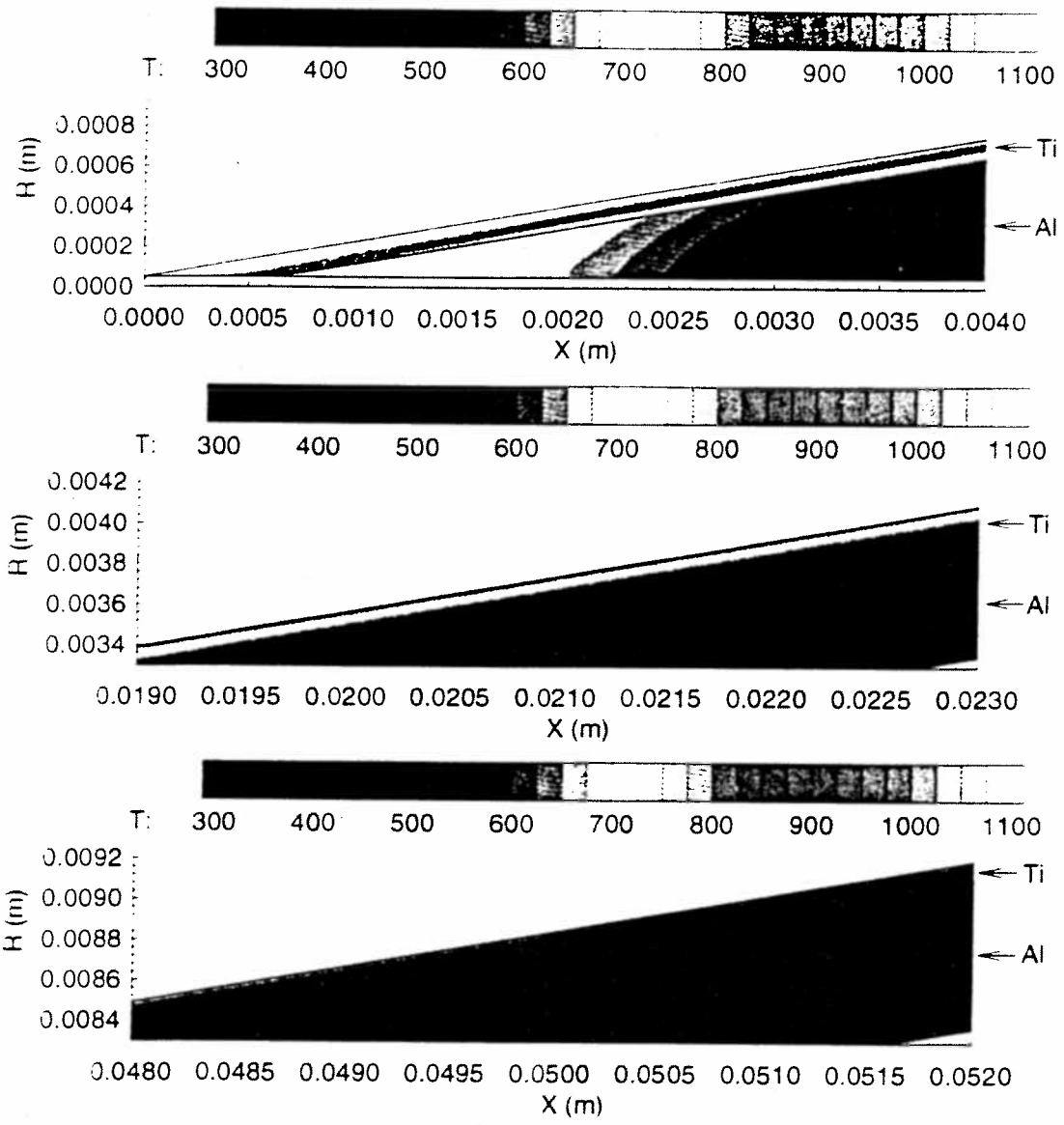

Figure 82. Expanded view of temperature contours in titanium-coated aluminum nose at selected points at end of simulation

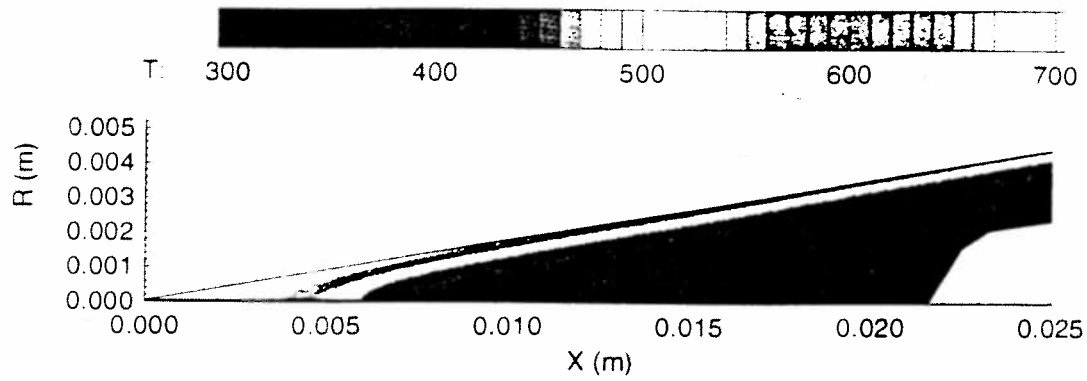

Figure 83. Temperature contours in tip of uncoated nose of aluminum projectile 5.5335 ms after start of simulation (time of unstart of HS 1064).

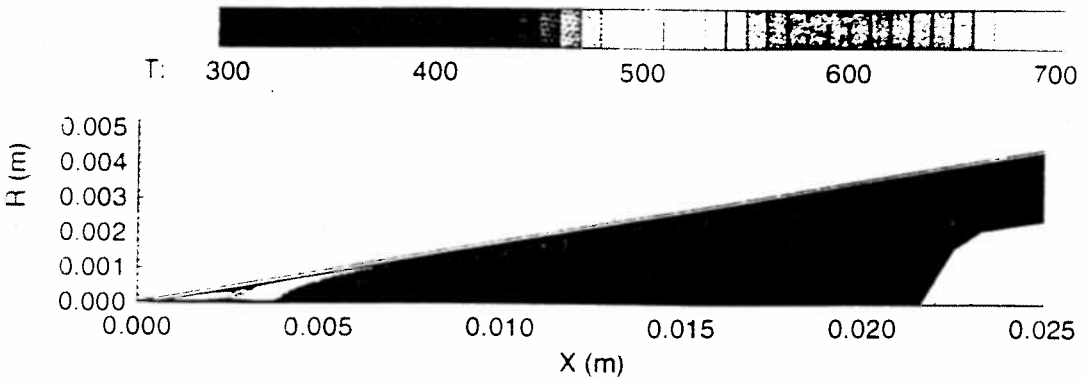

Figure 84. Temperature contours in tip of titanium-coated nose of aluminum projectile 5.5335 ms after start of simulation (time of unstart of HS 1064).

Figure 88 show contours of the yield parameter in the titanium-coated aluminum nose over the course of the simulation. The state of stress in the hollow section is similar to that of the uncoated nose shown in Fig. 35. An expanded view of the yield parameter in the solid tip section is shown in Fig. 89. Comparison with Fig. 36 shows that less of the nose tip is predicted to meet the Von Mises failure criterion; thus, the tip of the coated nose is predicted to erode much less. (Note that, although the yield

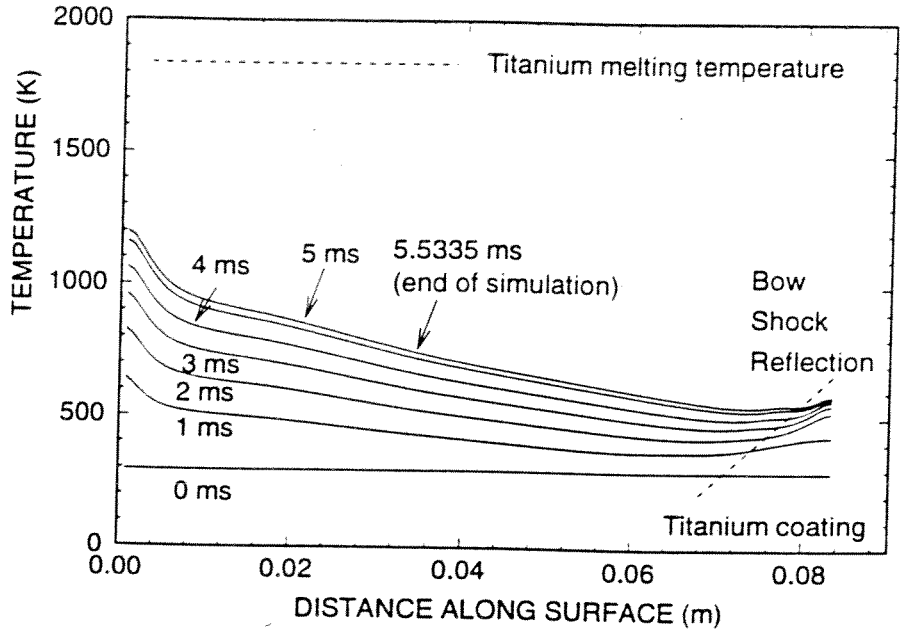

Figure 85. Temperatures on surface of titanium-coated projectile nose.

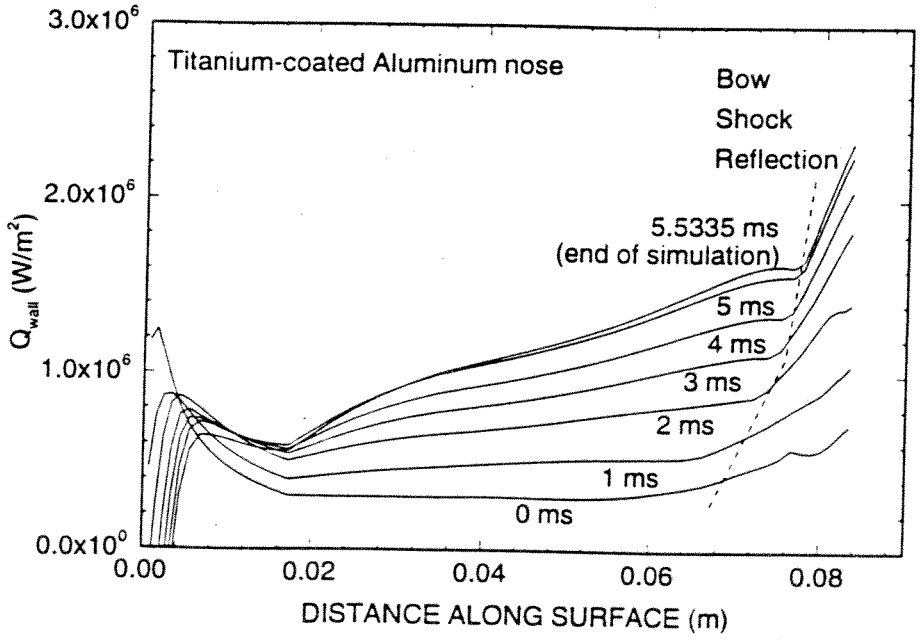

Figure 86. Variation of normal heat fluxes to surface of titanium-coated projectile nose.

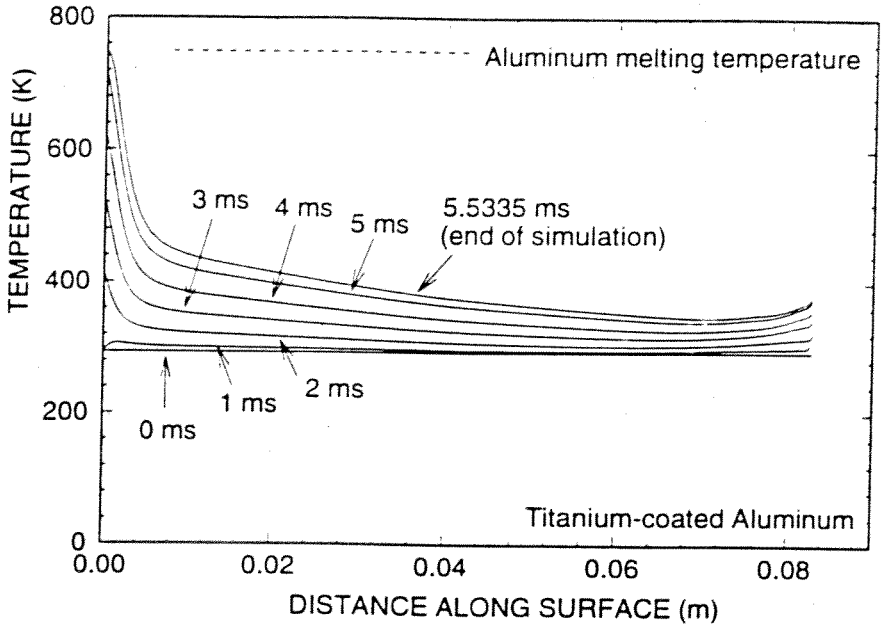

Figure 87. Temperatures between alloy layers of titanium-coated aluminum nose.

parameter in a thin layer on the surface appears to reach a level of 1.0, thus meeting the Von Mises failure criterion, this layer actually corresponds to the titanium coating. For computational convenience, the stress state in the entire nose is normalized to a single yield stress; since the coated nose is mostly aluminum, the yield stress of the aluminum alloy was used. Thus, the stress state in the coating actually does not meet the yield criterion of the titanium alloy.)

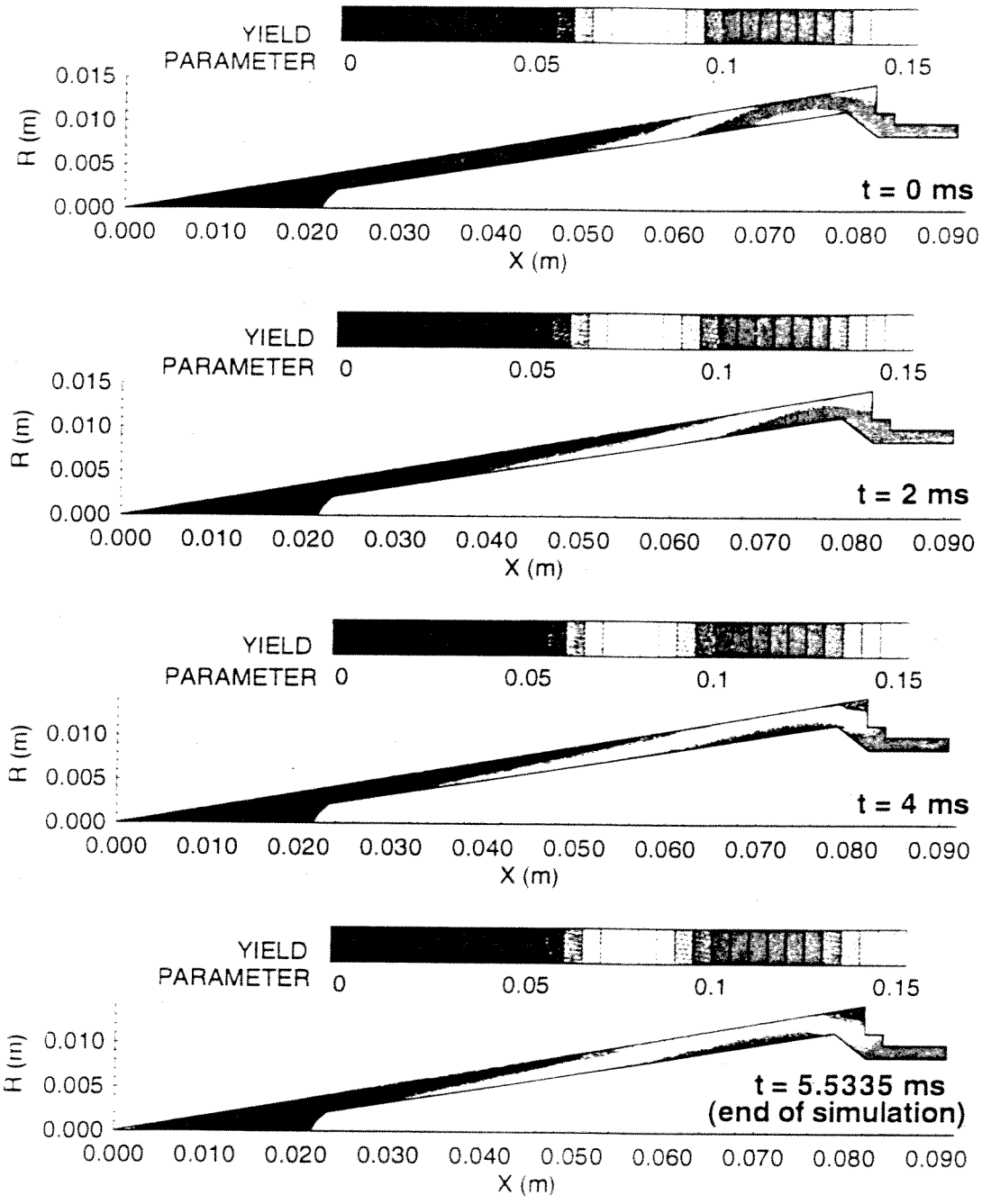

Figure 88. Yield parameter contours of titanium-coated projectile nose.

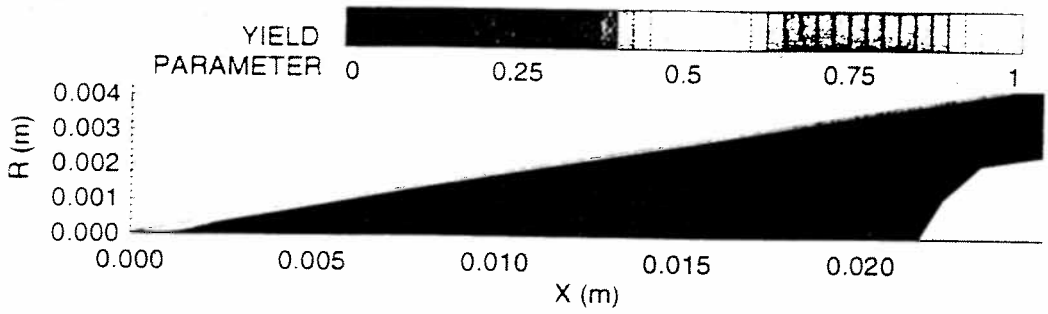

Figure 89. Yield parameter in tip of titanium-coated aluminum nose at end of simulation.

8. Conclusion

The evidence presented in this dissertation clearly indicates the superior performance (as measured by peak velocity and experiment lifetime) of ram accelerator projectiles equipped with heat-resistant noses. Both the experimental data and the computational simulations indicate that the more refractory noses endure the harsh conditions of high-velocity ram acceleration better than the standard aluminum noses.

The experimental data consist of several pairs of experiments. Each pair compares the maximum velocity attained by nearly identical projectiles, differing mainly in the alloy used to construct the nose. With nearly identical gas mixture compositions and fill pressures in the ram accelerator, these experiments provide a controlled study of the effects of projectile material on overall performance. The result of these experiments is that projectiles with titanium alloy noses generally attain a higher peak velocity, and survive for longer periods of time at high velocity, than standard projectiles with aluminum alloy noses. This result seems to hold for different alloys used in projectile body construction and different staging configurations of the ram accelerator tube. Since the major variation in parameters is the nose alloy, the implication is that the inherent differences in properties of the alloys, particularly mechanical strength, heat capacity, density, and thermal conductivity, are major factors in limiting the maximum velocity of the projectile.

Because of the limitations in the available instrumentation in the ram accelerator facility at the University of Washington, computational methods were used for more in-depth study of these factors. In the pursuit of greater understanding, a new method of calculating the extent of aerodynamic heating on ram accelerator projectiles has been developed. In this method, a computer program solves the unsteady axisymmetric Navier-Stokes equations for the turbulent gas flow around the projectile and the

unsteady axisymmetric heat equation within the projectile; the two solutions are coupled by a finite-volume formulation of the energy conservation equation on the gas-solid interface.

Using this computer program, the temperature histories of projectiles can be reconstructed from the velocity histories of laboratory experiments. Simulations of the alloy comparison experiments confirm that the aluminum projectile nose tips are likely melting, eroding into a blunt configuration, while the titanium nose tips do not melt and thus are much less likely to erode, remaining sharp. Further simulations with blunt nose tips indicate that, although blunting reduces the heat flux to leading edges of hypersonic bodies, melting temperatures are still reached in these noses; also, the concomitant pressure profile on the tube wall is unfortunately similar to that of sharp noses, indicating that detecting moderate to large nose erosion with the standard laboratory diagnostic instrumentation would be difficult. Projectile noses with larger cone half-angles are shown to likely experience even worse tip erosion than standard noses, due to the higher temperatures and pressures behind steeper conical shocks. A simulation of a high-strength steel nose indicates that steel is somewhat resistant to heat, much more so than aluminum; however, steel noses will probably not be used in the near future of the ram accelerator, due to the rather high density of steel (which would lead to projectiles too massive to accelerate at an acceptable rate).

Of course, a goal of these simulations is to design a nose that both resists erosion due to aerodynamic heating and is low in mass. The most promising projectile nose configuration seems to be one with a basic aluminum structure, but coated with a refractory material. The simulation of a titanium-clad aluminum nose indicated that such a nose would combine the better properties of the two materials; namely, the low

thermal diffusivity, high strength, and high melting temperature of titanium, with the relatively low density and good strength-to-weight ratio of aluminum. Such a projectile nose would be lightweight, yet shielded from the deleterious effects of aerodynamic heating.

Naturally, more study of projectile heating effects needs to be performed. A significant advance would be to extend the current two-dimensional/axisymmetric computer code to three dimensions, as well as adding the simulation of chemical combustion. Then, the contributions of heating on the projectile body, including the gas-bearing sliding friction on the fins, the bow shock of the fins, and the combustion zone travelling with the projectile, could be included in ram accelerator analysis. Additional experiments to study other projectile materials should also be performed. Both carbon-carbon composites and ablative coatings have been successfully used to protect hypersonic bodies from damage in high-temperature environments, and may prove to be beneficial to ram accelerator projectiles. Additionally, the development of better thermal probes, particularly to diagnose the temperature in the projectile itself, would go far in improving the understanding, and thus the eventual performance of the ram accelerator.

References

1. Hertzberg, A., Bruckner, A.P., and Bogdanoff, D.W., "Ram Accelerator: A New Chemical Method for Accelerating Projectiles to Ultrahigh Velocities," AIAA Journal, Vol. 26, No. 2, 1988, pp. 195-203.

2. Bruckner, A.P., Knowlen, C., Hertzberg, A., and Bogdanoff, D.W., "Operational Characteristics of the Thermally Choked Ram Accelerator," Journal of Propulsion and Power, vol.7, 1991, pp. 828-836.

3. Bruckner, A.P. and Knowlen, C., "Overview of Ram Accelerator Technology," National Shock Wave Symposium, Sendai, Japan, January 14-16, 1993.

4. Strehlow, R.A., Combustion Fundamentals, McGraw-Hill, New York, 1984, Ch. 9.

5. Hertzberg, A., Bruckner, A.P., and Knowlen, C., "Experimental investigation of ram accelerator propulsion modes," Shock Waves, vol.1, pp. 17-25, 1991.

6. Kull, A.E., Burnham, E.A., Knowlen, C., Bruckner, A.P., and Hertzberg, A., "Experimental Studies of Superdetonative Ram Accelerator Modes," AIAA Paper 89-2632, July 9-10, 1989.

7. Burnham, E.A., Kull, A.E., Knowlen, C., Bruckner, A.P., and Hertzberg, A., "Operation of the Ram Accelerator in the Transdetonative Velocity Regime," AIAA Paper 90-1985, July 16-18, 1990.

8. Bruckner, A.P. and Hertzberg, A., "Ram Accelerator Direct Launch System for Space Cargo," Paper No. IAF 87-211, 38th Congress of the International Astronautical Federation, Brighton, United Kingdom, October 10-17, 1987.

9. Bogdanoff, D.W., "Ram Accelerator Direct Space Launch System: New Concepts.", Journal of Propulsion and Power, vol. 8, No. 2, 1992, pp. 481-490.

10. Bruckner, A.P., Chew, G., Auzias de Turenne, J., and Dunmire, B., "Investigation of Hypersonic Ramjet Propulsion Cycles Using a Ram Accelerator Test Facility," Paper No. IAF 91-275, 42nd Congress of the International Astronautical Federation, Montreal, Canada, October 5-11, 1991.

11. Bruckner, A.P., Knowlen, C., and Hertzberg, A., "Applications of the Ram Accelerator to Hypervelocity Aerothermodynamic Testing," AIAA Paper 92-3949, July 1992.

12. Naumann, K.W. and Bruckner, A.P., "Ram Accelerator Ballistic Range Concept for Softly Accelerating Hypersonic Free-Flying Models," Journal of Aircraft, vol. 31, no. 6, November-December, 1994, pp. 1310-1316.

13. Kruczynski, D., "Experimental Demonstration of a 120 mm Ram Accelerator," 29th JANNAF Combustion Subcommittee Meeting, NASA Langley Research Center, Hampton, VA, October 19-23, 1992.

14. Giraud, M., Legendre, J.F., and Simon, G., "Ram Accelerator Studies in 90 mm Caliber," 43rd Meeting of the Aeroballistic Range Association, Columbus, OH, September 28-October 2, 1992.

15. Chang, X., Kanemoto, H., and Taki, S., "A Rectangular Ram Accelerator Is Being Made at Hiroshima University," Paper No. ISTS 94-a-05, 19th International Symposium on Space Technology and Science, Yokohama, Japan, May 15-24, 1994.

16. Sasoh, A. and Takayama, K., "Preparatory Studies of RAMAC at Institute of Fluid Science, Tohoku University," First International Workshop on Ram Accelerator, Saint-Louis, France, September 7-10, 1993.

17. Anderson, J.D., Hypersonic and High Temperature Gas Dynamics, McGraw-Hill, New York, 1989, pp. 250-256.

18. Ibid, pp. 14, 295-297.

19. Soetrisno, M., Imlay, S.T., and Roberts, D.W., "Numerical Simulations of the Transdetonative Ram Accelerator Combusting Flow Field on a Parallel Computer," AIAA Paper 92-3249, July 6-8, 1992.

20. Naumann, K.W., "Heating and Ablation of Projectiles During Acceleration in a Ram Accelerator Tube," AIAA Paper 93-2184, June 1993.

21. Chew, G. and Bruckner, A.P., "A Computational Study of Projectile Nose Heating in the Ram Accelerator," AIAA Paper 94-2964, June 27-29, 1994.

22. Hucek, H.J., editor, Aerospace Structural Metals Handbook, Metals and Ceramics Information Center, Battelle Columbus Division, Columbus, OH. 1989, Report Codes 3207, 3506, 3707, and 1201.

23. Knowlen, C., Li, J.G., Hinkey, J., and Dunmire, B., "University of Washington Ram Accelerator Facility," 42nd Meeting of the Aeroballistic Range Association, Adelaide, Australia, October 22-25, 1991.

24. Panton, R.L., Incompressible Flow, John Wiley & Sons, New York, 1984, Ch. 5 and App. C.

25. Anderson, J.D., Hypersonic and High Temperature Gas Dynamics, McGraw-Hill, New York, 1989, Ch. 8.

26. Anderson, J.D., Fundamentals of Aerodynamics, McGraw-Hill, New York, 1984, Ch. 9.

27. Thompson, J.F., Warsi, Z.U.A., and Mastin, C.W., Numerical Grid Generation, Elsevier Science Publishing, New York, 1985, Chapter 3.

28. Anderson, D.A., Tannehill, J.C., Pletcher, R.H., Computational Fluid Mechanics and Heat Transfer, McGraw-Hill, 1984, p. 75.

29. Incropera, F.P., and DeWitt, D.P., Fundamentals of Heat and Mass Transfer, John Wiley & Sons, New York, 1985, p. 35.

30. Yee, H.C., Klopfer, G.H., and Montagne, J.-L., "High-Resolution Shock-Capturing Schemes for Inviscid and Viscous Hypersonic Flows," NASA-TM-100097, April 1988.

31. Klopfer, G.H.,Yee, H.C., and Kutler, P., "Numerical Study of Unsteady Viscous Hypersonic Blunt Body Flows with an Impinging Shock," NASA-TM-100096, April 1988.

32. Yee, H.C. and Harten, A., "Implicit TVD Schemes for Hyperbolic Conservation Laws in Curvilinear Coordinates," AIAA Journal, Vol. 25, No. 2, 1987, pp. 266-274.

33. Yee, H.C. and Shinn, J.L., "Semi-Implicit and Fully Implicit Shock-Capturing Methods for Nonequilibrium Flows," AIAA Journal, Vol. 27, No. 3, 1989, pp. 299-307.

34. Steger, J.L., "Implicit Finite-Difference Simulation of Flow about Arbitrary Two-Dimensional Geometries," AIAA Journal, Vol. 16, No. 7, July 1978, pp. 679-686.

35. Anderson, D.A., Tannehill, J.C., and Pletcher, R.H., Computational Fluid Mechanics and Heat Transfer, McGraw-Hill, 1984, p. 280.

36. Pratt, D.T., Department of Mechanical Engineering, University of Washington, Seattle, WA, private communication, 1992.

37. White, F.M., Viscous Fluid Flow, McGraw-Hill, New York, 1991, pp. 29, 32, 570.

38. Zagoruchenko, V.A. and Zhuravlev, A.M., Thermophysical Properties of Gaseous and Liquid Methane, Keter Press, Jerusalem, 1970, p. 207.

39. White, F.M., Viscous Fluid Flow, McGraw-Hill, New York, 1991, pp. 34-35.

40. Ibid, pp. 442.

41. Anderson, D.A., Tannehill, J.C., Pletcher, R.H., Computational Fluid Mechanics and Heat Transfer, McGraw-Hill, 1984, p. 117.

42. Anderson, J.D., Fundamentals of Aerodynamics, McGraw-Hill, New York, 1984, Ch. 9.

43. Maccoll, J.W., "The Conical Shock Wave formed by a Cone moving at a High Speed," Proceedings of the Royal Society of London, Series A, No. 898, Vol. 159, pp. 459-472, 1937.

44. Taylor, G.I., and Maccoll, J.W., "The Air Pressure on a Cone Moving at High Speeds," Proceedings of the Royal Society of London, Series A, Vol. 139, pp. 278-311, 1933.

45. Van Driest, E.R., "Investigation of Laminar Boundary Layer in Compressible Fluids Using the Crocco Method," NACA Technical Note 2597, January 1952.

46. Pappas, C.C., "Measurement of Heat Transfer in the Turbulent Boundary Layer on a Flat Plate in Supersonic Flow and Comparison with Skin Friction Results," NACA Technical Note 3222, June 1954.

47. Incropera, F.P. and DeWitt, D.P., Fundamentals of Heat and Mass Transfer, 2nd Ed., John Wiley & Sons, New York, 1985, pp. 203-204.

48. Holsapple, K.A., Dept. of Aeronautics and Astronautics, University of Washington, Seattle, WA, private communication, November 1994.

49. Popov, E.P., Engineering Mechanics of Solids, Prentice-Hall, Englewood Cliffs, NJ, 1990, pp. 441-453.

50. Hinkey, J.B., An Experimental and Numerical Investigation of the Three-Dimensional Flow Field About a Ram Accelerator Projectile, Ph.D Dissertation, University of Washington, 1994.

51. Anderson, J.D., Hypersonic and High Temperature Gas Dynamics, McGraw-Hill, New York, 1989, p. 280.

Appendix A. Finding the Dissipation Vector

A.1 Introduction

The method of Yee *et al.*[30] involves the formation of the dissipation vector $R\Phi$. At first glance, this task apparently requires the computation of R, the full matrix of eigenvectors of the flux Jacobians, and the vector Φ. Calculation of the components of Φ is itself no easy task, as it involves the inversion of the matrix R. Once R and Φ are found, they are multiplied together; this sequence must be performed at each point in the grid, and repeated for each coordinate direction. Thus, the formation of the $R\Phi$ vector could cause the computation time to be prohibitively large. Fortunately, by analyzing and taking advantage of the form of the eigenvectors, one can simplify the overall process, replacing the computationally expensive matrix inversion and multiplication with a simpler series of algebraic manipulations. The following procedure closely follows the method used by Yee and Shinn.[33]

A.2 Preliminary definitions and functions

The method of Yee *et al.*[30] requires the computation of many intermediate quantities, including eigenvalues and thermodynamic properties of the gas mixture. Note that, since the $R\Phi$ matrix is to be calculated at half-points (that is, at (j+1/2,k) and (j,k+1/2) points), these intermediate quantities need to also be calculated at half-points. Several means of calculating half-point values exist, including Roe's averaging; however, for simplicity, the half-point values used here are calculated by taking the arithmetic mean of the quantities at the whole-point locations. Thus, for example,

$$Q_{j+\frac{1}{2},k} = \frac{1}{2}\left(Q_{j,k} + Q_{j+1,k}\right) \tag{A.1}$$

Unless explicitly labelled with whole-point indices (such as (j,k)), the quantities in the following sections are half-point quantities.

The eigenvalues of the flux Jacobian matrix can be listed as follows:

$$(\lambda_\xi^1, \lambda_\xi^2, \ldots, \lambda_\xi^{N+3}) = (U, U, \ldots, U, U + k_\xi a, U - k_\xi a) \tag{A.2}$$

where U is the contravariant velocity in the ξ-direction, defined by

$$U = \xi_t + \xi_x u + \xi_y v \tag{A.3}$$

and k_ξ is defined by

$$k_\xi = \sqrt{\xi_x^2 + \xi_y^2}. \tag{A.4}$$

The "frozen sound speed" a is given by:

$$a = \sqrt{\left.\frac{\partial p}{\partial \rho}\right|_{E,\,m,\,n} + \left.\frac{\partial p}{\partial E}\right|_{\rho_i,\,m,\,n} \times [H_0 - (u^2 + v^2)]}. \tag{A.5}$$

The first partial differential in Eq. A.5 is taken by holding the energy and the mass fluxes m and n in the x and y directions constant (where $m=\rho u$, $n=\rho v$). Conversely, the second differential is taken holding the species densities ρ_i and the mass fluxes constant. H_0 is simply the total enthalpy per unit mass of mixture.

The partial differentials of Eq. A.5 require considerable manipulation for direct expression in terms of known variables. Starting with the chain rule of differentiation, and noting that

$$\rho = \sum_{i=1}^{N} \rho_i \tag{A.6}$$

then

$$\left.\frac{\partial p}{\partial \rho}\right|_{E,\,m,\,n} \equiv \sum_{k=1}^{N}\left[\left(\frac{\rho_k}{\rho}\right)\times\left.\frac{\partial p}{\partial \rho_k}\right|_{E,\,m,\,n,\,\rho_{i\,(i\neq k)}}\right] \tag{A.7}$$

From Dalton's rule of partial pressures, and the equation of state for a thermally perfect gas, the pressure can be found from the constituent species densities and the temperature:

$$p = \sum_{i=1}^{N} p_i = \sum_{i=1}^{N} \frac{\rho_i R_U T}{M_i} \tag{A.8}$$

Differentiating by parts, then

$$\left.\frac{\partial p}{\partial \rho_k}\right|_{E,\,m,\,n,\,\rho_{i\neq k}} = \frac{R_U T}{M_k} + \left(\sum_{i=1}^{N}\frac{\rho_i R_U}{M_i}\right)\cdot\left.\frac{\partial T}{\partial \rho_k}\right|_{E,\,m,\,n,\,\rho_{i,\,i\neq k}} \tag{A.9}$$

The differential on the right side of Eq. A.9 is somewhat difficult to find, since the relation between temperature, density, and energy is rather complex. The energy per unit volume of gas mixture is simply

$$E = \rho\left[e|_{T=0} + \int_0^T C_v d\tilde{T} + \frac{1}{2}(u^2+v^2)\right] \tag{A.10}$$

where the first term inside the brackets represents the energy per unit mass at absolute zero, the integral of the constant-volume specific heat represents the sensible energy, and the last term represents the kinetic energy of the mixture. The zero-level energy is a function of gas composition only:

$$e|_{T=0} = \sum_{i=1}^{N} c_i e_i|_{T=0} \tag{A.11}$$

where c_i and e_i are the mass fraction (ρ_i/ρ) and the energy per unit mass, respectively, of gas species i.

Because the variation with temperature of the constant-volume specific heat can be quite complicated, a simple exact expression for the temperature as a function of its integral (that is, the sensible heat) is impossible to find. In order to simplify calculations, the specific heat is approximated as a constant over all temperatures.

$$\int_0^T C_v d\tilde{T} \equiv C_v T \tag{A.12}$$

For most gases, the constant volume specific heat is nearly constant, so this approximation is acceptable.

Substituting Eq. A.11 and Eq. A.12 into Eq. A.10 and rearranging gives

$$T = \frac{1}{C_v}\left\{\frac{E}{\rho} - \sum_{i=1}^{N}\left[\left(\frac{\rho_i}{\rho}\right)(e_i|_{T=0})\right] - \frac{1}{2}(u^2+v^2)\right\}, \tag{A.13}$$

an expression for temperature which can be readily differentiated, resulting in the following expressions:

$$\left.\frac{\partial T}{\partial \rho_k}\right|_{e,\, m,\, n,\, \rho_{i\neq k}} = \frac{1}{C_v}\frac{\partial}{\partial \rho_k}\left[\frac{e}{\sum_{i=1}^{N}\rho_i} - \frac{\sum_{i=1}^{N}\rho_i e_i|_{T=0}}{\sum_{i=1}^{N}\rho_i} - \frac{\frac{1}{2}(m^2+n^2)}{\left(\sum_{i=1}^{N}\rho_i\right)^2}\right]\Bigg|_{e,\, m,\, n,\, \rho_{i\neq k}} \tag{A.14}$$

or

$$\left.\frac{\partial T}{\partial \rho_k}\right|_{e,\, m,\, n,\, \rho_{i\neq k}} = \frac{1}{C_v}\left[\frac{-e}{\rho^2} - \frac{e_k|_{T=0}}{\rho} + \frac{\sum_{i=1}^{N}\rho_i e_i|_{T=0}}{\rho^2} + \frac{m^2+n^2}{\rho^3}\right] \tag{A.15}$$

This expression can be substituted into Eq. A.9, giving

$$\left.\frac{\partial p}{\partial \rho_k}\right|_{\substack{m,\, n,\\ e,\, \rho_{i\neq k}}} = \frac{R_U T}{M_k} + \frac{\sum_{i=1}^{N}\frac{\rho_i R_U}{M_i}}{\rho C_v}\left[\frac{-e}{\rho} - e_k|_{T=0} + \frac{\sum_{i=1}^{N}\rho_i e_i|_{T=0}}{\rho} + (u^2+v^2)\right] \tag{A.16}$$

which is substituted into Eq. A.7, which in turn is substituted into Eq. A.5. The second partial differential of Eq. A.5 is found in a similar manner. Using the chain rule of differentiation,

$$\left.\frac{\partial p}{\partial E}\right|_{\rho_i,\, m,\, n} = \left.\frac{\partial p}{\partial T}\right|_{\rho_i} \times \left.\frac{\partial T}{\partial E}\right|_{\rho_i,\, m,\, n} \tag{A.17}$$

The first differential in Eq. A.17 is easily derived from the perfect gas law:

$$\left.\frac{\partial p}{\partial T}\right|_{\rho_i} = \sum_{i=1}^{N}\frac{\rho_i R_U}{M_i} \tag{A.18}$$

Returning to Eq. A.13 and differentiating with respect to energy, then

$$\left.\frac{\partial T}{\partial E}\right|_{\rho_i,\, m,\, n} \approx \frac{1}{C_v} \times \left[\frac{1}{\rho}\right]. \tag{A.19}$$

So, substituting Eq. A.18 and Eq. A.19 into Eq. A.17 gives

$$\left.\frac{\partial p}{\partial E}\right|_{\rho_i,\, m,\, n} = \frac{1}{\rho C_v} \sum_{i=1}^{N} \frac{\rho_i R_U}{M_i} \tag{A.20}$$

which is the second partial differential in Eq. A.5.

The frozen sound speed for an individual species k is found from

$$a_k = \sqrt{\left.\frac{\partial p}{\partial \rho_k}\right|_{E,\, m,\, n,\, \rho_{i\,(i \neq k)}} + \left.\frac{\partial p}{\partial E}\right|_{\rho_i,\, m,\, n} \times \left[H_0 - (u^2 + v^2)\right]} \tag{A.21}$$

The differentials in Eq. A.21 are found from Eq. A.16 and Eq. A.20.

A.3 The eigenvector matrices

Let R_ξ, R_η be the matrices consisting of the eigenvectors of the flux Jacobian matrices A and B. Now define a matrix of values denoted by α:

$$\alpha_{j+\frac{1}{2},k} \equiv R_{\xi}{}^{-1}_{j+\frac{1}{2},k} \cdot \frac{(Q_{i+1,k} - Q_{j,k})}{\frac{1}{2}(J_{j+1,k} + J_{j,k})} \tag{A.22}$$

with $\alpha_{j,k+1/2}$ defined similarly, but with the R_η matrix and on half-points in k. Ordinarily, computing α requires inversion of an R matrix followed by a matrix multiplication.

However, Yee and Shinn[33] found a simplified method of computing α, which eliminates the need to explicitly form the inverse R matrix.

$$\alpha_{j+\frac{1}{2},k} = \overline{\overline{R}}^{-1}_{j+\frac{1}{2},k} \begin{bmatrix} \Delta\rho^1_{j+\frac{1}{2},k} - c^1 A_1 \\ \Delta\rho^2_{j+\frac{1}{2},k} - c^2 A_1 \\ \cdots \\ \Delta\rho^N_{j+\frac{1}{2},k} - c^N A_1 \\ -U_t A_2 + k_2 \Delta m - k_1 \Delta n \\ \frac{1}{2}\left[A_1 - \frac{1}{a}(U_k A_2 - A_3) \right] \\ \frac{1}{2}\left[A_1 + \frac{1}{a}(U_k A_2 - A_3) \right] \end{bmatrix} \tag{A.23}$$

where

$$A_1 = \frac{1}{a^2}\left[\sum_{l=1}^{N} \frac{\partial p}{\partial \rho_l} \Delta\rho^l - \frac{\partial p}{\partial e}(u\Delta m + v\Delta n + w\Delta q - \Delta e) \right] \tag{A.24}$$

$$A_2 = \sum_{l=1}^{N} \Delta\rho^l \tag{A.25}$$

$$A_3 = k_1 \Delta m + k_2 \Delta n + k_3 \Delta q \tag{A.26}$$

and

$$k_1 = \frac{\xi_x}{k_\xi} \qquad k_2 = \frac{\xi_y}{k_\xi} \tag{A.27}$$

$$U_k = k_1 u + k_2 v \tag{A.28}$$

$$U_t = k_2 u - k_1 v. \tag{A.29}$$

A.4 Finding the components of Φ

The components of Φ, denoted by ϕ^l, can now be calculated. For the j+1/2 points,

$$\phi^l_{j+\frac{1}{2},k} = \frac{1}{2}\psi(\lambda^l_{j+\frac{1}{2},k})(g^l_j - g^l_{j+1}) - \psi(\lambda^l_{j+\frac{1}{2},k} + \gamma^l_{j+\frac{1}{2}})\alpha^l_{j+\frac{1}{2},k} \tag{A.30}$$

The function ψ(Z) is actually the same as that of Eq. 5.25. That is, if $|Z| > \varepsilon$, then

$$\psi(Z) = |Z| \tag{A.31}$$

otherwise

$$\psi(Z) = \frac{(Z^2 + \varepsilon^2)}{(2\varepsilon)} \tag{A.32}$$

where ε is some small number.

Several different forms for the limiter function g^l_j are available. Here, the limiter is defined by

$$g^l_j = \text{minmod}\left[\alpha_{j-\frac{1}{2},k}, \alpha_{j+\frac{1}{2},k}\right] \tag{A.33}$$

where the minmod function yields the argument whose absolute value is the smallest in magnitude. An equivalent expression is

$$g^l_j = S \cdot \max\left[0, \min\left(\left|\alpha_{j+\frac{1}{2},k}\right|, S \cdot \alpha_{j-\frac{1}{2},k}\right)\right] \tag{8.1}$$

where

$$S = \text{sign}\left(\alpha_{j+\frac{1}{2},k}\right) \tag{8.2}$$

Once the g_j^l are known, then

$$\begin{aligned} \gamma^l_{j+\frac{1}{2}} &= \frac{1}{2}\psi(\lambda^l_{j+\frac{1}{2},k}) \cdot \frac{g^l_{j+1} - g^l_j}{\alpha^l_{j+\frac{1}{2},k}} && \text{if } \alpha^l_{j+\frac{1}{2},k} \neq 0 \\ \gamma^l_{j+\frac{1}{2}} &= 0 && \text{if } \alpha^l_{j+\frac{1}{2},k} = 0 \end{aligned} \tag{8.3}$$

A.5 Assembly into the $R\Phi$ matrix

Once the components of Φ are known, then the vector $R\Phi$ can be assembled.

$$R\Phi_{j+\frac{1}{2},k} = \begin{bmatrix} \phi^1_{j+\frac{1}{2},k} + c^1 K_1 \\ \phi^2_{j+\frac{1}{2},k} + c^2 K_1 \\ \cdots \\ \phi^N_{j+\frac{1}{2},k} + c^N K_1 \\ uK_2 + k_1 K_3 + k_2 \phi^{N+1} \\ vK_2 + k_2 K_3 - k_1 \phi^{N+1} \\ H_0 K_2 - \sum_{l=1}^{N} \frac{(a^l)^2}{(\frac{\partial p}{\partial e})} \phi^l + U_k K_3 + U_t \phi^{N+1} \end{bmatrix} \tag{A.34}$$

where

$$K_1 = \phi^{N+2} + \phi^{N+3}$$

$$K_2 = \sum_{l=1}^{N+3} \phi^l - \phi^{N+1}$$

$$K_3 = a\,(\phi^{N+2} - \phi^{N+3}) \qquad \text{(A.35)}$$

Appendix B. Flux Jacobians

Implicit numerical solutions of the Navier-Stokes equations require knowledge of the derivatives of the fluxes with respect to the conserved variables. The matrices of derivatives are known as the flux Jacobians, and can be found for both the inviscid and viscous fluxes. The inviscid flux Jacobians, $A \equiv \frac{\partial F}{\partial Q}$ and $B \equiv \frac{\partial G}{\partial Q}$, are calculated as follows:

$$A, B = \begin{bmatrix} k_0 + U\left(1 - \frac{\rho_1}{\rho}\right) & \cdots & -U\frac{\rho_1}{\rho} \\ \cdots & \cdots & \cdots \\ -U\frac{\rho_N}{\rho} & \cdots & k_0 + U\left(1 - \frac{\rho_N}{\rho}\right) \\ -uU + k_1 p_{\rho_1} & \cdots & -uU + k_1 p_{\rho_N} \\ -vU + k_2 p_{\rho_1} & \cdots & -vU + k_2 p_{\rho_N} \\ U(p_{\rho_1} - H) & \cdots & U(p_{\rho_N} - H) \end{bmatrix}$$

$$\begin{bmatrix} k_1\frac{\rho_1}{\rho} & k_2\frac{\rho_1}{\rho} & 0 \\ \cdots & \cdots & \cdots \\ k_1\frac{\rho_N}{\rho} & k_2\frac{\rho_N}{\rho} & 0 \\ k_0 + U + k_1 u(1 - p_e) & k_1 u - k_2 v p_e & k_1 p_e \\ k_1 v - k_2 u p_e & k_0 + U + k_2 v(1 - p_e) & k_2 p_e \\ -uUp_e + k_1 H & -vUp_e + k_2 H & k_0 + U(1 + p_e) \end{bmatrix} \qquad \text{(B.1)}$$

where $k_0=\xi_t$, $k_1=\xi_x$, $k_2=\xi_y$ for A and $k_0=\eta_t$, $k_1=\eta_x$, $k_2=\eta_y$ for B, and $U=k_1u+k_2v$.

Using the same procedure as Steger,[34] the Jacobians of the axisymmetric source terms, $C \equiv \frac{\partial H}{\partial Q}$, is found:

$$C = \begin{bmatrix} v\left(1-\frac{\rho_1}{\rho}\right) & -v\frac{\rho_1}{\rho} & \cdots & -v\frac{\rho_1}{\rho} & 0 & \frac{\rho_1}{\rho} & 0 \\ -v\frac{\rho_2}{\rho} & v\left(1-\frac{\rho_2}{\rho}\right) & \cdots & -v\frac{\rho_2}{\rho} & 0 & \frac{\rho_2}{\rho} & 0 \\ \cdots & \cdots & & \cdots & & \cdots & \cdots \\ -v\frac{\rho_N}{\rho} & -v\frac{\rho_2}{\rho} & \cdots & v\left(1-\frac{\rho_N}{\rho}\right) & 0 & \frac{\rho_N}{\rho} & 0 \\ -uv & -uv & \cdots & -uv & v & u & 0 \\ -v^2 & -v^2 & \cdots & -v^2 & 0 & 2v & 0 \\ v(p_{\rho_1}-H) & v(p_{\rho_1}-H) & \cdots & v(p_{\rho_N}-H) & -uvp_e & H-v^2p_e & v(1+p_e) \end{bmatrix} \quad \text{(B.2)}$$

Similarly, the viscous flux Jacobians can be found by differentiating the viscous fluxes F_V, G_V, and H_V with respect to the matrix of conserved quantities Q. However, since the viscous terms tend to be nonlinear, the calculation become quite lengthy. In order to simplify the calculation, a common assumption is that gradients in the streamwise direction are much lesser in magnitude than in the normal direction; thus, in calculating the viscous flux Jacobians, terms with derivatives in the streamwise direction are neglected. This assumption is only valid for thin boundary layers; hence, the resulting set of equations is called the thin-layer Navier-Stokes equations. Note that the calculation of only the viscous flux Jacobian needs to be simplified; the rest of the unsteady Navier-Stokes equations, including the viscous fluxes, can still include terms involving streamwise derivatives.

Thus, the remaining viscous flux Jacobian matrix is:

$$B_V = \begin{bmatrix} 0 & \cdots & 0 & 0 & 0 & 0 \\ \cdots & & \cdots & \cdots & \cdots & \cdots \\ 0 & \cdots & 0 & 0 & 0 & 0 \\ M_{N+1,1} & \cdots & M_{N+3,1} & \alpha_1 \frac{\partial}{\partial \eta}(\frac{1}{\rho}) & \alpha_2 \frac{\partial}{\partial \eta}(\frac{1}{\rho}) & 0 \\ M_{N+2,1} & \cdots & M_{N+3,1} & \alpha_2 \frac{\partial}{\partial \eta}(\frac{1}{\rho}) & \alpha_3 \frac{\partial}{\partial \eta}(\frac{1}{\rho}) & 0 \\ M_{N+3,1} & \cdots & M_{N+3,N} & M_{N+3,N+1} & M_{N+3,N+2} & M_{N+3,N+3} \end{bmatrix} \quad \text{(B.3)}$$

where

$$M_{N+1,1} = -\alpha_1 \frac{\partial}{\partial \eta}(\frac{u}{\rho}) - \alpha_2 \frac{\partial}{\partial \eta}(\frac{v}{\rho}) \quad \text{(B.4)}$$

$$M_{N+2,1} = -\alpha_2 \frac{\partial}{\partial \eta}(\frac{u}{\rho}) - \alpha_3 \frac{\partial}{\partial \eta}(\frac{u}{\rho}) \quad \text{(B.5)}$$

$$M_{N+3,1} = \alpha_4 \frac{\partial}{\partial \eta}\left(-\frac{e}{\rho^2} + \frac{u^2+v^2}{\rho}\right) - \alpha_1 \frac{\partial}{\partial \eta}(\frac{u^2}{\rho}) - 2\alpha_2 \frac{\partial}{\partial \eta}(\frac{uv}{\rho}) - \alpha_3 \frac{\partial}{\partial \eta}(\frac{v^2}{\rho}) \quad \text{(B.6)}$$

$$M_{N+3,N+1} = -\alpha_4 \frac{\partial}{\partial \eta}(\frac{u}{\rho}) - M_{N+1,1} \quad \text{(B.7)}$$

$$M_{N+3,N+2} = -\alpha_4 \frac{\partial}{\partial \eta}(\frac{v}{\rho}) - M_{N+2,1} \quad \text{(B.8)}$$

$$M_{N+3,N+3} = \alpha_4 \frac{\partial}{\partial \eta}(\frac{1}{\rho}) \quad \text{(B.9)}$$

$$\alpha_1 = \mu(\frac{4}{3}\eta_x^2 + \eta_y^2) \quad \text{(B.10)}$$

$$\alpha_2 = \frac{\mu}{3}\eta_x \eta_y \quad \text{(B.11)}$$

$$\alpha_3 = \mu\left(\eta_x^2 + \frac{4}{3}\eta_y^2\right) \tag{B.12}$$

$$\alpha_4 = \frac{k}{C_v}\left(\eta_x^2 + \eta_y^2\right) \tag{B.13}$$

In this form, B_V would be added to B in the Navier-Stokes equations; the analogous flux Jacobians A_V and C_V are neglected.

Appendix C. Turbulence Modeling

C.1 Baldwin-Lomax Model

The Baldwin-Lomax model of turbulence[40] is an often-used model of turbulence, mainly because of its simplicity. It is an eddy-viscosity model, meaning that the effective viscosity is simply the sum of separate laminar and turbulent terms. Thus,

$$\mu = \mu_L + \mu_T \tag{C.1}$$

where μ_L is the laminar viscosity, an intrinsic property of the fluid, and μ_T is the increase in observed viscosity due to turbulence. The calculation of μ_L is described elsewhere; the computation of μ_T is discussed here.

The turbulent viscosity is defined differently in two layers of the flow:

$$\mu_T = \begin{cases} \mu_{T_{\text{inner}}} & y \le y_{\text{crossover}} \\ \mu_{T_{\text{outer}}} & y > y_{\text{crossover}} \end{cases} \tag{C.2}$$

where $y_{\text{crossover}}$ is the height at which $\mu_{T_{\text{outer}}}$ equals $\mu_{T_{\text{inner}}}$. For the lower layer,

$$\mu_{T_{\text{inner}}} = \rho l^2 |\omega| \tag{C.3}$$

where

$$l \equiv ky\left[1 - \exp\left(\frac{-y_0}{A_0}\right)\right] \tag{C.4}$$

with $A_0 = 26.0$.

$$y_0 \equiv y\frac{\sqrt{\rho_W \tau_W}}{\mu_W} \tag{C.5}$$

with the subscript W indicating conditions at the surface of the solid, and ω is the vorticity, computed from

$$\begin{aligned}\omega &= \frac{\partial u}{\partial y} + \frac{\partial v}{\partial x} \\ &= (\xi_y u_\xi + \eta_y u_\eta) + (\xi_x v_\xi + \eta_x v_\eta)\end{aligned} \tag{C.6}$$

In the upper layer,

$$\mu_{T_{\text{outer}}} = \rho K C_{\text{cp}} F_{\text{wake}} F_{\text{Kleb}} \tag{C.7}$$

where K=0.0168, C_{cp}=1.6, the Klebanoff intermittency factor F_{Kleb} is given by

$$F_{\text{Kleb}} = \left[1 + 5.5\left(C_{\text{Kleb}}\frac{y}{y_{max}}\right)^6\right]^{-1}, \tag{C.8}$$

and

$$F_{\text{wake}} = \min\left(y_{\max} F_{\max}, C_{\text{wk}} y_{\max}\frac{U_{\text{dif}}^2}{F_{\max}}\right). \tag{C.9}$$

In the above equations, the function F is defined by

$$F(y) = y|\omega|\left[1 - \exp\left(\frac{-y_0}{A_0}\right)\right] \tag{C.10}$$

and the values for $y_{\max}$ and $F_{\max}$ correspond to the point where the function $F(y)$ given by Eq. C.10 is at a maximum. In Eq. C.9, $C_{\text{wk}} = 0.25$, and

$$U_{dif}^2 = u^2 + v^2, \tag{C.11}$$

Using the definition of a turbulent Prandtl number

$$Pr_T \equiv \frac{\mu_T c_p}{k_T} \tag{C.12}$$

then the turbulent eddy conductivity can be found, assuming $Pr_T = 1$.

C.2 Prediction of transition

The prediction of the onset of transition in compressible flow is a topic of current study. As such, a definitive method does not yet exist. In spite of the uncertainty, the correlation used here is a simple one, given by Anderson,[51] and relates the Reynolds number at the transition position Re_T to the Mach number M_e at the edge of the boundary layer:

$$\log_{10}(Re_T) = 6.421 \exp(1.209 x 10^{-4} M_e^{2.641}) \tag{C.13}$$

where

$$Re = \frac{\rho_e U_e x}{\mu_e}. \tag{C.14}$$

The subscript e refers to conditions at the edge of the boundary layer. The variables ρ, U, μ, and x are the density, velocity, viscosity, and streamwise coordinate, respectively.

Thus, starting from the leading edge, the Reynolds and Mach numbers at each point along the surface must be calculated. At the leading edge, $x = 0$, so $Re = 0$, and the left

side of Eq. C.13 is then clearly less then the right side. Transition is predicted to occur at the first point where the inequality is reversed; that is, when

$$\log_{10}(Re) \geq 6.421 \exp(1.209x10^{-4}M_c^{2.641}). \qquad \text{(C.15)}$$